PhD in Astronomy, Astrophysics and Space Science
Cycle XXXII

Validation of the IPSL Venus General Circulation Model with Venus Express data

Pietro Scarica
A.Y. 2019/2020

Supervisor:
Giuseppe Piccioni

Co-supervisor:
Francesco Berrilli
Chiara Cagnazzo

Table of contents

Introduction

Several numerical models devoted to the simulation of Venus atmosphere have been developed. These models are useful instruments in the understanding of the mechanisms behind the observational features. However, before using their outputs to drive any conclusion about the dynamics and the structure of the atmosphere of Venus, we need to validate them. The process of validation passes by a comparison of the modelled and observational features.

Among these numerical models, the Institut Pierre Simon Laplace (IPSL) Venus GCM is the one with a more physical approach, being capable to solve the radiative transfer for each layer of the simulated atmosphere. Our study makes use of Venus Express data – in particular VIRTIS (Visible and Infrared Thermal Imaging Spectrometer) and VeRa (Venus Express Radio Science Experiment) observations – in order to validate this model.

This work will analyze the temperature and wind fields in the atmosphere of Venus between 50 and 90 km, that is the range covered by observations. In this range – covering from the upper troposphere to the upper mesosphere – two different regimes are found in the observational thermal field, above and below ~ 76 km, with temperatures increasing towards the pole and towards the equator, respectively. At cloud top level (~ 68 km), permanent cold features, the cold collars, encircle the warmer poles. Winds velocities reach their maximum values (~ 120 m/s) at cloud top, but are faster than the solid body through the entire range of altitudes, determining a condition called superrotation. Seasonal thermal tides are negligible in data, but those related to the diurnal cycle, are present and have a large impact, especially in the upper atmosphere.

Venus modelling has always suffered from the strong dependence of the simulation by the initial conditions and the different dynamical cores. Winds far weaker than observed, as well as the inability to reproduce the complex polar vortexes and the subpolar cold regions, have been the major issues for all the numerical simulations for Venus.

However, to simulate the fast rotation of the atmosphere and to properly model the thermal structure associated to the polar and subpolar regions, means to understand the physical conditions under which these characteristics develop. Thus, the first objective of our validation of the IPSL Venus GCM is to estimate the general characteristics of the modelled atmosphere and their resemblance of observations. A first, qualitative comparison, is fundamental in recognizing the main dynamical regions in Venus atmosphere.

Being the main goal of this work, the validation of a model through its comparison with the thermal and winds field in observational data, we need to clarify the adopted ingredients and the state of the art of our knowledge of Venus. Thus, in **chapter 1** we present the overall characteristics of

Venus atmosphere, in terms of its composition, thermal structure and dynamics. In **chapter 2** we discuss the Venus Express mission, with a focus on the VIRTIS and VeRa experiments and the datasets that we used in this analysis. In **chapter 3** we describe the evolution and the present state of the major numerical models trying to simulate the atmosphere of Venus, with a particular emphasis on the IPSL Venus GCM. **Chapter 4** and **chapter 5** present our validation: the former concerns the analysis of the average temperature and wind fields, the latter is about the thermal tides affecting the temperature and wind fields. As a result, we recognize the capability of the model to reproduce the main observational feature and we propose future steps in order to overcome the major discrepancies that we found in our validation.

1. The atmosphere of Venus

Being one of the most prominent and bright objects in the sky, Venus, the second planet of the Solar System, has always been a reference mark at dusk and dawn. For a long time, we called it "the morning star" or “the evening star”, to underline its nature.

Several astronomical observations have been accounted among many different ancient peoples, leading to the drawing of Venus motion in the sky. In a more recent era, along the years of early telescopic observations, Venus phases played a crucial role in the validation of the Copernicus heliocentric theory by Galileo Galilei and, therefore, in supporting the first steps of modern astronomy. Since then, it drove more and more the curiosity of the astronomers: Venus have a size and a mass very similar to Earth. For such reason, it is not surprising that it was depicted for a long time as the “twin sister” of our planet.

As long as we entered in the modern era, we knew that this was not true: there are no layers of water vapor and the sentence "everything on Venus is dripping wet" (Arrhenius, 1918), does not correspond to reality. Indeed, Venus has been extensively investigated thanks to ground-based observations (Boyer and Guerin, 1969; Allen and Crawford, 1984), that allows a broad range of spectral coverage and monitoring over long period. Moreover, since the beginning of the space age, it also became the target of several space missions devoted to the exploration of the planet. The first successful flyby of Venus was performed by the NASA Mariner 2 (Sonett, 1963), whose radiometer measured a surface temperature of 460°C and revealed an atmosphere mainly composed by carbon dioxide. The Venera program (Avduevsky et al., 1983), the VEGA program (Blamont et al., 1987), the Magellan mission (Saunders et al., 1992) and the Pioneer Venus (Colin and Hunten, 1977) contribute to determine the atmospheric properties and the surface physical conditions through the use of orbiters, probes and landers. More recently, the Galileo (Carlson et al., 1991) and Cassini (Russell, 2003) spacecrafts observed the planet during close encounters made on their way towards their target in the outer Solar System.

Venus finally revealed its true nature, well hidden under the dense atmosphere, along with all the critical points that make it so different from Earth: despite having a mass of $4.8675*10^{24}$ Kg (Konopliv et al., 1999) and an equatorial radius of 6051.3 (Schubert et al., 1983), both very much similar to that of our own planet, Venus presents a strong greenhouse effect, that is responsible for a climate far hotter and dryer than that of Earth. Moreover, Venus has a huge atmospheric mass (92 times larger than that of our planet) and a mainly-carbon dioxide atmospheric composition, it shows discrepancies in the noble gases abundances with respect to Earth (Pepin, 2006) and it has no internal magnetic field (Luhmann and Russell, 1997).

The search for a “twin sister” ended and the space exploration moved to other targets. Venus has then remained unexplored for more than a decade, until 2005, when the European Space Agency (ESA) launched the Venus Express mission (VEX).

Venus Express, with its short developments time and the design heritage adopted by Mars Express, has provided a huge amount of data, that have increased the knowledge of the planet and furnished a nice comparison for all the numerical models that want to simulate the observed atmospheric features. The Venus Express mission (Titov et al., 2008) was very successful. Venus has come back into the spotlight of planetary science and the interest towards its exploration has grown. In 2010, the Japan Aerospace Exploration Agency (JAXA) launched Akatsuki, that observed bow shapes in the atmosphere of the planet (Fukuhara et al., 2017), never seen before, demonstrating that the investigation of Venus has not yet come to an end.

Now that the exploration of the Solar System is living a season of renewed interest among the scientific community, for both the study of minor and major bodies, in the inner and outer regions, Venus comes into the forefront and it has also been pointed as a possible target for future space missions (Glaze et al., 2018).

The atmosphere and the evolution of the climate of Venus are topics of great interest in Planetary Science. Indeed, an improved understanding of Venus is essential to better appreciate the terrestrial planet origin and evolution and to interpret observations of new earth-sized planets being discovered in other solar systems. The great amount of data acquired and those that will be collected in the next future, will become even more important thinking to a direct comparison with Earth in particular. This is indeed a focal point: whether due to a discrepancy within the original atmospheric ingredients or to the evolutionary paths of the two planets (Taylor and Grinspoon, 2009), Venus and Earth reached very different states.

How a body so similar to our planet has evolved in a so different way? The understanding of Venus atmosphere and its different story, starts from the study of its present conditions. Here we describe the state of the art of our knowledge of the atmosphere of Venus, analyzing in detail its composition (**section 1.1**), structure (**section 1.2**) and dynamics (**section 1.3**).

1.1 Composition

The massive atmosphere of Venus is mainly CO_2 (96.5%). Since Adams and Dunham (1932) we know the presence of absorption bands of CO_2 in the atmosphere of our neighbor planet. Our recent knowledge (Vandaele et al., 2008) confirms that carbon dioxide is the main absorber in the infrared region, with absorption bands that span throughout wide regions of the spectrum, and we are also capable to distinguish between different CO_2 isotopologues. Carbon dioxide is far more abundant than on Earth (0.04%) and it is the main responsible of the strong greenhouse effect that is observed on Venus (**Fig. 1**).

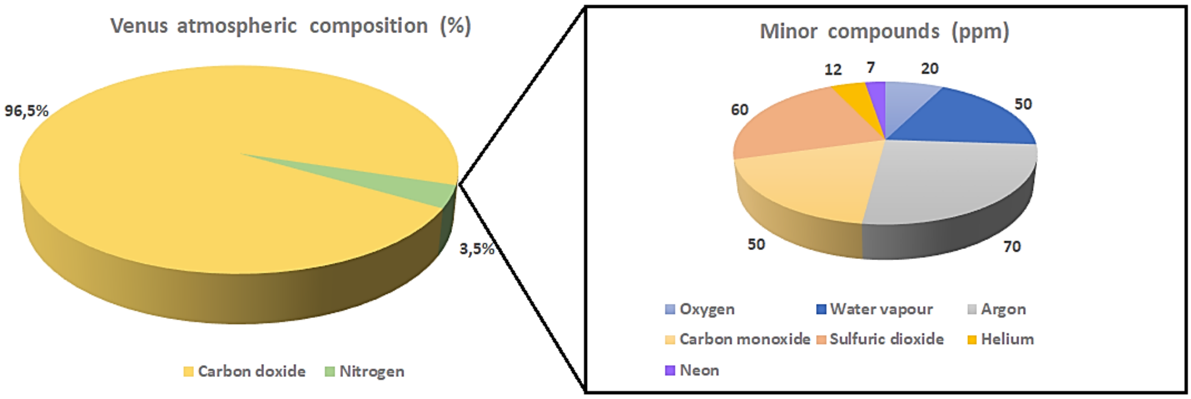

Figure 1: *Carbon dioxide is the main compound in Venus atmosphere (left panel; abundances expressed in part-per-hundred). Minor compounds abundances are expressed in part-per-million (right panel).*

Apart from CO_2, Venus atmosphere primarily consists of inert gases, like nitrogen – that is a 3.5% of the total – argon and neon. Sulfur-bearing gases (like OCS and SO_2), halides compounds (HCL and HF), carbon compounds (like CO) and water vapor, are also present in a few hundred parts per million (ppm) (de Bergh et al., 2006).

CO and other minor compounds are important trackers for the dynamics of the Venusian atmosphere and a mirror of the interaction happening between the surface and the atmosphere, and between the atmosphere and the outer space. The discovery of the spectral windows in the near infrared (Allen and Crawford, 1984), through which thermal radiation escapes into space from the lower atmosphere, allowed the study of atmosphere composition below the clouds on the nightside of the planet. For instance, the carbon monoxide, very abundant in the upper atmosphere (above the clouds), due to the photo-dissociation of CO_2, becomes less abundant in the lower layers, where it acts as a reducing agent. In particular, carbon monoxide is even more depleted towards the equator, giving a hint of a subsidence region in the polar dynamics of the planet. On the other hand, OCS – one of the products of CO chemical reaction at low levels – shows an opposite tendency: it is more depleted in the high atmosphere and latitudes close to the pole (Marcq et al., 2008).

More than this, some of the minor compounds have a great influence on the overall energy balance, even if present in small percentages. In particular this is the case of the sulfuric acid (H_2SO_4), that is the main compound (75%) of the cloud deck (48 – 70 km) and is produced by chemical reactions between CO_2, SO_2, H_2O and chlorine compounds. A lower (30 – 48 km) and a higher haze (70 – 90 km) have also been found on the bottom and on the top of the cloud deck: data from the Pioneer Venus were interpreted as indicating four populations of particles (Knollenberg and Hunten, 1980). Mode 1 particles have a typical radius of 0.1 – 0.2 μm and make up the bulk of the upper cloud layers (Wilson et al., 2008). The larger mode 2 particles (mean radius 1.0 μm) make up the particulate mass in the upper clouds, while the slightly larger mode 2' particles (mean radius 1.4 μm) are found in the middle and lower clouds. The large mode 3 particles (typical radius 3.5 – 4.0 μm) are mainly found in the base of the clouds (Titov et al., 2018).

Variations in the amount of SO_2 have been observed above the clouds of Venus (Belyaev et al., 2008); one of the possible explanations, other than changes in the effective eddy diffusion in the cloud layer (Krasnopolsky, 1986) and in the atmospheric dynamics (Clancy and Muhleman, 1991), involves active volcanism (Shalygin et al., 2015). On the other hand, the thick layer of clouds would dissipate without a sustained outgassing of sulfur dioxide into the atmosphere, responsible of replenishing the mechanisms of clouds formation (Taylor and Grinspoon, 2009). Thus, interactions atmosphere-surface can not be underestimate in general: surface minerals can interact through outgassing with the lower atmosphere, boosting the abundance of gases.

Water is roughly one hundred thousand times less than in Earth's oceans and atmosphere. Venus is very dry, but its D/H ratio is about 127 times the terrestrial one (Bézard et al., 2011). Given the observed horizontal uniformity of H_2O abundances and the lack of sources (Bézard et al., 2009), this ratio reveals two possibilities: either this is a trace of the last 10^9 years of escape and resupply (Grinspoon, 1993), or there was a large primordial water ocean (Donahue et al., 1997), loss by photo-dissociation of water in the upper atmosphere by solar ultraviolet radiation, followed by the leakage of hydrogen into the outer space. Models of a Venusian large primordial water ocean are based on an early volatile delivery and does not consider stochastic processes happening in different early-planets; Kasting (1988) derived a timescale for the loss of water of hundred million years, while Grinspoon and Bullock (2007), in the presence of a simplified cloud feedback, suggests a timescale of 2-3 billion year. Whether hundred million years or a few billion years, as long as liquid water was available, carbonates removed atmospheric carbon dioxide. After the disappearing of water basins, the removal mechanism vanished, carbonate rocks have been probably lost due to thermal decomposition and the CO_2 have been consequently accumulated into the atmosphere through outgassing, leading to the present runaway greenhouse effect that is observed (Taylor and Grinspoon, 2009).

Thus, observations and models suggest that Venus and Earth had a very similar past and evolved differently (Svedhem et al., 2007). These discrepancies become even more clear when it comes to the comparison of the thermal structure and the dynamics of the two planets.

1.2 Thermal Structure

With a solar constant of 2621 W m^{-2} (Sanchez-Lavega 2011), Venus receives almost twice the solar flux of Earth. About 75% of the incoming radiation is reflected into the outer space by the H_2SO_4 clouds. Half of the sunlight received by Venus is then absorbed by CO_2 at altitudes around 65 km and by an unknown UV-absorber between 35 and 70 km. The other half is absorbed through the inner atmosphere layers, before reaching the surface; only a 2.6% of the incident radiation reaches the surface of the planet (Sanchez-Lavega 2011).

The atmospheric structure of Venus is defined through its physical quantities (i.e. pressure, density, temperature) and may vary vertically, horizontally and temporally. Basing on the main processes that govern Venus' atmosphere and on the most peculiar thermal feature that are observed, we can recognize three different layers:

(i) The troposphere (0-60 Km);

(ii) The mesosphere (60-100 Km);

(iii) The thermosphere (100-200 Km).

(i) The troposphere (**Fig. 2**), the lowest layer of Venus atmosphere, displays a temperature which decreases monotonically from 735 K on the surface to the upper limit of 245 K (± 35K) (Tellmann et al., 2009). On the surface, pressure reaches the very high value of 92 bars. The troposphere is so dense to contain about 99% of the total atmospheric mass: in this such extreme physical conditions, both carbon dioxide and nitrogen should be in supercritical state (Lebonnois and Schubert, 2017). The lapse rate is -10 K/km, which identifies a stable atmosphere, apart from regions near the base of the cloud layer (~ 45 km) and below 20 km. Diurnal changes in the deep atmosphere are expected to be very low (< 1 K) due to the large thermal inertia. From 45 km, until the top of the troposphere, there are the lower and middle sulfuric acid clouds, which have a strong influence on the thermal structure and stability of the Venusian atmosphere: changes in the temperature lapse rate with altitude are found and coincide with the boundaries of the cloud layers. Around 60 - 62 km is located a large temperature inversion called tropopause, defined (Kliore, 1985) as the level where the temperature lapse exceeds -8 K/km, and which also represents the upper boundary of both middle clouds and troposphere.

(ii) The mesosphere is the second layer of the atmosphere. Its temperatures display a variability – especially related to latitudinal changes – much more evident than in the troposphere.

Within the upper clouds (60-70 Km) the temperature lapse rate is almost zero (**Fig. 2**), while it decreases again over the clouds top level, even if with a lapse rate lower than in the troposphere and nearly isothermal close to the poles. At an altitude higher than 75 km, the vertical temperature gradient is negative at all latitude. The lapse rate is -7.6 K/km below 80 km, and then drops to -3.5 K/km, above 80 km (Patzold et al., 2007).

Poleward of 80°, warm pole is observed (Piccioni et al., 2007), with values around 250 K at 60 km. Infrared observations have revealed local temperature minima (~ 210 – 220 K) within the upper clouds, at approximately 60-65 km altitude and 65° latitudes on both hemispheres (**Fig. 3**), with temperatures at 3:00 LT (Local Time) colder (about 8-10 K) than at 18:00 LT. These cold regions partially envelop the bright polar vortexes. For their nature of being circumpolar features and colder than the surroundings, they are named cold collars. Each cold collar peaks towards the morning terminator with a temperature 40 – 50 K colder than the warm poles (Piccioni et al. 2007; Garate-Lopez et al. 2015).

Close to the two day-night terminators – in particular the evening terminator – warm regions are detected during nighttime, peaking around 68 km at 240 K (Tellmann et al., 2009).

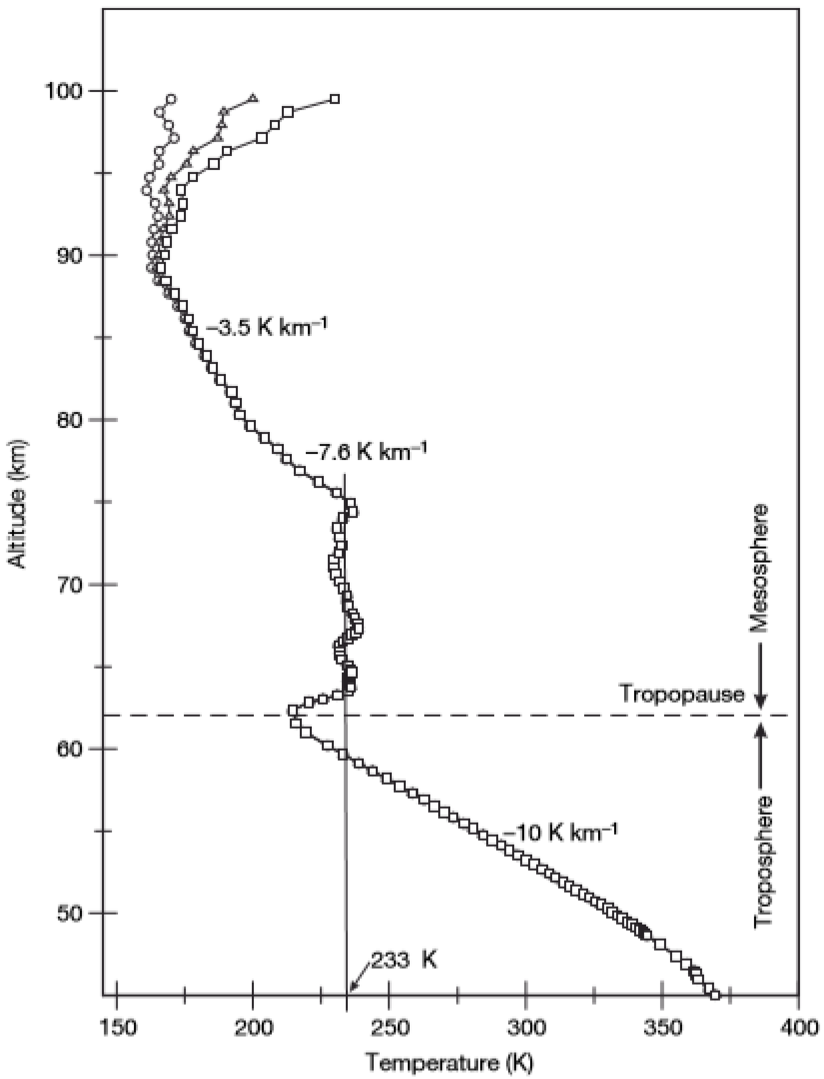

Figure 2: *Temperatures (K) with respect to the altitude (km). Data acquired by VeRa/VEX at 71° latitude. (Patzold et al., 2007)*

Two different regimes are recognizable (**Fig. 3**): below 70 km altitude, the temperature increases from the pole to the equator, above 70 km, the temperature increases poleward. At 80 km, a temperature of 205 K is found at the equator, 215 K at the poles (Limaye et al., 2018). Since the solar heating is higher at equator than poles, this trend indicates a significant role of atmospheric dynamics in the heat transfer above 70 km.

At the top of the mesosphere (70 – 90 km) the atmosphere is stressed by the thermal tides, day-to-night variations of heating caused by the incoming solar radiation (Limaye et al., 2018). Thermal tides are induced in the atmosphere by the solar cycle, and results from the combination of the rotation of Venus on its polar axis and of the revolution around the Sun. The diurnal cycle of the solar heating in the Venus atmosphere induces tides with wavenumbers 1 (diurnal), 2 (semi-diurnal), and higher orders.

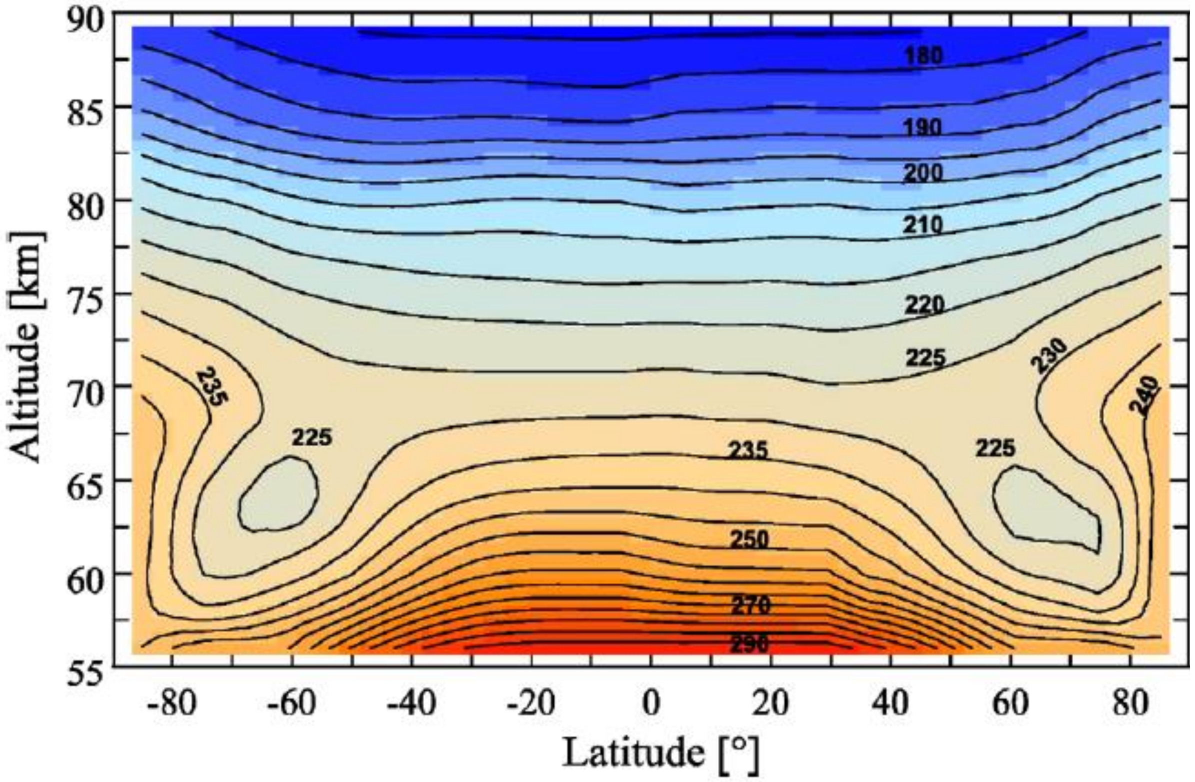

Figure 3: *Temperature structure of the mesosphere during nighttime. Cold collar features are clearly recognizable around 60° - 70° (60 - 65 km altitude), at both hemispheres. Warmer regions are found around the poles. Haus et al., 2014, based on VIRTIS-M data.*

The upper boundary of the mesosphere is the mesopause, which is located roughly between 95 and 120 Km. Temperature increases until ~ 103 km and then decreases until ~ 110 km altitude. Although ozone has been detected on Venus (Montmessin et al. 2011) around 100 km, its abundance is too low to be responsible for this temperature inversion. No stratosphere has been observed on Venus between the troposphere and the mesosphere: the lack of a stable ozone layer, implies that this reversal of the temperature may be due to aerosols rather than ozone.

(iii) The thermosphere is the uppermost layer and it is more sensible to diurnal effects: while the dayside temperature is affected by the incoming solar radiation, the nightside is not provided with that heat and it is then – commonly – known as cryosphere: nighttime and daytime are separated by a sharp transition. On Venus the nighttime temperature in the thermosphere is very low, around 100 K, in contrast to 300 K on the dayside. These global oscillations of the atmosphere are forced by the thermal tides.

The average vertical temperature gradient in Venus' dayside thermosphere is around 1.1-1.8 K/km (Muller-Wodarg et al., 2006), while it is negative during nighttime, reaching values of -1.2 K/km. Due to the lack of an internal magnetic field, the thermosphere is also the one interacting directly with the solar wind: this interaction produces the observed loss of oxygen ions (Luhmann et al., 2008) and neutrals compounds (Galli et al., 2008) and represents one of the mechanisms that produced the composition that we measure today. Besides the interaction with the solar wind, several other processes happen within the thermosphere: dissociation, ionization, thermal/nonthermal escape, cosmic ray erosion, meteoritic and cometary impacts.

1.3 Dynamics

To observe the atmospheric circulation, different methods have been adopted: these include Doppler Spectroscopy (Machado et al., 2017), direct observation through entry probes and balloons (Moroz and Zasova, 1997; Linkin et al, 1986), radio occultation techniques (Sànchez-Lavega, 2011), tracking of emission features (Drossart and Montmessin, 2015) and tracking of cloud features (Garate-Lopez et al., 2013).

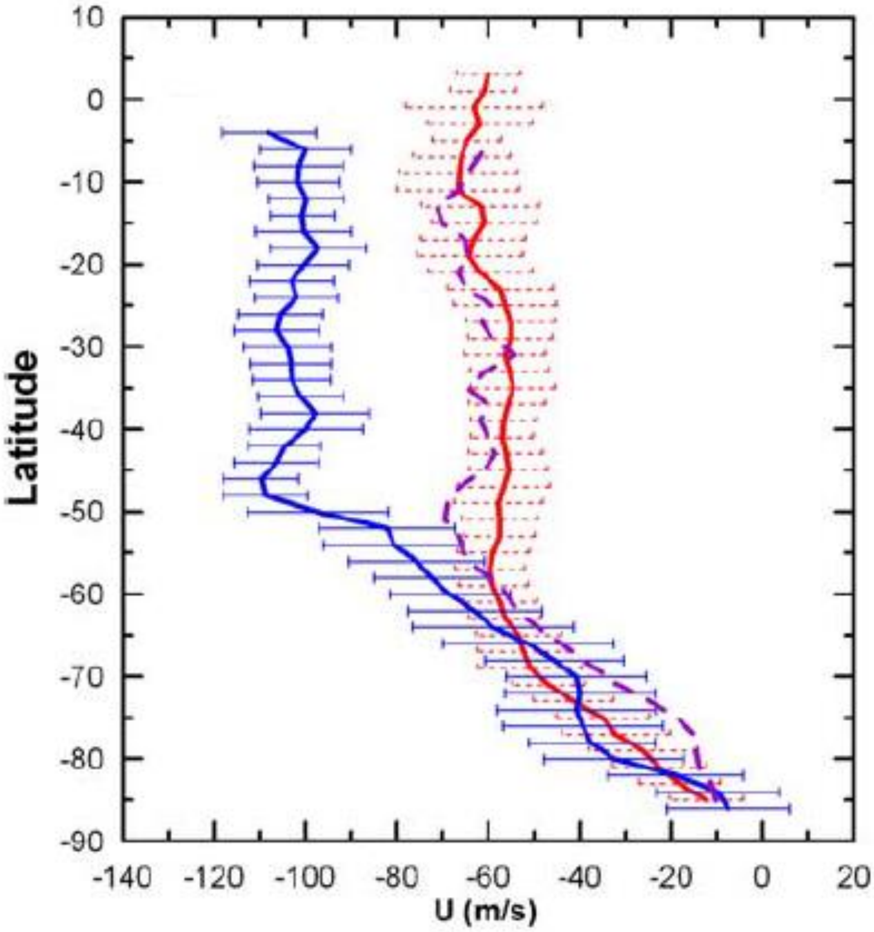

Figure 4: *The averaged zonal wind speeds in the southern hemisphere of Venus as a function of latitude. Retrieved by VIRTIS/VEX data. Blue lines are referred to 62-70 km altitude (top clouds), the purple lines to 58-64 km (base of upper clouds), the red lines to 44-48 km (lower clouds). Adapted from Sanchez-Lavega et al., 2008.*

All probe data agree that the zonal wind speed from surface to 10 km altitude is less than 3 ms^{-1}. From the surface to around 65–70 km, the zonal winds increase globally. Indeed, the mean atmospheric motions are dominated by a rotation that, at the cloud top level, is roughly 60 times faster than that of the planetary body: the upper atmosphere rotates in ~4 days, the solid body in ~243 days. The zonal winds blow westward, in the same direction of the planet rotation, with a nearly constant speed of ~110 ms^{-1} (Garate-Lopez et al., 2013) at cloud top level (roughly 70 km altitude), from latitude 50° N to 50° S, then decrease their speeds monotonically from these latitudes toward the poles (**Fig. 4**). For that reason, Venus' atmosphere is in a Retrograde Superrotation (RSR) state, or simply in "superrotation".

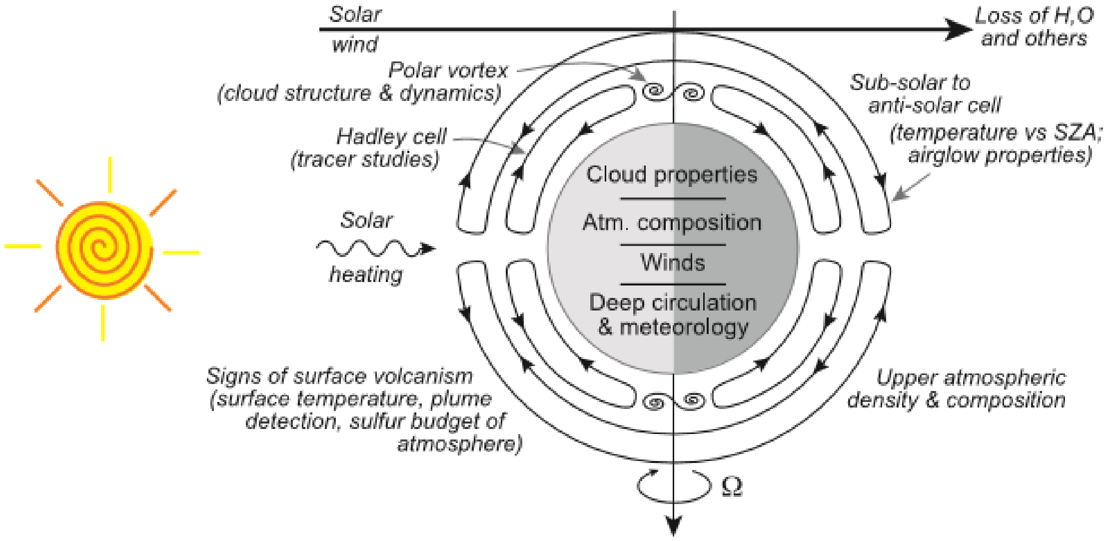

Figure 5: *Schematic representation of the main Venus' circulation features. The main circulation is superimposed to the subsolar to antisolar cell. Adapted by Piccialli, 2010 and Taylor and Grinspoon, 2009.*

The source of this superrotation and the mechanisms that maintain it, are still unknown. However, it is clear that large scale waves, in the form of planetary scale Kelvin waves and small-scale gravity waves (Sornig et al., 2008), play a major role in the efficient pumping of angular momentum through the atmosphere, from the inner layers to the outer ones. Studies (Newman and Leovy, 1992) suggest that the superrotation is maintained by the transport of retrograde zonal momentum upward through thermal tides at the equator and then poleward by the meridional cell. Indeed, in the upper cloud region, a major fraction of the solar energy incident is absorbed by the 'unknown' absorber and sulfuric acid aerosols. This distribution of the absorbed energy generates thermal tides, in the form of planetary-scale waves. The excited waves propagate both upwards and downwards from the forcing region.

In addition to the zonal superrotation, a thermally directed meridional cell flowing from the equator to pole with meridional velocities of less than 10 ms^{-1} has been observed at the cloud top (**Fig. 5**). This meridional circulation is expected to be efficient in transporting warm air poleward and cooler air equatorward. Indeed, CO data obtained for the deep atmosphere by the NIMS onboard the Galileo spacecraft (Collard et al., 1993) and by Venus Express (Tsang et al., 2008), are consistent with a Hadley circulation on Venus that extends from the clouds to the surface, and from the equator to the poles. The less relevance that Coriolis forces have on Venus – with respect to

Earth – allows Hadley cells to extend much closer to the pole.

Above the clouds is present a transition region of complex dynamics that separates the Venus troposphere from the thermosphere: the winds decrease with altitude until a strong subsolar-antisolar (SS-AS) circulation occurs at 90-110 km, because of the large temperature gradient between Venus' daytime and nighttime. By tracking emission features from NO and O_2 airglow, we know that measurements in the 90–110 km altitude of the zonal component range from ~ 5 to 150 ms^{-1}, while wind data for the SS-AS range from 40 up to 290 ms^{-1}, but exhibit very strong day to day variations. This SS-AS component seems to be related to the thermal tides: waves with both a diurnal and a semi-diurnal period have been observed through the data (Rossow et al., 1990; Collard et al., 1993), and a maximum has been detected in the temperature profile near the antisolar point, at around 90 km, corresponding to the adiabatic heating expected in the subsolar to antisolar circulation regime.

The complexity of the Venusian atmospheric dynamics finds its most puzzling element in the polar region (**Fig. 6**), where giant vortexes features are correlated to the subsidence of cold air and the consequent meridional flow due to the recycle of the air towards the equator. Vortexes occur in the polar region of planets: they are characterized by swirling clouds of high vorticity that move around a common center of rotation of low relative vorticity (the "eye"). The Venus' polar vortexes appear like permanent – due to the lack of important seasonal variations – but time varying structures contained in a region ~2500 km wide around the pole. Their position, rotation rate and morphology have been shown to change significantly: the basic core morphology is that of a single (monopole), double (dipole) or triple spiral, with filaments extending outwards from its center or connecting two or more brightness centers (Piccioni et al., 2007). Basing on cloud tracking measurements at 5.0 μm (~65 km), Peralta et al. (2012) detected thermal tides harmonic forcing a solar-to-antisolar circulation across the pole, responsible of the dynamics of these vortex.

South-polar features observed in the atmosphere of Venus are in general similar to those observed around the north pole, with a slightly difference in the rotation period, maybe due to long terms variations in the dynamics, occurring between different observations: the Northern vortex exhibits a rotation period that spans from -2.79 to 3.21 days (Schofield and Diner, 1983; data from Pioneer Venus), while the Southern vortex shows a period of -2.48+- 0.05 days (Piccioni et al., 2007; data from Venus Express). Both rotate with an offset of a few degrees with respect to the geographical pole.

The cold collar features circulate around the vortexes at latitudes between 60° and 80°, where the Hadley cells stop, dividing the middle atmosphere vertically and generating the two different regimes observed in the thermal structure of Venus: below, the atmosphere cools with increasing latitude, while above, it warms with increasing latitude (Kliore et al. 1985).

The dynamics behind the cold collar and the warm pole has only just begun to be investigated (Garate-Lopez et al. 2015). The presence of the cold collar between 55 and 65 km altitude appears to confine the warm vortex to latitudes poleward of 75°S, while at higher altitudes the vortex is more extended. Moreover, while warm poles need short-term processes or some with a certain periodicity (i.e. thermal tides), in order to maintain the pressure differences between the cold collar and the surroundings, some continually forcing mechanism is needed. In order to understand these features, as well as the general structure and dynamics of Venus atmosphere, coupling of observations and numerical models is needed.

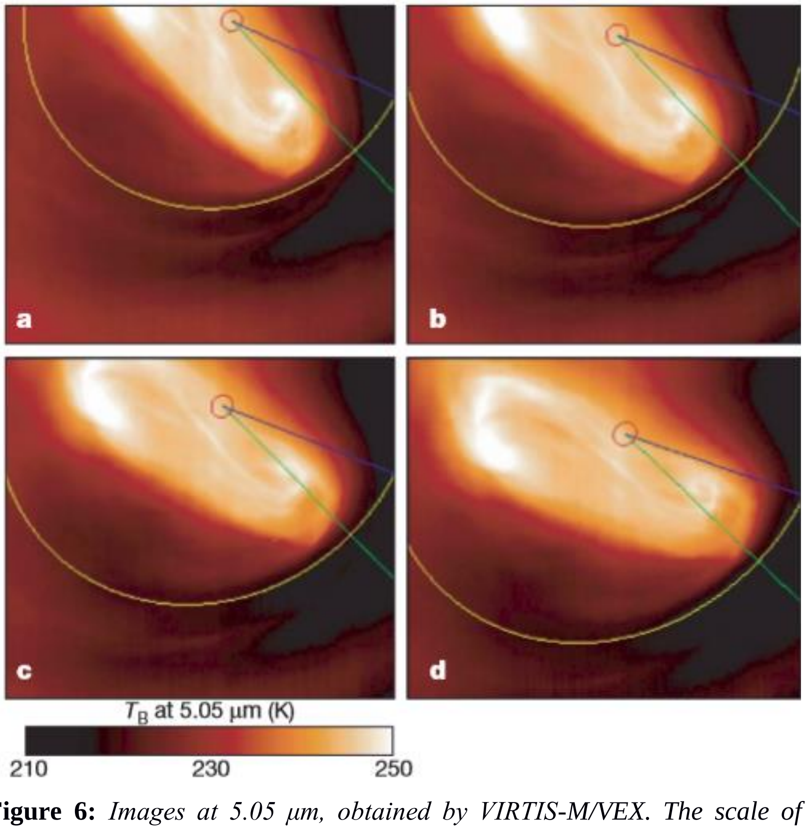

Figure 6: *Images at 5.05 µm, obtained by VIRTIS-M/VEX. The scale of colors indicates the brightness temperature. The polar vortex is rotating around the geographical south pole (red circle) with an offset of 4°. The cold collar is just beyond the yellow line, which indicates the -70° parallel. Piccioni et al., 2007.*

2. The Venus Express mission

Venus Express was the first European mission to reach planet Venus (Titov et al., 2006; Svedhem et al., 2007). After a winning proposal in 2001, aiming to re-use much of the Mars Express basic design for the spacecraft, Venus Express was ready in less than 4 years. Launched by a Russian Soyuz-Fregat launcher on 9 November 2005, from Baikonur (Kazakhstan), it used a slightly modified spacecraft – with respect to Mars Express – in order to adapt to the specific environment around Venus, and a payload carrying the heritage of the Rosetta mission. Venus Express has been a quick-realization, cost-effective mission (**Fig. 7**).

Arrived at Venus on 11 April 2006, it entered a highly elliptic polar orbit of 24 h period, with a pericenter altitude of 250 km over the northern polar region and an apocenter altitude of 66,000 km over the southern polar region (Svedhem et al., 2009). This orbital geometry allowed a much dense coverage of the southern hemisphere with respect to the northern one.

Venus Express aimed at a complete investigation of the atmosphere and plasma environment of Venus and was also able to address some significant features of the surface. The quest of Venus Express can be summarized in seven key topics, according to Svedhem et al. (2007):

1) Atmospheric structure;
2) Atmospheric dynamics
3) Atmospheric composition and chemistry;
4) Cloud layer and hazes;
5) Energy balance and greenhouse effect;
6) Plasma environment and escape processes;
7) Surface properties and geology.

The payload was composed by seven scientific instruments, devoted to answer to the topics above. We provide here a brief overview of the general characteristics **(Table 1**) and objectives of the instruments onboard Venus Express mission. A more detailed description of VIRTIS and VeRa experiments – on which data this work is based – will be given in **section 2.1** and **section 2.2**, respectively.

SPICAV/SOIR (Spectroscopy for the Investigation of the Characteristics of the Atmosphere of Venus/Solar Occultation in the Infrared) (Bertaux et al., 2007) was a set of three UV-IR spectrometers (SPICAVUV, SPICAV-IR, SOIR) to study the thermal profiles and composition of the Venus thermosphere (90-140 km), as well as vertical profiles of the haze above the clouds and the microphysical properties of aerosols within the haze, by means of solar and stellar occultations.

VMC (Venus Monitoring Camera) was a wide-angle camera working in four narrows spectral bands (Markiewicz et al., 2007). The visible band studied water vapor absorption and O_2 airglow emission; the UV band tracked the clouds top in reflected sunlight during daytime, thanks to the unknown UV absorber; the two near-IR bands mapped the global distribution of water vapor and the surface brightness during nighttime.

PFS (Planetary Fourier Spectrometer) was a high spectral resolution IR-spectrometer with two channels (Formisano et al., 2006). Its purposes were to map the temperature field in the 55–100 km altitude range and on the surface, along with a determination of the total radiation budget and the extraction of the abundances profile in the middle and lower atmosphere. However, the mechanism that had to point the field of view of the Spectrometer towards Venus did not move properly after launch.

ASPERA-4 (Analyzer of Space Plasma and Energetic Atoms) included five sensors: two Neutral Particle Detectors (NPD1 and NPD2), a Neutral Particles Imager (NPI), an Electron Spectrometer (ELS) and an Ion Mass Analyser (IMA) (Barabash et al., 2007). ASPERA-4 made measurements in the solar wind and characterized the outer atmospheric regions with respect to flux, energy and composition of the particles (i.e. the determination of the escape rates of H^+, O^+ and He^+).

MAG (Magnetometer) was a dual sensor fluxgate instrument devoted to measure magnitude and direction of the magnetic field around Venus (Zhang et al., 2006). MAG, devoted to the study of the plasma environment of Venus, produced continuous measurements, studying the bow shock and the induced magnetopause.

VIRTIS (Visible and Infrared Thermal Imaging Spectrometer), is described in **section 2.1**.

VeRa (Venus Express Radio Science Experiment), is described in **section 2.2**.

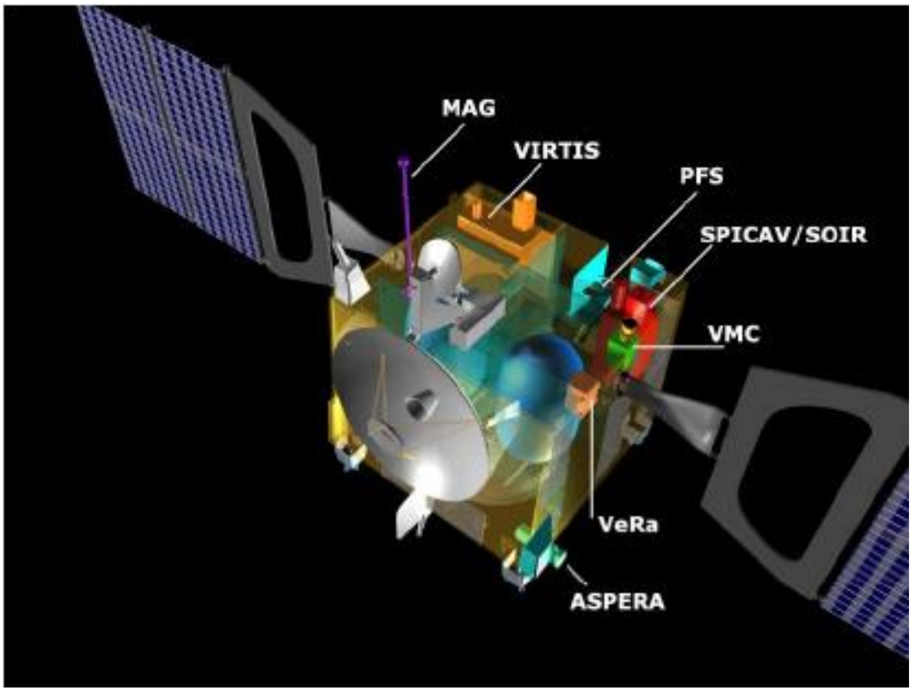

Figure 7: Schematic representation of Venus Express spacecraft. Locations of the instruments are displayed. Copyright by ESA.

2.1 The Visible and Infrared Thermal Imaging Spectrometer

VIRTIS, the Visible and Infrared Thermal Imaging Spectrometer (**Fig. 8**), used a concept and a design very similar to the VIRTIS instrument that flew on the Rosetta spacecraft (Coradini et al., 1998), with some modifications to adapt it to the different environment and target brightness.

VIRTIS was divided in four modules: the Optics Module containing the Optical Heads, the two Proximity Electronics Modules and the Main Electronics Module. Two subsystems were located into the Optics Module: VIRTIS-M, a visible and infrared (0.3 μm up to 5.1 μm) spectro-imager, and VIRTIS-H, an infrared (2 μm up to 5 μm) point spectrometer, which was aligned with the center of the VIRTIS-M field of view (Piccioni et al., 2007; Drossart et al., 2007).

The two optical systems of VIRTIS had parallel slits and were placed at the top of the Optics Module, which was directly coupled to the radiator and the space. The infrared sensors were actively cooled to 80 K, while the visible detector was passively cooled below 200 K.

Table 1	
Name	*General characteristics*
SPICAV/SOIR	Wavelengths: 110–310 nm; 0.7-1.7 µm; 2.2-4.4 µm. Resolving power up to $\lambda/\Delta\lambda$ >20000.
VMC	Wavelengths: 365 nm, 513 nm, 965 nm, and 1000 nm. FOV: 17.5°, pixel size on the surface: 200 m (pericenter) - 45 km (apocenter).
PFS	Wavelengths of the two channels: 0.9–5.5 µm and 5.5–45 µm. Spectral resolution: 1.3 cm^{-1}.
ASPERA-4	Neutral particles energies: 0.1-60keV; Electrons energies: 1eV-15keV; ions energies: 0.01-36keV/q
MAG	Frequency of solar wind samples: 1 Hz. Frequency of pericenter samples: up to 128 Hz.
VIRTIS	VIRTIS-M spectral range: 0.3-5.1 µm; VIRTIS-M spectral sampling: 2 nm (VIS) – 10 nm (IR). VIRTIS-H spectral range: 2-5 µm; VIRTIS-H spectral sampling: 1.5 nm.
VeRa	Wavelength of the "X band": 3.6 cm. Wavelength of the "S band": 13 cm.

VIRTIS-M had a field of view of 64 x 64 mrad, correspondent to a pixel size of 0.25 mrad. It was divided in two spectral channels: the Visible channel (VIS) covered the spectral range 0.3-1.1 µm, with a spectral sampling of about 2 nm, the Infrared channel (IR) covered the spectral range 1.05-5.1 µm, with a spectral sampling of about 10 nm. VIRTIS-M was able to acquire simultaneously the spectra of a slit of aligned pixels. Acquisitions with different pointings allowed to produce a monochromatic two-dimensional image of the target (a "cube"), which contained spectral information for each pixel. VIRTIS-M produced cubes having typically a spatial dimension of 256 x 256 (samples x lines) and a spectral dimension of 432 different wavelengths (bands), covering the entire probed spectral range.

VIRTIS-H had a field of view of 0.44 x 1.34 mrad, which means a projected horizontal resolution per pixel of 115 km × 38 km at the apocenter. Its spectral sampling was about 1.5 nm, finer than VIRTIS-M. VIRTIS-H provided spectra (sampled in 432 wavelengths) in the center of VIRTIS-M images.

VIRTIS dataset is made of several acquisitions, for each orbit around Venus, spanning over more than 3000 operational days. Cubes of geometry are associated with every observation: they contain geometrical information of the target, as longitude, latitude, height with respect to the surface, incidence angle, emission angle etc.

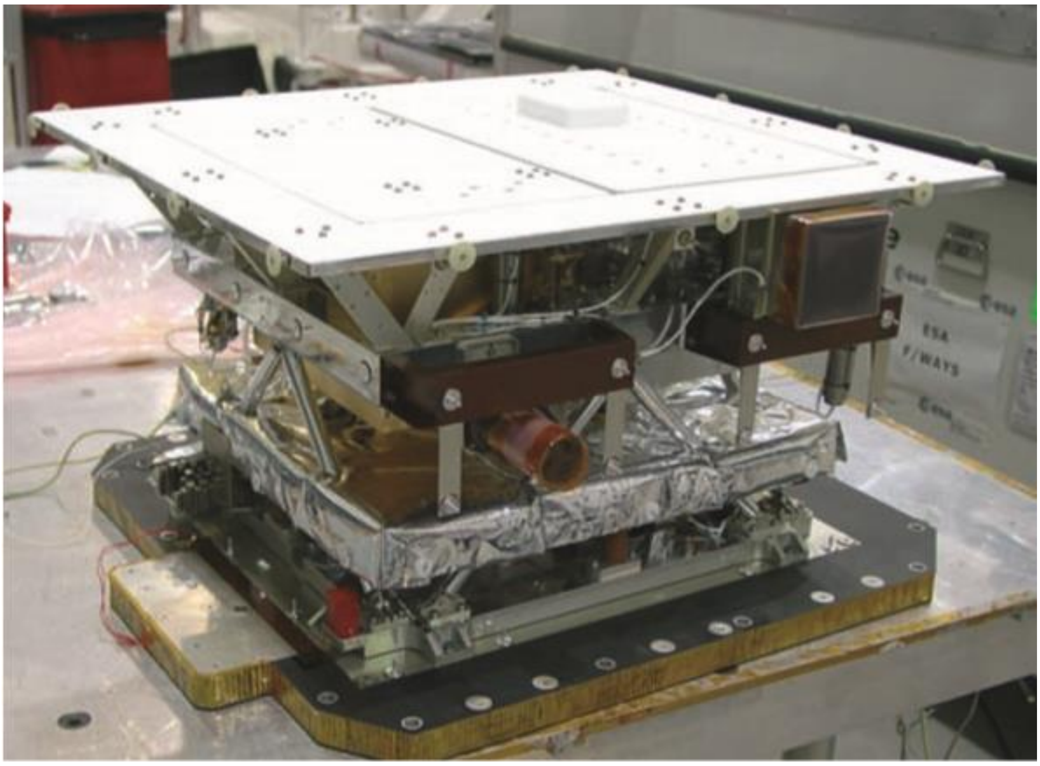

Figure 8: VIRTIS Optics Module. VIRTIS-M and VIRTIS-H are just under the cover (right and left of the image, respectively).

VIRTIS experiment studied the atmosphere composition, leading to accurate measurements of chemical species abundances (Marcq et al., 2008). It investigated the atmospheric dynamics, measuring the wind speeds by tracking the clouds in the UV (top clouds, ~70 km altitude on dayside) and IR (bottom clouds, ~50 km altitude on nightside) and following the time variation of dynamical-tracking species (e.i., CO, OCS) (Marcq et al., 2008). It mapped the surface of Venus in the 1 μm spectral window during nighttime and searched for volcanic and seismic activity (Mueller et al., 2008).

Moreover, radiance spectral distribution contains information about temperature distribution. Since opacity varies with wavelength and the depth from which emergent radiation is emitted varies with opacity, different depths within the atmosphere are sounded by measurements at different wavelengths. Radiation emitted from gases of known distribution, such as carbon dioxide, allows the retrieval of temperature. For this reason, VIRTIS dataset was extensively used to probe the mesosphere temperature structure of Venus (Grassi et al., 2014; Migliorini et al., 2012).

2.1.1 VIRTIS-M temperature retrieval and database selection

VIRTIS-M temperature retrieval by Grassi et al. (2014) is based on Bayesian formalism (Rodgers, 2000). The temperatures have been retrieved from the CO_2 band at 4.3 μm. The presence of CO_2 non-Local Thermal Equilibrium emission and the atmospheric scattering of the sunlight presently limit this study to nighttime only. Constrains, imposed in order to avoid signal saturation of data due to the thermal emission of the instrument, select a dataset of 636 VIRTIS-M cubes, acquired until August 2008. The coverage of this dataset is in general more dense in the southern hemisphere, from mid latitudes to the pole (**Fig. 9**).

In this work, we used the entire dataset of Grassi et al. (2014).

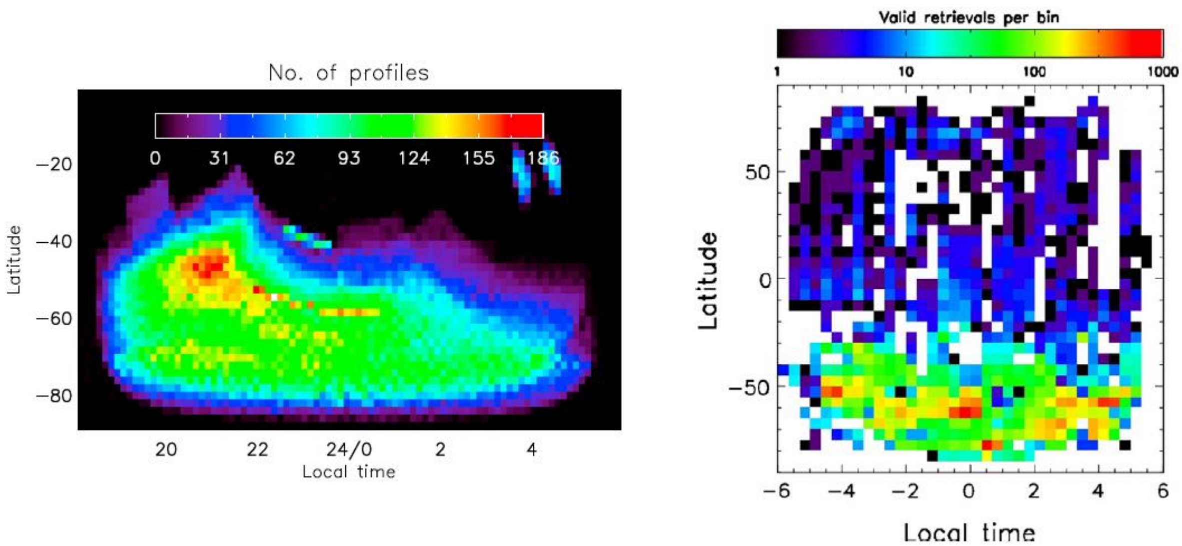

Figure 9: Spatial coverage of the VIRTIS-M dataset adopted for the temperature retrieval (left panel, Grassi et al., 2010). Spatial coverage of the VIRTIS-H dataset adopted for the temperature retrieval (right panel, Migliorini et al., 2012).

2.1.2 VIRTIS-H temperature retrieval and database selection

VIRTIS-H temperature retrieval by Migliorini et al. (2012) relies on a methodology similar to Grassi et al. (2014). This study is limited to 3×10^4 VIRTIS-H spectra collected until November 2013. VIRTIS-H complements the dataset of VIRTIS-M with more observations at low latitude and in the northern hemisphere, even if the larger part of valid retrievals is still in the mid to high latitude range of the southern hemisphere (**Fig. 9**).

In this work, we used the entire dataset of Migliorini et al. (2012).

2.2 Venus Express Radio Science Experiment

VeRa, the Venus Express Radio Science Experiment, used radio signals in two different bands "X" and "S" (3.6 and 13 cm respectively) to study the Venus atmosphere and ionosphere.

VeRa studied:

(1) the atmospheric structure (approximately 40 km to 90 km altitude), basing on vertical profiles of neutral mass density, temperature, and pressure as a function of local time and season;

(2) the presence and properties of small scale and planetary waves, indicating that convection at low latitudes and topographical forcing at high northern latitudes play key roles in the genesis of gravity waves and demonstrating the role of thermal tides in the mesosphere;

(3) the H_2SO_4 vapor layer in the atmosphere by variations in signal intensity;

(4) the ionospheric structure from approximately 80 km to the ionopause (600 km), allowing investigation of the solar wind plasma.

2.2.1 VeRa temperature profiles extraction and database selection

Measurements have been made by directing the High Gain Antenna (HGA) towards the Earth before and after occultation of the spacecraft behind the planetary disc of Venus. The atmosphere caused the radio path to bend: the propagation of the radio signal through the ionosphere and the neutral atmosphere of Venus led to a change in the radio ray path, that produced a wave's phase shift detectable as a frequency shift on Earth. This allowed retrieval of electron density profiles in the ionosphere and profiles of temperature, pressure and neutral number density in the mesosphere and upper troposphere with a high vertical resolution. The radio occultation technique allows to sound deeper below the clouds, probing altitudes deeper than VIRTIS could reach.

Due to the orbit geometry of Venus Express, VeRa coverage of the Northern hemisphere is poor too. Indeed, while the southern hemisphere could be observed with good latitudinal coverage during each occultation season, observations in the northern hemisphere are mainly constrained to latitudes close to the pole (**Fig. 10**).

The VeRa database (**Table 2**) contains a collection of the atmospheric temperature, pressure, absorptivity, sulfuric acid vapor (H_2SO_4) and ionospheric electron density profiles, from each of the VeRa occultation season, along with the latitudinal and local time averaged atmospheric temperature and the corresponding pressure profiles.

In the present study, we selected all nighttime observations form the entire database (local time between 18:00 and 6:00). At the end of the selection phase, we found 657 VeRa profiles corresponding to our requirements, acquired up to November 2013. We used these profiles to perform our study.

Table 2

Occultation season	*DOY start*	*DOY stop*	*Date start*	*Date stop*
01	192	242	2006-07-11	2006-08-30
02	341	031	2006-12-07	2007-01-31
03	116	176	2007-04-26	2007-06-25
04	005	073	2008-01-05	2008-03-13
05	198	215	2008-07-16	2008-08-02
06	304	001	2008-10-30	2009-01-01
07	197	261	2009-07-16	2009-08-18
09	120	192	2010-04-30	2010-07-11
10	017	082	2011-01-17	2011-03-23
11	165	191	2011-06-14	2011-07-10
12	319	007	2011-11-15	2012-01-07
13	087	280	2012-03-27	2012-10-06
14	365	047	2012-12-30	2013-02-16
15	129	210	2013-05-09	2013-07-29
16	298	082	2013-10-25	2014-03-23

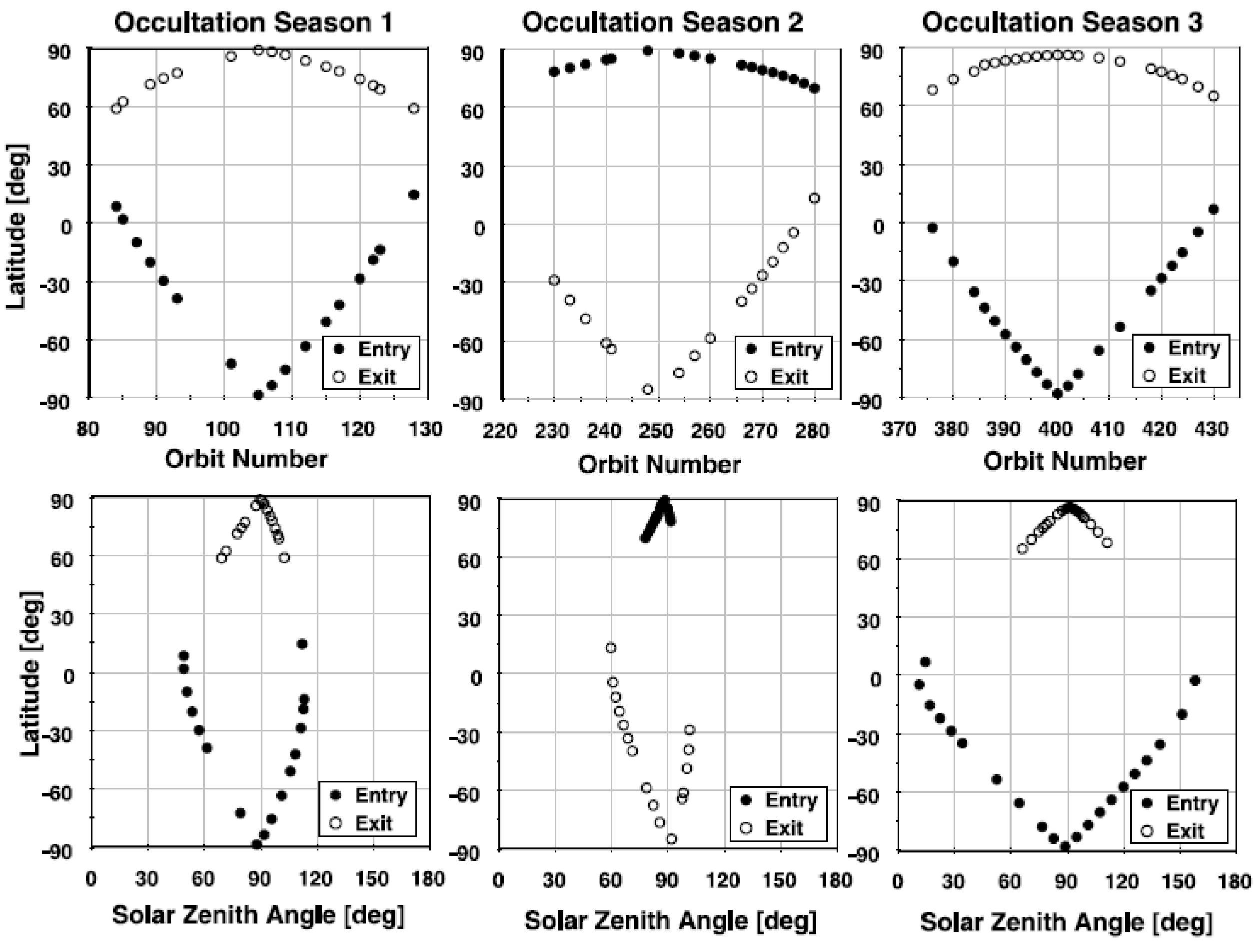

Figure 10: Latitudinal coverage of VeRa season 1, season 2 and season 3 occultations. Full circles: ingress. Empty circles: egress. Tellmann et al. (2009).

3. General Circulation Models

The link between the data gathered by remote sensing measurements and the interpretation of the physical processes active in planetary atmospheres, is made by numerical models: they are valuable instruments to understand the most peculiar features in the atmospheres of planets and the mechanisms behind their dynamics and evolution. Given proper parameters (i.e. radius, gravity, rotation period), boundary conditions, damping and forcing mechanisms, these simulations reproduce the large-scale circulation of a planet, solving the equations governing the atmospheric dynamics. These numerical models are called General Circulation Models (GCMs).

In the attempt of building numerical simulations able to reproduce or predict the available observations of a given planetary body, GCMs combine:

(1) a three-dimensional hydrodynamical core to solve the Navier-Stokes equations for a rotating spherical system (three components of the momentum equation, the continuity equation for density, the thermodynamic equation for potential temperature, the equation of state and the transport equations for tracers);
(2) a radiative transfer solver;
(3) a parameterization of turbulence and convection not resolved by the dynamical core;
(4) a thermal ground model, considering storage and conduction of heat;
(5) a volatile phase change code for the surface or the atmosphere.

Most of the GCMs adopted in planetary science are a re-adaptation of their counterparts for Earth atmosphere. They have been used for the study of several bodies of the Solar System, such as Mars (Forget et al., 1998), Saturn (Spiga et al., 2013), Pluto (Forget et al., 2017), Titan (Lebonnois et al., 2012) and Triton (Vangvichith et al., 2010) and also for conducting scientific investigations on the possible climates of exosolar planets (Turbet et al., 2016).

The planet Venus makes no exception and it has been widely studied thanks to GCMs. However, the extreme physical conditions of its atmosphere and the very important role of the clouds in the energy balance of the planet, impose a much difficult work of adaptation. Producing a GCM for Venus is a big challenge to be accomplished, because of the sensitivity showed by the dynamical core to the initial conditions and the weak forcing of Venus atmosphere (Bengtsson et al., 2013). For this reason, it is difficult to draw conclusions on the circulation obtained with a single model and the capability of that model to conserve the angular momentum, as well as on its sensitivity to many parameters.

In the modelling of Venus, two different approaches have been used through the years:

i) A simplified approach. The radiation scheme is not based on a radiative transfer model; it uses a linear temperature relaxation scheme towards a global-averaged temperature profile obtained from data, plus a perturbations function that takes into account the latitudinal variations of solar radiation within the cloud deck. The circulation is characterized through simplified heating, cooling and friction processes, as well as a rough representation of surface and clouds.

ii) A physically-based approach. It relies on a radiative transfer module that computes the temperature structure self-consistently for each different atmospheric layer. It makes use of realistic topography and specific heat as well. The simulation requires longer computational times, but the outputs point directly toward the physical processes. The aim is not only a qualitative description of the atmosphere of Venus, but a general and comprehensive view of all the active mechanisms.

Either using a simplified or a physically-based approach, some key scientific questions are typically investigated by GCMs and need to be answered in order to understand the real nature of the circulation of Venus:

1. What are the mechanisms that produce fast zonal winds from a slow rotating body?
2. What is the role of the waves, in particular gravity waves and thermal tides;
3. How much is important the topography in surface-atmosphere interactions and in building up superrotation?
4. What is the dynamical role of clouds in the activation of superrotation?

5. What is the origin of the polar temperature distribution, formed by highly variable vortices and cold air areas (the cold collar)?
6. What kind of mechanism permanently forces the cold collar?

At the present state, several simulations qualitatively reproduced the observed superrotation in the modelled atmospheres. However, their results vary from case to case, showing different zonal wind fields under similar initial conditions.

GCMs have also been able to demonstrate the role of the thermal tides in the vertical transportation of angular momentum through the atmosphere, as well as the role of planetary-scale waves and large-scale gravity waves.

However, the thermal structure is still a pending issue in the modelling of Venus. In particular, the polar temperature distribution has not been satisfactory reproduced.

3.1 Simplified Venus General Circulation Models

3.1.1 The CCSR/NIES model

Table 3						
Horizontal resolution	**Grid spacing**	**Altitude coverage**	**Topography**	**Radiating scheme**	**Specific heat**	**Diurnal effects**
5.5° x 5.5°	1.5 km	0-100 km	no	Newtonian cooling	Constant: 10^3 J/Kg/K	No

The **CCSR/NIES** model (Center for Climate System Research/National Institute for Environmental Study) (**Table 3**, **Fig. 11**) is born as an adaptation of a spectral model used for terrestrial modelling (Yamamoto and Takahashi, 2003). A simplified radiative process of zonally uniform solar heating has been assumed and temperatures are relaxed via Newtonian cooling. Solar heating due to CO_2 above 70 km and surface radiative processes are neglected.

The altitude of the maximum heating rate has been adapted to peak 10 km below the cloud top, in order to fully develop a superrotation with 100 m/s at cloud top. No superrotation is activated when the heating rate peaks at cloud top, like in the observations. The circulation is formed by two Hadley cells.

In Yamamoto and Takahashi (2004) and Yamamoto and Takahashi (2006), a new three-dimensional solar heating and Newtonian cooling has been implemented. The peak of the solar heating is located at altitude closer to data, but the heating rate at 55 km has become higher than observations. An equatorial Kelvin wave, a midlatitude Rossby wave – transporting angular momentum towards the equator – and thermally-induced, global scale waves are developed within the model.

Including aerosols, CO_2 and H_2O absorption and emission (Ikeda et al., 2007), the vertical temperature structure below 70 km is found to better agree with observations. Superrotation is maintained by the coupling of the mean meridional circulation with thermal tides, but appear fully developed just above 55 km. Under 55 km, the zonal wind is weaker: only introducing a parametrization for gravity waves, superrotation becomes fully activated.

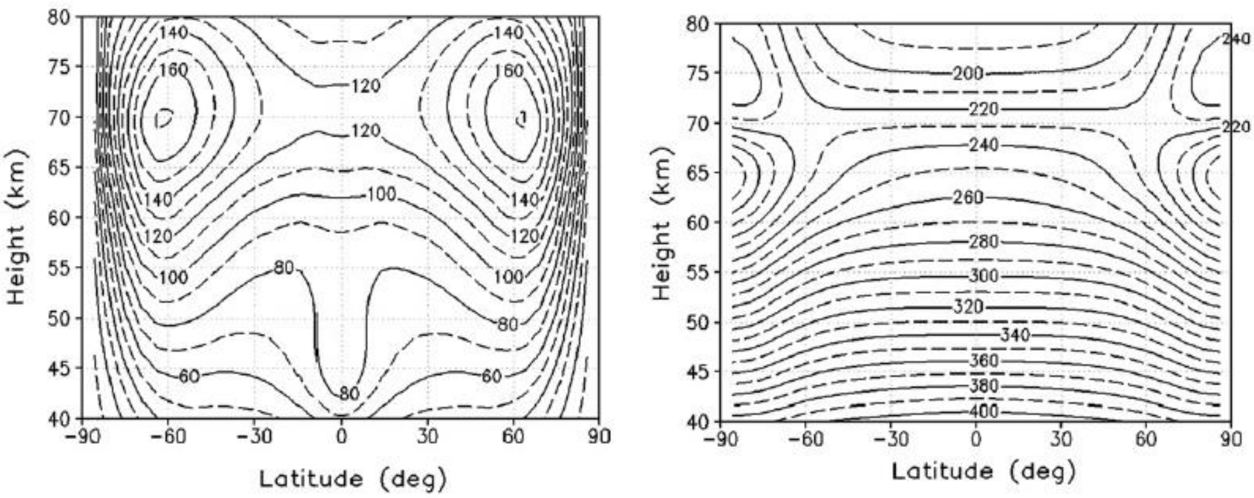

Figure 11: Altitude-latitude distribution of the longitudinally averaged zonal winds (m/s, left panel) and temperatures (K, right panel). Yamamoto and Takahashi (2012).

In Yamamoto and Takahashi (2012, 2015), after inducing superrotation through wave forcing, a Y-shaped wave pattern is formed in the cloud by the superposition of equatorial Kelvin waves and midlatitude Rossby waves, and seems to be modulated by thermal tides. At the same time, an unstable polar vortex is simulated, its life strongly affected by the transient waves: this vortex is sometimes modeled as a dipolar feature, sometimes merges into a monopole or breaks up into a tripole as it stretches. In general, when the transient waves are in phase within the hot oval, the dipole is enhanced, otherwise, the dipolar structure breaks down. The results show some discrepancies with observations: the cold collar is not adequately reproduced, as well as the fine structures observed in the pole, because of the low horizontal resolution utilized in the runs.

3.1.2 The OPUS-V model

Table 4						
Horizontal resolution	**Grid spacing**	**Altitude coverage**	**Topography**	**Radiating scheme**	**Specific heat**	**Diurnal effects**
5° x 5°	3.5 km	0-90 km	flat	Newtonian cooling / radiation scheme	Constant: 10^3 J/Kg/K	no

The **OPUS-V** (Oxford Planetary Unified Simulation model for Venus) (**Table 4**, **Fig. 12**) was developed in Oxford (Lee et al., 2005), using a modification of the UK Meteorological Office Hadley Center Atmospheric Model (HadAM3). It is a finite-difference model, implemented with a simple bulk cloud parametrization (Lee and Richardson, 2010). The radiation scheme is obtained by a relaxation towards Pioneer Venus temperature profile, plus a function that compute the latitudinal variability of the solar absorption rate in the cloud deck (Seiff et al., 1980).

In each hemisphere, zonal jets are produced at 60 km, with a maximum of 45 m/s at mid-latitudes, and an equatorial wind of 35 m/s: this discrepancy with observations may be related to the coarse horizontal resolution, unable to reproduce sub-gridscale convection. Due to the slower zonal winds, both Kelvin waves and Rossby waves in the model display a period longer than in observations. Mid-to-high latitudes cold regions and warm poles are reproduced, at 6 x 10^4 Pa and 7 x 10^3 Pa, respectively, but the contrast with the surroundings is smaller than data; moreover, the fine structure observed in these features does not appear in the GCM.

In Lee et al. (2010) a cloud parameterization has been added, including a close cycle of condensation, evaporation and sedimentation of sulfuric acid particles, where the surface acts as a reservoir for the sulfuric acid liquid. Large "Y"-shape clouds are modeled, similar to those observed. These clouds maintain their large-scale structure over a period of about 7 days, and then become "C"-shape features, due to the interaction of polar and equatorial waves, the former having a longer period than the latter.

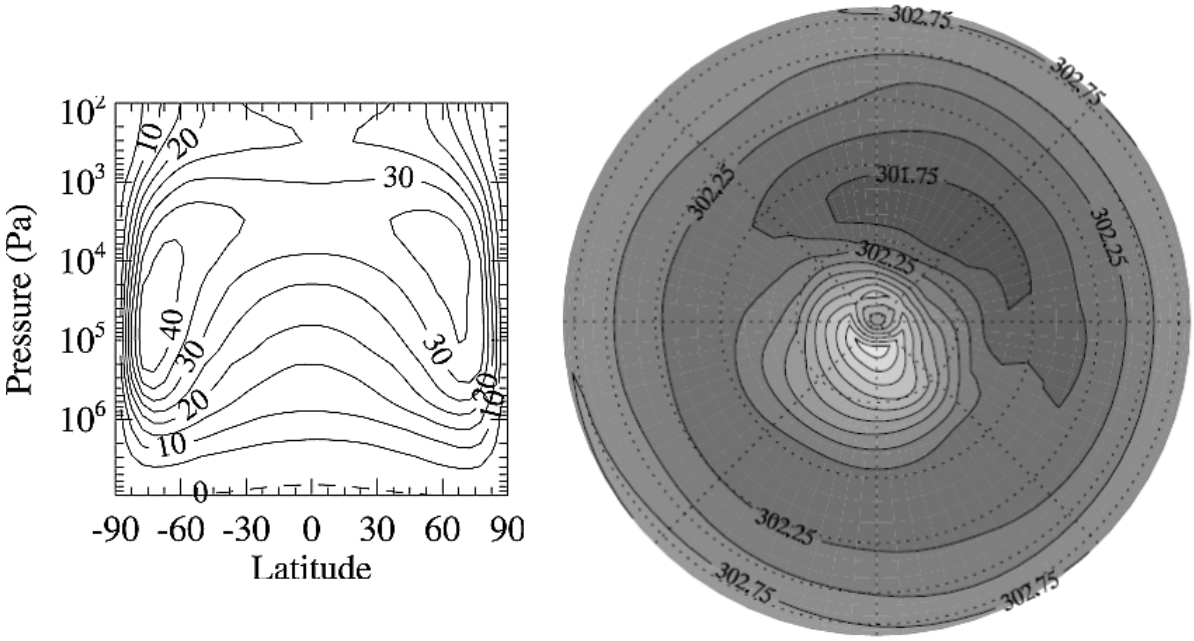

Figure 12: Left panel: pressure-latitude distribution of the longitudinally averaged zonal winds (m/s, Lee et al., 2007). Right panel: polar temperatures at 6 x 10^4 Pa (K, Lee et al., 2005).

Implementing a more realistic radiation scheme to include cloud scattering, Mendonca (2010) and Mendonca et al. (2012), reproduce a long-term variability of the zonal winds in the cloud region, related to large-scale variations in the atmospheric circulation of the low atmosphere. The simulated circulation is characterized in the cloud region by two planetary-scale Hadley cells in each hemisphere, one near the cloud base and another in the upper clouds. The model is still unable to reproduce the strong zonal winds retrieved by data, especially in the lower atmosphere. Even utilizing a realistic topography seems inefficient in building up superrotation.

3.1.3 The AFES model

Table 5						
Horizontal resolution	**Grid spacing**	**Altitude coverage**	**Topography**	**Radiating scheme**	**Specific heat**	**Diurnal effects**
2.8° x 2.8°	1.5 km	0-120 km	no	Newtonian cooling	Constant: 10^3 J/Kg/K	No/yes

The **AFES** model (Atmospheric GCM for the Earth Simulator) (**Table 5**, **Fig. 13**) is a spectral model (Ando et al., 2016) developed in several horizontal and vertical resolution, that uses solar heating rates based on observations by Tomasko et al. (1980).

The simulation was ran with and without solar heating variation: without diurnal effects, the modelled zonal wind fields and temperature profiles are not in agreement with data, vice versa, introducing diurnal variation in the solar heating, model and data become much in agreement, giving a hint of the importance of the thermal tides in the atmospheric circulation of Venus. Superrotation is activated since the first kilometers, with zonal winds showing a mid-latitude peak of 120 m/s at 10^3 Pa, and a strong polar vertical shear which redistribute the angular momentum downward.

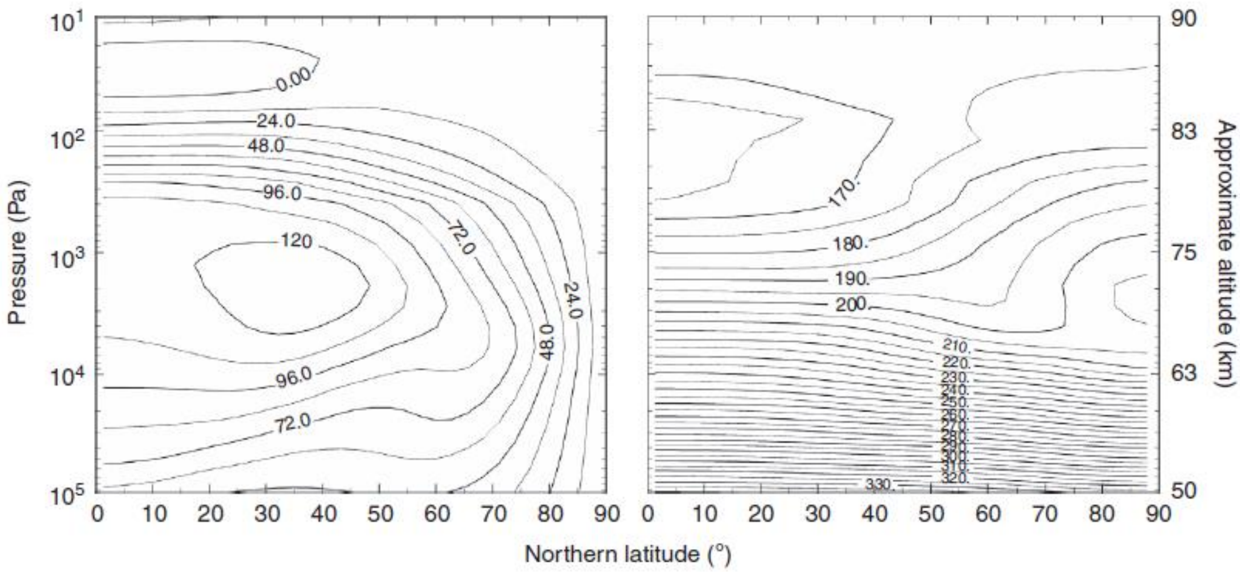

Figure 13: Altitude-latitude (northern hemisphere) distribution of the zonally and temporally averaged zonal winds (m/s, left panel) and temperatures (K, right panel). Ando et al. (2016).

The modelled temperature rises towards the pole at 75 Km and decreases monotonically in the same direction at 60 Km, as observations have revealed. A cold region appears (20 K colder than the surroundings), resembling the cold collar; it is located between 60° and 70°, at an altitude slightly higher than data (Ando et al., 2016). A vortex, rapidly changing in shape, rotates around the pole with an offset of a few degrees.

Also the capability of the GCM to reproduce the warm pole variability and the thermal inversion resembling the cold collar, is directly linked to the presence of a diurnal component in the solar heating. It is shown that the diurnal component causes the model to have a strong downward motion in the polar region, which is responsible of the efficient adiabatic heating that produces the warm pole. When the diurnal component is not activated, the adiabatic heating is less effective, and both the cold region and the warm pole disappear. The role of thermal tides in the GCM is deeply investigated in Takagi et al. (2018), where it was showed that the peak amplitudes of the vertical winds induced by thermal tides are important until higher harmonics: 3^{rd} and 4^{th} thermal tides subharmonics in the AFES-Venus GCM simulations are roughly 50% and 25%, respectively, compared to the 2^{nd} component.

3.2 Physically based Venus General Circulation Models

Table 6

Horizontal resolution	**Grid spacing**	**Altitude coverage**	**Topography**	**Radiating scheme**	**Specific Heat**	**Diurnal effects**
3.75°x1.875°	2 km	0-90 km	Magellan	Full transfer module	Analytical approximation	yes

The dynamical core of the IPSL (Institut Pierre Simon Laplace) Venus GCM (**Table 6**, **Fig. 14**, **Fig. 15**) is based on the Earth model developed at the Laboratoire de Météorologie Dynamique of Paris, which is a latitude-longitude grid finite-difference dynamical core. The model has the capability to zoom over a given region.

Crespin et al. (2006) presented the initial results for a simulation aiming to produce a realistic Venus GCM. In Lebonnois et al. (2010) the GCM included a realistic topography taken from Magellan mission, a realistic diurnal cycle, a temperature dependence of the specific heat $C_p(T)$, in order to get realistic adiabatic lapse rates in the entire atmosphere, and a radiative transfer module which allowed a consistent computation of the temperature field. The boundary layer scheme was taken by Mellor and Yamada (1982).

With these ingredients, peak speeds of 60 m/s are activated at cloud top. Without introducing a realistic topography, superrotation is not activated by the model.

The impact of diurnal cycles has been highlighted by the IPSL Venus GCM. Without diurnal variation, the angular momentum transport is consistent with other

GCMs, with clear high and mid-latitude jets in the winds field. Introducing a diurnal variation, the thermal tides add a significant downward transport at the equator, that weakens the upward and poleward transport due to the mean meridional circulation. This transport allows accumulation of angular momentum at low latitudes and prevents the formation of mid and high-latitude jets.

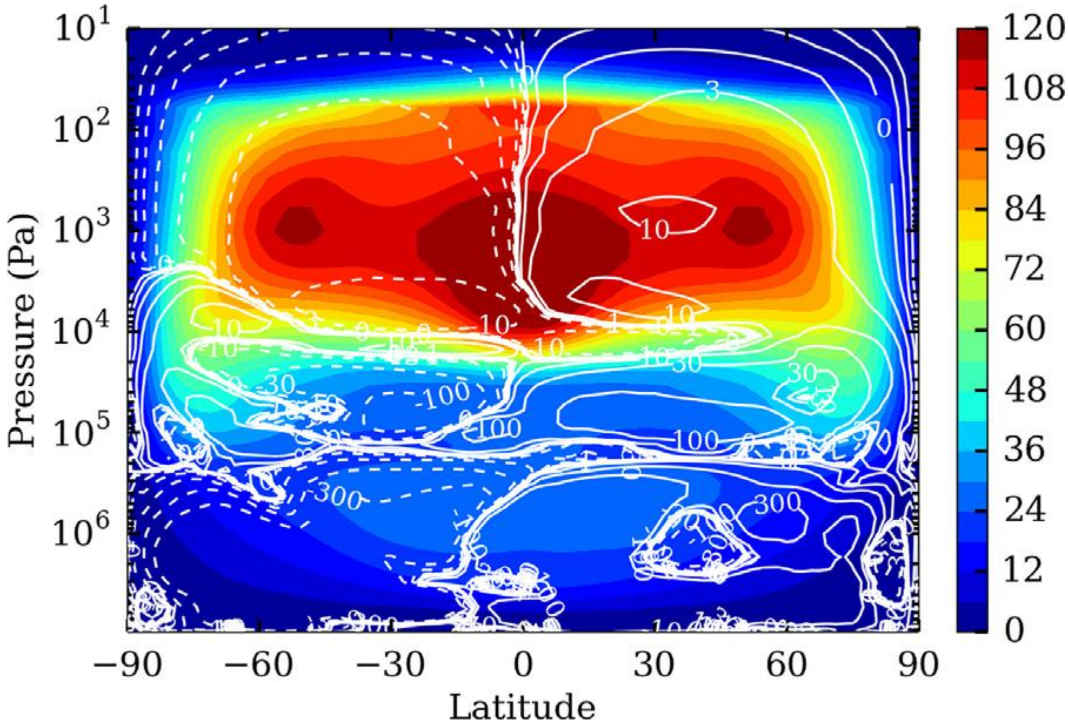

Figure 14: *Pressure-latitude distribution of the mean zonal wind field (m/s). Lebonnois et al. (2016).*

Lebonnois et al. (2016) improved the modelling capabilities of the IPSL Venus GCM. A fully developed superrotation is obtained, both from rest and from an atmosphere already in motion, though winds below the clouds are about half the observed values. The atmospheric waves play a crucial role in transporting angular momentum in Venus atmosphere, with diurnal and semidiurnal tides dominating in the upper clouds level. This work was also capable to successfully reproduce the cold feature displayed in Ando et al. (2016) around 60°-70° latitude, but having just a 10 K contrast with the surroundings. As it happens in Ando et al. (2016), this cold collar resembling feature is formed at an altitude higher than data.

Garate-Lopez and Lebonnois (2018) introduced a latitudinal variability in the parametrization of the clouds, taken by Haus et al. (2014, 2015). This cloud model prescribes the vertical distribution for the three cloud particle modes observed in Venus clouds. It includes a latitudinal modulation of these distributions: a strong decrease of the cloud top altitude is present at 50° latitude, dropping from 70 km to 61 km over both poles, along with a latitudinally dependent scaling of the abundance of the different modes compared to the equatorial vertical distributions.

Solar heating rates are computed from tables that give the heating rates as a function of altitude, solar zenith angle, and latitude. This cloud model is also added in the infrared net exchange matrices. In order to implement the latitudinal variation of the cloud structure in the infrared cooling rates, the net-exchange rate matrices are computed for five latitudinal bins and then interpolated between the central latitudes of each bin. These matrices use correlated-k coefficients of opacity sources, gas and clouds, and consider the CO_2 and H_2O collision-induced absorption.

Because of the uncertainty of the optical properties and the absorption of the solar flux, due to the lack of knowledge of the lower-haze particles composition, some tuning in the radiative transfer module were possible, in order to bring the modelled temperature profile in much agreement with the observed values: as the simulated temperature structure in the deep atmosphere was colder (10 K) than that observed, the solar heating rates were increased in the 30–48 km altitude region by multiplying the values provided by Haus et al. (2015) of a factor of 3. Moreover, some additional continuum to close the infrared windows located in the 3–7 μm range was also needed below the clouds (16 to 48 km), in order to have a best fit of the VIRA and VeGa-2 temperature profiles.

Garate-Lopez and Lebonnois (2018) show that the cloud structure is essential in polar temperature structure and dynamics. The cold region appearing at mid-to-high latitude in Ando et al. (2016) and Lebonnois et al. (2016) weakens, although still present. Even more striking, for the first time a cold collar feature is reproduced at the right altitude (2×10^4 Pa – 4×10^3 Pa) and latitude (poleward of 60°), with a realistic contrast against the surroundings.

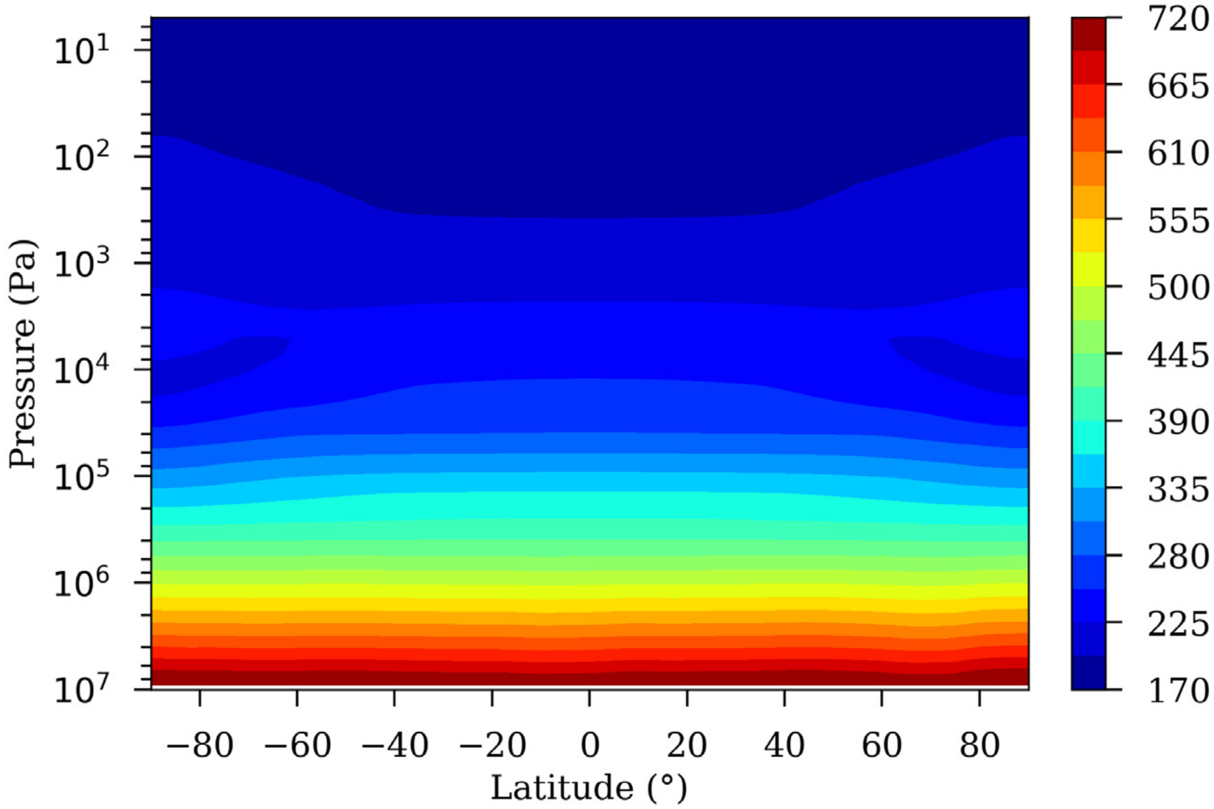

Figure 15: Zonally (360°) and temporally (2 Venus days) averaged temperature field (K). Garate-Lopez and Lebonnois (2018).

At the present state, the simulation in Garate-Lopez and Lebonnois (2018) is the state of the art IPSL Venus GCM, the version that we used in the comparison presented in this work. More details about this simulation and the main characteristics of the radiative transfer scheme, can be found in Garate-Lopez and Lebonnois (2018). An accurate description of the general characteristics of the IPSL Venus GCM and the dynamical core is given in Lebonnois et al. (2010).

4. Data-model comparison: thermal and winds field

Here we present the validation of the current version of the IPSL (Institut Pierre Simon Laplace) Venus GCM, by means of a comparison between the modelled temperatures and winds field and those obtained from data by the Visible and Infrared Thermal Imaging Spectrometer (VIRTIS) and the Venus Express Radio Science Experiment (VeRa) onboard Venus Express.

As already stated in **chapter 2**, in this work we made use of the entire dataset from Grassi et al. (2014) and Migliorini et al. (2012), respectively providing VIRTIS-M and VIRTIS-H temperature retrieval, as well as all nighttime observations form the entire VeRa database (local time between 18:00 and 6:00). The IPSL Venus GCM temperatures and winds are based on the latest version of the model, as obtained by Garate-Lopez and Lebonnois (2018) simulation (see **chapter 3**). While the modelled and observational temperature fields comparison relies on the original data analysis conducted in the present work, starting from Grassi et al. (2014) and Migliorini et al. (2012) temperature retrieval, the wind fields comparison directly uses the data analysis by Sanchez-Lavega et al. (2008), based on VIRTIS data cloud tracking.

In order to validate the global thermal and winds field characterization of the Venus atmosphere obtained with the IPSL Venus GCM, we first analyze the zonally and temporally averaged temperatures and winds field, that are easy to compare with Venus Express observations and give an immediate idea of the overall model reliability.

We limit our analysis to the southern hemisphere, which is richer in observational data. Indeed, we would expect Venus to be a symmetric planet (little axis inclination, no seasonal variations, no macroscopic topographic asymmetries between hemispheres, except for the Maxwell Montes) and we can extend any consideration done for the southern hemisphere to its northern counterpart. Also, because the model itself would eventually show us any possible asymmetry of the planet: the two hemispheres are almost identical in the IPSL Venus GCM. Therefore, from here on, we just report the discussion for the – better observationally covered – southern part of the globe.

The adopted datasets, along with a general description of the VIRTIS and VeRa experiments and the methods of acquisition and retrieval, have been described in **section 2.1** and **section 2.2**. In **section 4.1** we will focus on the thermal field, while in **section 4.2** we will study the winds field in both model and data.

4.1 Average temperature fields

4.1.1 Global average

The horizontally and temporally globally averaged temperature profile (**Fig. 16**), produced in the whole southern hemisphere and during the entire nighttime, have been derived for the IPSL Venus GCM and Venus Express observations. Model output has been averaged over 2 Venus days.

Although this is just a global average, that is not meant for a detailed evaluation of the latitudinal or temporal comparison of model and data, it is clear that some mechanisms are so important in the model to mark significant features in the average field.

This comparison shows a general agreement of model and data, with the simulated temperature very close to VeRa profile into the stable atmosphere of Venus, below the cloud deck (pressures higher than 10^4 Pa). However, while the VeRa profile is smoothly changing through the entire pressures range, with temperatures increasing monotonically from 40 Pa to 10^5 Pa, the IPSL Venus GCM shows some important variations in the slope of its globally averaged temperature profile:

- around 3-4 x 10^3 Pa a cuspid is observed: above and below this level, two sudden changes in the slope;
- between 2 x 10^2 Pa and 3 x 10^3 Pa a broad region of layers warmer (above 4 x 10^2 Pa) and colder (below 4 x 10^2 Pa) than the observed atmosphere. The cold region, in particular, has temperatures 10 K lower than VeRa data.

VIRTIS data are in fair agreement with model in the 2 x 10^2 Pa – 2 x 10^3 Pa range of pressures, but discrepancies arise at altitude higher than 2 x 10^2 Pa and lower than 2 x 10^3 Pa. This is particularly evident in VIRTIS-H case, where we found ~15 K of maximum discrepancy with the model (~ 10^2 Pa).

In Lebonnois et al. (2016) they already noted that the profile of the IPSL Venus GCM is close to the VIRA (Venus International Reference Atmosphere) profile (Seiff al., 1985), with a modelled surface temperature colder than observed, and a temperature in the clouds – and above them – slightly higher (Tellmann et al., 2009; Migliorini et al., 2012; Grassi et al., 2014).

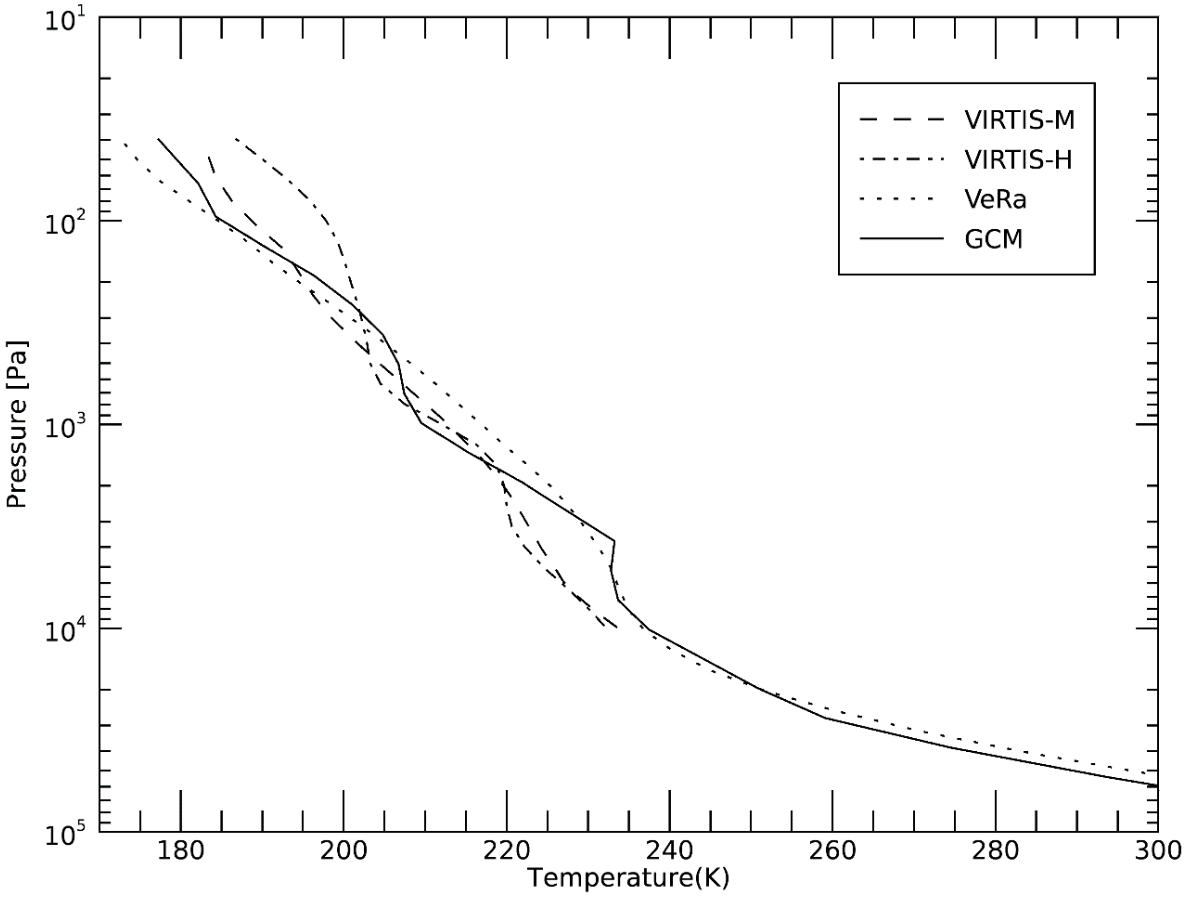

Figure 16: Horizontally and temporally averaged temperature profile (K) for the IPSL Venus GCM (solid line), compared to VIRTIS-M (dashed line), VIRTIS-H (dashed-dotted line) and VeRa (dotted line). For each latitude, profiles are globally averaged over all 360° longitudes and all latitudes of the entire southern hemisphere. Model has been averaged in time over 2 Venus days.

In Garate-Lopez and Lebonnois (2018) (**Fig. 17**), it was found that the new cloud parametrization, on which we based our comparison, allowed a globally averaged temperature profile closer to VIRA: a simulated atmosphere below the clouds warmer than in the previous version of the model, and colder above (Lebonnois et al., 2016).

It must be noted that our comparison is investigating a narrower region in the atmosphere of Venus and thus small fluctuations within the cloud region, that are not evident in **Fig. 17,** are now emerging in **Fig. 16**.

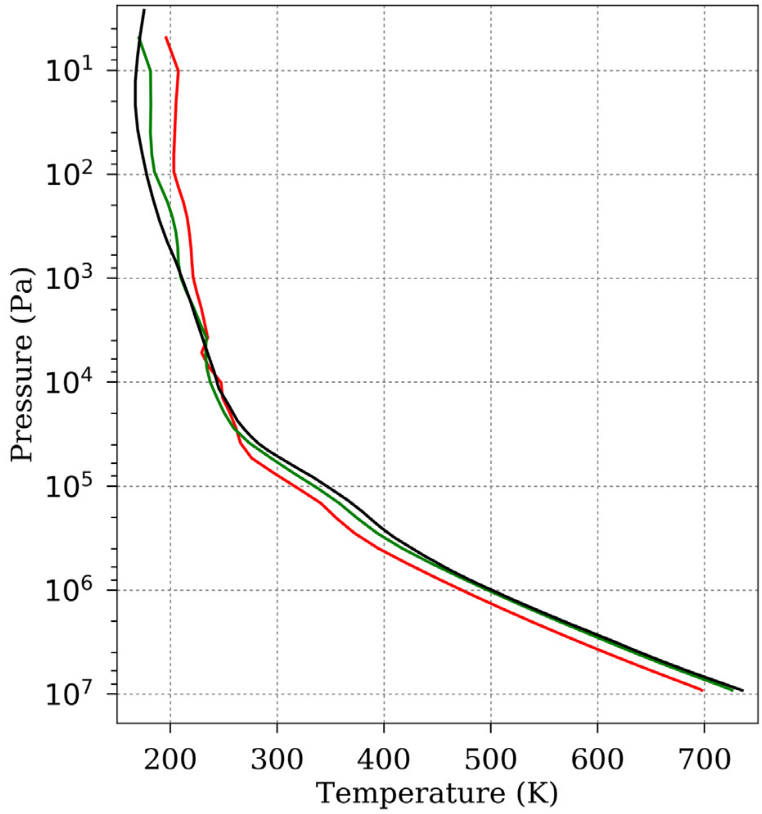

Figure 17: Horizontally and temporally averaged temperature profile (K) for the Lebonnois et al. (2016) IPSL Venus GCM (red line), compared to Garate-Lopez and Lebonnois (2018) (green line) and VIRA reference profile (black line). Profiles are globally averaged over all longitudes and latitudes in each altitude. Model has been averaged in time over 2 Venus days. Garate-Lopez and Lebonnois (2018).

In order to detail the thermal field derived by the IPSL Venus GCM and validate it through the temperatures retrieved by data, we need to disentangle the contribution of each latitude from the average temperature. We produced a map of the zonal and temporal average of the temperature field with respect to both latitude and pressure. The average is performed over 360° of longitude and the entire night (from 18:00 to 6:00 in local time), for both model (using a simulation through 2 Venus days) and data (using the entire available dataset). Results are displayed in **Fig. 18** and **Fig. 19**, for the IPSL Venus GCM and Venus Express data, respectively.

The zonal and temporal average temperature maps, based on observations by VIRTIS-M (**Fig. 19a**), VIRTIS-H (**Fig. 19b**) and VeRa (**Fig. 19c**), immediately show a qualitative agreement with the IPSL Venus GCM.

The altitude-latitude distributions of the modelled temperature field (**Fig. 18**), shows a flat latitudinal trend in the low-to-mid latitude range, around 10^3 Pa – 2 x 10^3 Pa, especially until -60° of latitude. This pressure level represents the border between two different dynamical regions in the modelled temperature distribution. Above this level, temperature increases from the equator to the south pole; on the contrary, below this level, temperature increases towards the equator. The difference between these two regimes becomes clearer at high latitude, where the slope of this trend is higher in both the upper and the bottom atmosphere, although the sign is different.

On the contrary, the data temperature distributions around 10^3 Pa, display a latitudinal upward trend from the equator to the pole, particularly evident for VIRTIS-M, where the latitudinal profile is monotonically changing in the entire hemisphere, and VeRa, where a flat trend is observed equatorward of -40°, followed by a poleward rising tendency. The discrepancies between modelled and observational latitudinal trend may be related to the adopted haze distribution (Hauss et al., 2014; 2015), that is not well constrained. However, it is not surprising to see – in all the three observations-based maps – the two dynamical regions that we see in the upper and bottom atmosphere of the GCM: this is a known behavior of Venus atmosphere (see **section 1.2**).

Venus atmosphere shows different vertical behaviors at different latitudes: in general, equatorward of −50°, the modelled temperature field seems to be homogeneously stratified, no complex features are present and no abrupt variation of the temperature. Moreover, in this region, the temperature trend is monotonically decreasing from the bottom to the top of the atmosphere, ranging from ~364 K to ~165 K (image saturated). On the contrary, at higher latitudes a more complex behavior is modelled: there are two cold elongations extending downward and poleward from −60°, one at pressures higher than 4×10^3 Pa and another at pressures lower than 2×10^3 Pa. The former, resembling the observed cold collar, reaches the south pole and thus is not yet a completely isolated feature; it shows temperatures about 15–20 K colder than the surroundings and is coupled with a partially formed warm pole (5×10^3 Pa – 10^4 Pa). The latter is coupled with another warmer region at high latitudes, which extends almost 10 Pa into the vertical in the temperature field, until 2×10^2 Pa. The absolute temperature of the upper cold and warm regions, as well as the thermal contrast they maintain with their surroundings, are lower than that of the regions at ~10^4 Pa (64 km).

The complex behavior displayed in the IPSL Venus GCM temperature profile and the different features reproduced, are also observed in the three different datasets. Basing on this comparison, the most striking result of the IPSL Venus GCM is the capability to simulate the major feature associated to the cold collar with a remarkable resemblance with VIRTIS-H, VIRTIS-M and VeRa data. The modelled temperatures within this region are similar to those that are observed and the general contrast between the warm and cold areas close to the pole in the data-based maps and in the simulated one, is very similar too. Moreover, both the simulated and the observed cold collar appear at comparable pressure levels (roughly below 3–4 × 10^3 Pa) and latitudes (poleward of −60°) and both features elongate towards the pole at increasing pressures, just beneath the warm polar region. However, in VeRa observations is particularly clear that the cold collar is an enclosed feature that doesn't reach the pole, and the warm pole is fully formed and more vertically extended than the one reproduced by the model. This discrepancy is explained thanks to the grid currently used in the model, which is based on a longitude-latitude scheme with a longitudinal polar filter, that reduces the latitudinal resolution and the reliability of the IPSL Venus GCM at latitudes close to the pole. No warm region is found in data at pressures lower than 10^3 Pa and consequently, no abrupt variation of the temperature – like the one present in the model at -70° - is observed in the high atmosphere of VIRTIS and VeRa data.

Deeper in the atmosphere, into the bottom clouds layers (under 3 x 10^4 Pa), the only probing experiment is VeRa. In this region, Venus atmosphere is more stable and both the temporal and latitudinal variation become minimal. The IPSL Venus GCM agreement with VeRa data, confirms the first look conclusions of **Fig. 16**.

Beside of the little discrepancies that we found on the border between the two different regimes, we can assert the overall similarity of model and data altitude-latitude distributions and the capability of the IPSL Venus GCM to satisfactory reproduce the general temperature structure and also the complex temperature pattern observed in the subsolar and polar region. Indeed, the modelled thermal structure displays a good agreement with data, and the cold collar is successfully reproduced at latitudes poleward than −60°, with an extent and a behavior close to the observed ones.

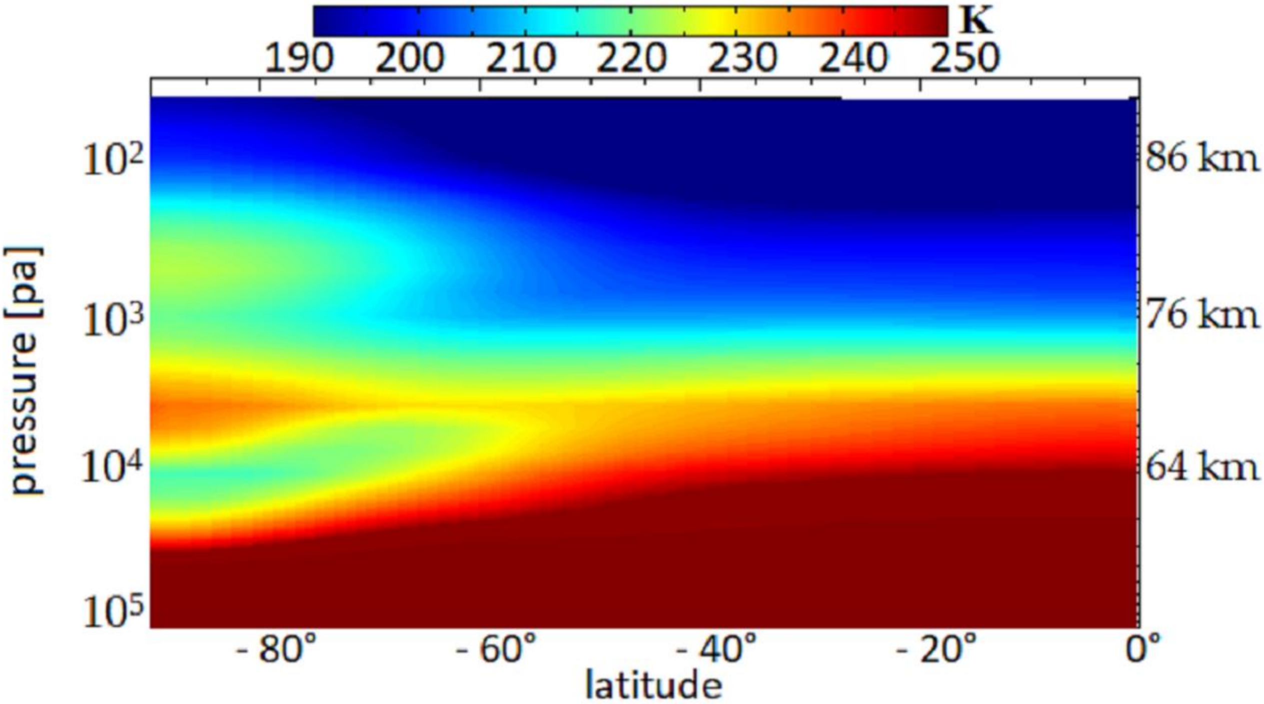

Figure 18: Altitude–latitude distribution of the zonal and temporal average temperature field (K) for the IPSL Venus GCM. The average has been obtained over 360° of longitude and the entire nighttime, over 2 Vd. The cold collar is the green and cyan oval-shape feature poleward of -60°. Scarica et al. (2019).

However, even if the GCM was qualitatively capable to reproduce the polar temperature pattern, here resides also the most crucial discrepancy with data. It is clear from this comparison, that the most important differences between the IPSL Venus GCM simulation and Venus Express observations regarding the mean temperature field are the cold elongation around 10^3 Pa and the vertical extension of the warm region associated with it (see **section 5.5** for further discussion).

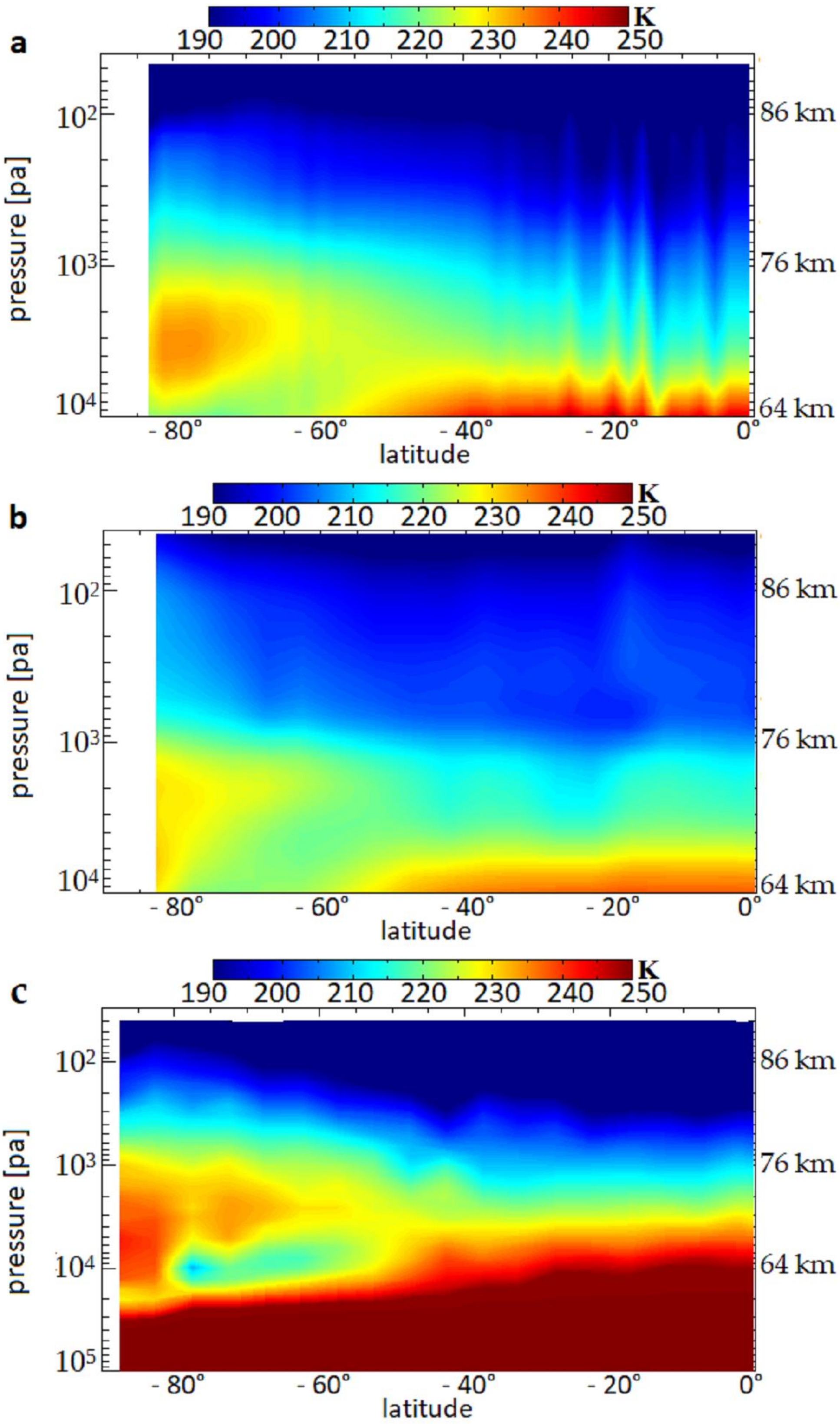

Figure 19: Altitude-latitude distribution of the zonal and temporal average temperature field (K). (a) VIRTIS-M; (b) VIRTIS-H; (c) VeRa. The average has been obtained over 360° of longitude and the entire nighttime, over 2 Vd. The altitude range of VeRa extends deeper, allowing us to see the cold collar as an enclosed feature. Scarica et al. (2019).

4.1.2 Vertical gradient

In order to test more thoroughly the vertical temperature gradient simulated by the GCM, we produced several cuts in the average temperature fields, displayed **Fig. 18** and **Fig. 19** and we built a latitude-by-latitude comparison of GCM and data average temperatures. High-latitude profiles are then compared to low and mid latitude samples. The averages have been obtained over the entire nighttime and 360° of longitude, for both model and data. Here (**Fig. 20**, **Fig. 21** and **Fig. 22**), we show a set of ad-hoc reference latitudes (-75°, -45° and -15°), characteristic of high, mid and low latitude samples.

- At -75° (**Fig. 20**), the average temperature in the simulation peaks at 235 K on a pressure level of 3-4 × 10^3 Pa (roughly 69 km). This is consistent with VIRTIS-M and VeRa profiles. The peak in VIRTIS-H data is less pronounced, is located at a slightly lower temperature (230 K) and at a lower pressure level (2 × 10^3 Pa) than GCM output, VIRTIS-M and VeRa data. Deeper in the atmosphere (between 4 × 10^3 Pa and 2 × 10^4 Pa), model and data share the cold collar temperature inversion: after peaking, the modelled temperature decreases at higher pressure levels and reaches values 15 K lower than peak. The contrast between the peak and the deepest region is consistent with VIRTIS-M and VeRa data. However, the transition between the warm layer above the cold collar and the cold collar itself, takes place at a shorter vertical distance in the model: thus, the peak of the profile is sharper in the GCM than in data. Between 5 × 10^2 Pa and 2 × 10^3 Pa, the GCM displays a second temperature inversion, coinciding with the upper cold elongation (the second inversion) discussed in the altitude-latitude distribution maps (see **section 4.1.1**). This feature does not appear in either VIRTIS-M or VeRa data profiles, that are instead characterized by a monotonic increase of the temperature from the top of the observed atmosphere to the cloud top at 4 × 10^3 Pa. On the other hand, between 10^2 and 4 × 10^2 Pa, VIRTIS-H data display a flatter trend then VIRTIS-M and VeRa. However, even if resembling the modelled second temperature inversion, this flat trend never becomes a complete inversion of the temperature and the double peak structure that is formed in the model appears far more pronounced than in VIRTIS-H data.

- At -45° (**Fig. 21**), model and data average temperature profiles show an overall qualitative agreement. The abrupt changes displayed in the high-latitude modelled atmosphere, fade, and the IPSL Venus GCM tend to better agree with observations. Indeed, the cold collar disappears in both model and data, and no upper cold elongation is produced by the GCM. From our analysis results that this modelled temperature inversion shows no sign at all at lower latitudes (**Fig. 22**) and have an impact only at mid-to-high latitude: it starts as an isothermal feature at around −55° and then evolves into a clear inversion as latitude increases towards the south pole. For this reason, at this latitude, both data and GCM profiles display a rising temperature from the top to the bottom of our accessible pressure range. Moving in the pressures range between 3×10^3 Pa and 10^4 Pa, we see that GCM temperatures are 5–10 K warmer than VIRTIS data. Instead, at low pressures (below 2×10^2 Pa), the discrepancy of model and VIRTIS data profile is about 10 K, slightly more than the random errors due to the retrieval method, that are roughly 4–5 K in this pressure range (Grassi et al., 2014; Migliorini et al., 2012). We have to consider that the strong variability of the Venus atmosphere, also in terms of temperature profiles, may be important for short-term evolution and using poor statistical coverage data in the average. Deeper into the atmosphere (pressure higher than 3×10^4 Pa), the only available observations are VeRa data, and they agree with the simulation, as it was for the horizontally and temporally average profile of **Fig. 16**. In general, we note that VeRa data and the IPSL Venus GCM are in much agreement in the entire range of analysis, apart from the pressure levels between 3×10^3 Pa and 3×10^4 Pa, where still a notable discrepancy of 5-10 K is noted.
- At -15° (**Fig. 22**), a good consistency of model and data profiles is seen in the mid-pressure range (5×10^2 - 2×10^3 Pa), where random retrieval errors in VIRTIS-M and VIRTIS-H are smaller (about 1 K for both VIRTIS-M and VIRTIS-H, Grassi et al., 2014; Migliorini et al., 2012). On the other hand, at the lowest and highest pressure levels of the atmosphere probed by VIRTIS, a broad difference is visible between the GCM average temperature profile and VIRTIS data, up to 15–20 K around 10^2 Pa. This large discrepancy may be partially due to the combined effect of the low spatial coverage of VIRTIS at low latitudes (**Fig. 9**) and the intrinsic errors of the temperature retrieval

method at high and low pressures. We still notice a flattened trend in the VIRTIS-H profile, at pressures below 5×10^2 Pa. This feature is shown for the entire southern hemisphere of VIRTIS-H data, and thus is not related to the mid-to-high latitude upper cold elongation that we see in the model. The GCM profile remains consistent with the VeRa one through the entire pressures range. **Figure 23** reports the same temperature profiles: GCM is compared to VIRTIS-M and VIRTIS-H, which are provided of error bars, obtained by the standard deviation.

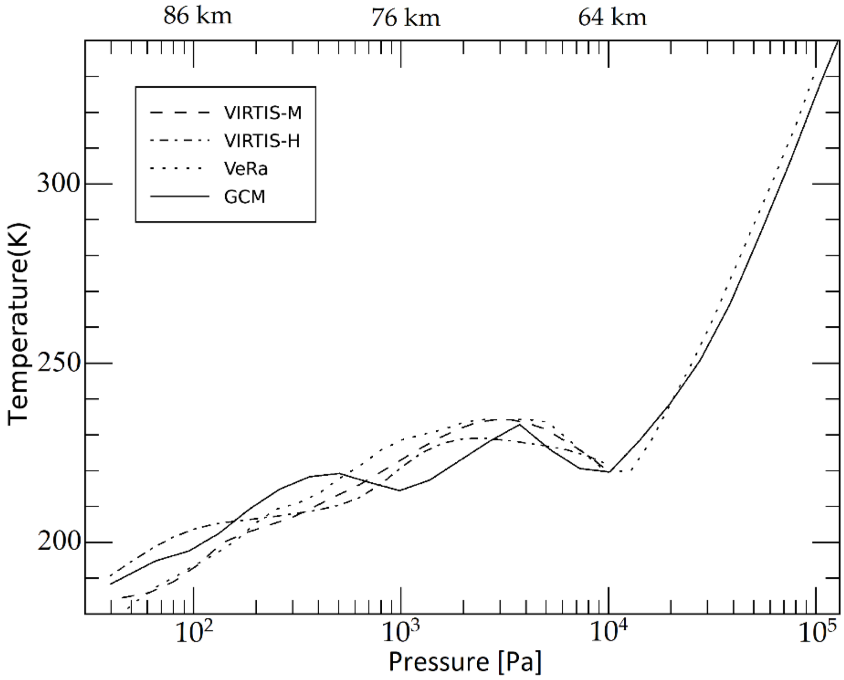

Figure 20: Average temperature profiles (K) for the IPSL Venus GCM (solid line), VIRTIS-M data (dashed line), VIRTIS-H data (dotted-dashed line) and VeRa data (dotted line), at -75°. Average has been obtained over 360° of longitude and the entire nighttime, over 2 Vd. Scarica et al. (2019).

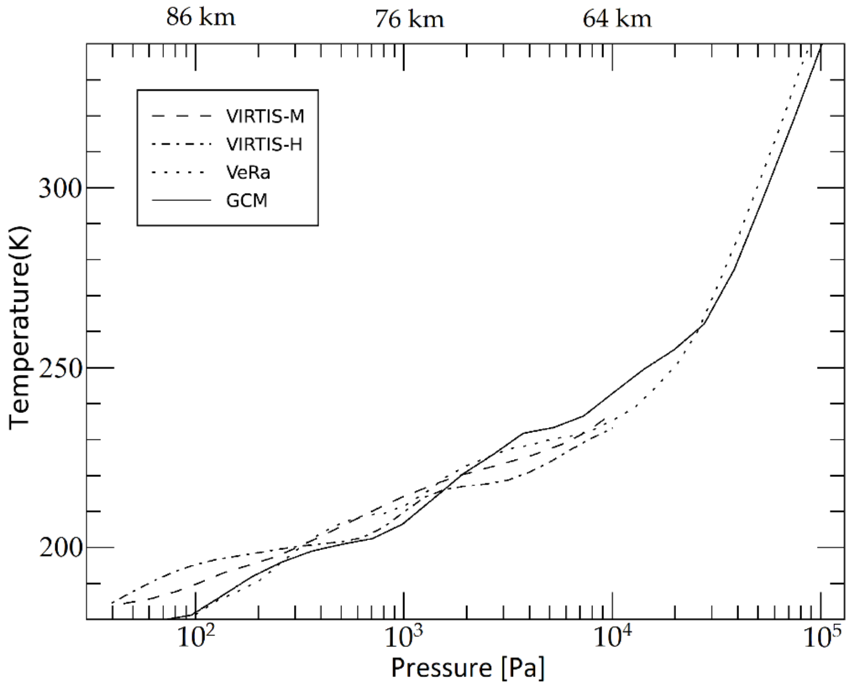

Figure 21: Average temperature profiles (K) for the IPSL Venus GCM (solid line), VIRTIS-M data (dashed line), VIRTIS-H data (dotted-dashed line) and VeRa data (dotted line), at -45°. Average has been obtained over 360° of longitude and the entire nighttime, over 2 Vd. Scarica et al. (2019).

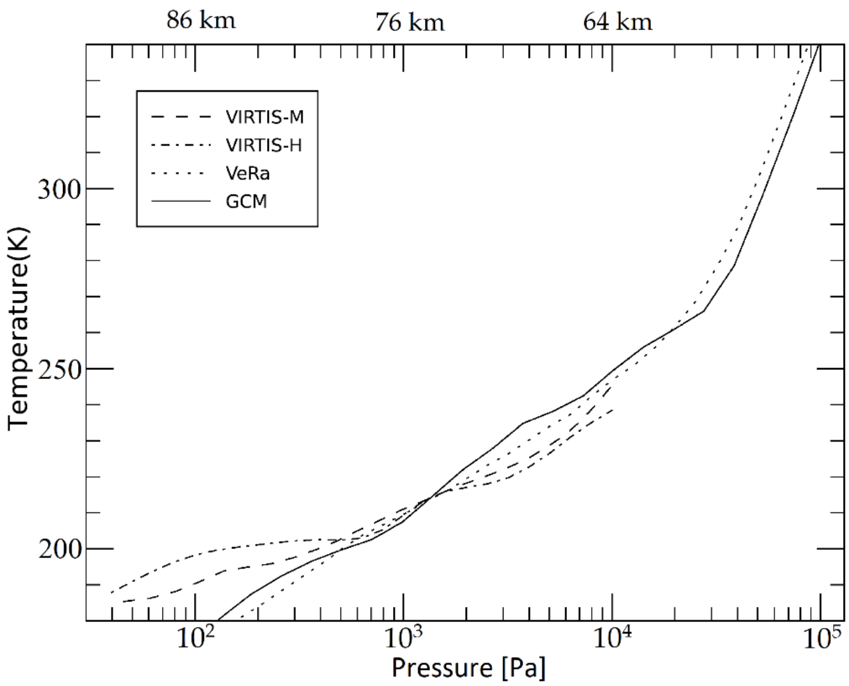

Figure 22: Average temperature profiles (K) for the IPSL Venus GCM (solid line), VIRTIS-M data (dashed line), VIRTIS-H data (dotted-dashed line) and VeRa data (dotted line), at -15°. Average has been obtained over 360° of longitude and the entire nighttime, over 2 Vd. Scarica et al. (2019).

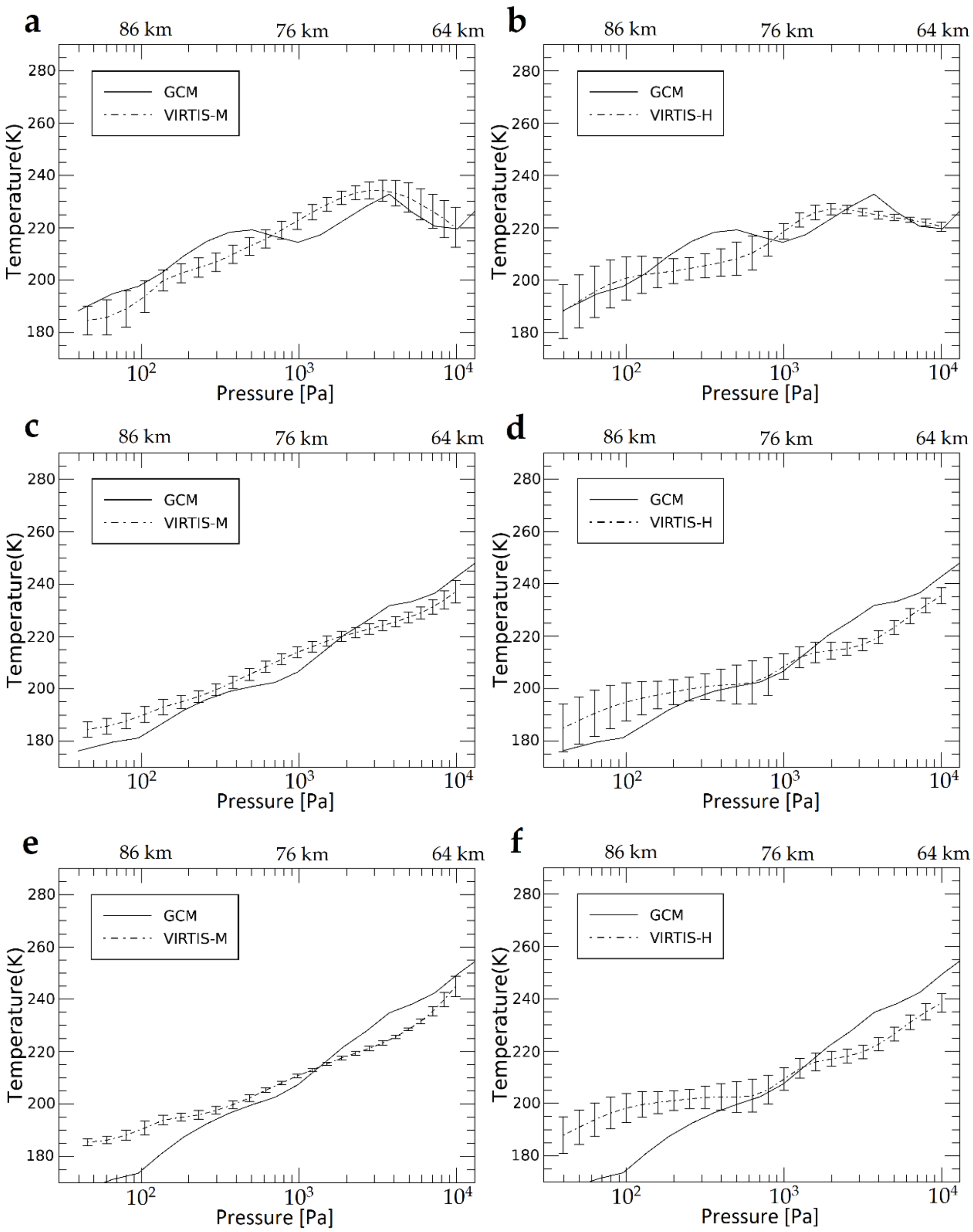

Figure 23: Average temperature profiles (K) for the IPSL Venus GCM (solid line) and data (VIRTIS-M and VIRTIS-H), provided with error bars obtained by the standard deviation. (a) GCM vs VIRTIS-M data at -75°, (b) GCM vs VIRTIS-H data at -75°, (c) GCM vs VIRTIS-M data at -45°, (d) GCM vs VIRTIS-H data at -45°, (e) GCM vs VIRTIS-M data at -15°, (f) GCM vs VIRTIS-H data at -15°.

The less smoothness of the horizontally and temporally averaged temperature profile of the model, with respect to the observational profiles, reported in **Fig. 16**, is now explained with the puzzling polar and subpolar features and the upper cold elongation:

- the cuspid at 3-4 x 10^3 Pa is clearly related to the warm peak and the cold collar at -75°, which contrast is larger than the observed one;
- the broad region between 2 x 10^2 Pa and 3 x 10^3 Pa is related to the second inversion, the modelled upper cold elongation that is not found in any data.

4.1.3 Latitudinal profiles

The modelled latitudinal temperature gradient is compared with observations. We produced cuts along given pressure levels and we built a detailed comparison of GCM and data average temperatures for each different pressure. The averages have been obtained over the entire nighttime and 360° of longitude, for both model and data. Here (**Fig. 24**, **Fig. 25** and **Fig. 26**), we show and discuss several cases, that cover the different regimes in Venus atmosphere: 10^2 Pa (~ 86 km) is reported in **Fig. 24**, 10^3 Pa (~ 76 km) in **Fig. 25** and 10^4 Pa (~ 64 km) in **Fig. 26**.

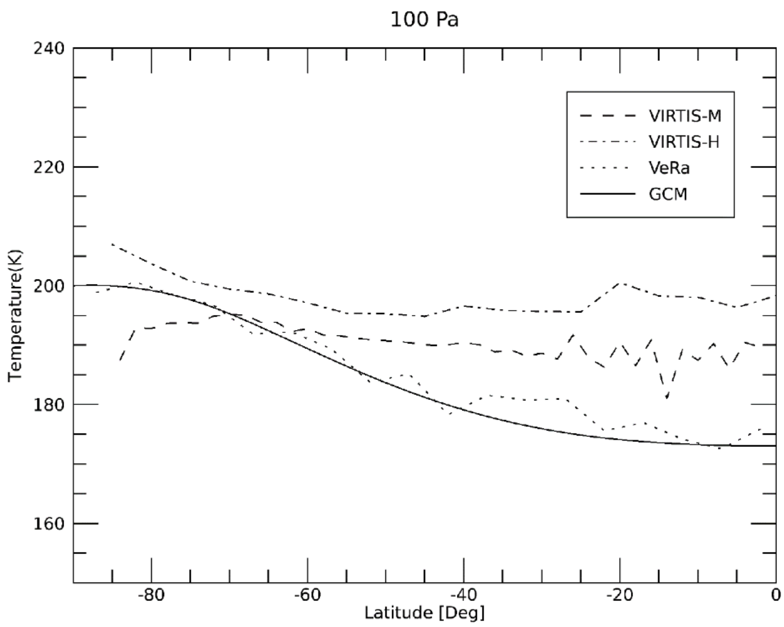

Figure 24: Latitudinal profiles of the temperature (K, zonal and temporal average over 2 Vd) at 10^2 Pa (~86 km). GCM is the solid line, VIRTIS-M is dashed, VIRTIS-H is dashed-dotted and VeRa is dotted.

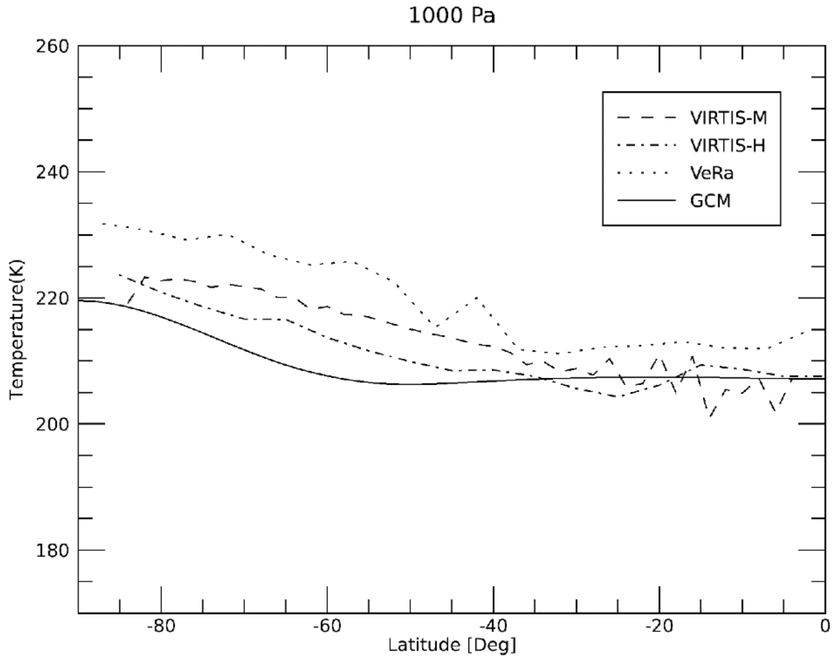

Figure 25: Latitudinal profiles of the temperature (K, zonal and temporal average over 2 Vd) at 10^3 Pa (~76 km). GCM is the solid line, VIRTIS-M is dashed, VIRTIS-H is dashed-dotted and VeRa is dotted.

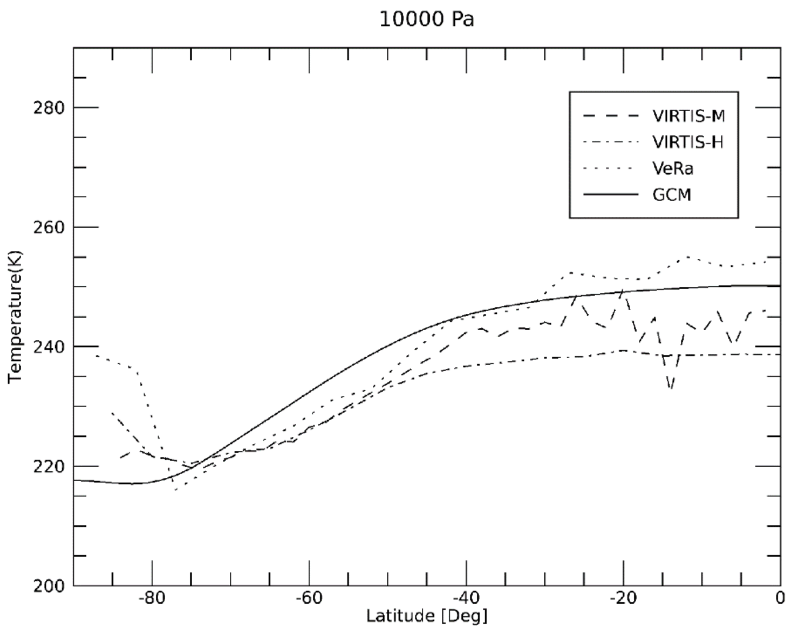

Figure 26*:* Latitudinal profiles of temperature (K, zonal and temporal average over 2 Vd) at 10^4 Pa (~65 km). GCM is the solid line, VIRTIS-M is dashed, VIRTIS-H is dashed-dotted and VeRa is dotted.

- At 10^2 Pa (**Fig. 24**), both model and data temperatures increase towards the pole, as already reported (see **section 4.1.1**). We note that the IPSL Venus GCM adequately follows the trend of VeRa temperature profile. VIRTIS data (both -M and -H) have higher low-latitude temperatures but tend to high-latitude temperatures very similar to the model. This means that the latitudinal profile in VIRTIS data appears to be sharper than in the model.
- At 10^3 Pa (**Fig. 25**), there is a very good agreement of model and data (especially VIRTIS). In particular, the low latitude modelled temperature gradient is very consistent with the three datasets, while profiles tend to diverge poleward of -40°, because of the second inversion of the temperature produced in the model.
- At 10^4 Pa (**Fig. 26),** it is evident the change of regime: warmer air at the equator and colder close to the pole. Altogether, we confirm a fair agreement of model and data, though the observed warm pole is not reproduced in the IPSL Venus GCM (modelled cold collar extending until the pole). The increasing equatorward model-data discrepancies may be due to the low spatial coverage.

Discrepancies between the modelled and the observational latitudinal temperature gradient are consistent with **Fig. 24**, in agreement with the discussion of **section 4.1.1**.

4.1.3 Polar temperature

We now inspect the horizontal structure of both thermal inversions using polar projections. **Fig. 27** shows the nighttime temperature field of the southern hemisphere at 7×10^3 Pa (~64 km altitude), where the cold collar resides, as observed by VIRTIS-M data (**Fig. 27a**) and simulated by the model (**Fig. 27b**). For this study, we produced a different output, having longitude locked to local time (each local time corresponds to a different longitude). Thus, the radial coordinate of the grid corresponds to latitude, while the angular coordinate to local time, going from the evening to the morning terminator clockwise. The modelled temperature field in **Fig. 27b** is an average over 2 Venus days, while the VIRTIS-M temperature field in **Fig. 27a** is obtained with all available data.

Even if there is a lack of observations close to the equator and to the morning and evening terminators, we can conclude that the GCM generally agrees with data: the first half of the night is warmer than the second one, in both the simulation and VIRTIS-M data, and local minima and maxima that appear in the model are consistent with observations.

The cold collar appears as a completely formed structure in the IPSL Venus GCM, well distinguished from the surrounding environment. The modelled atmosphere between -60° and -85° is colder than the rest of the latitudes, being on average ~25 K colder than the equator and about 10 K colder than the pole. This simulated feature displays a strong resemblance with the data: the altitude where the feature is peaking (around 64 km, roughly 10^4 Pa) and the temperature values (about 220 K) obtained in the simulation are consistent with observations, as well as the phase in local time. Both GCM and VIRTIS-M cold collars are more pronounced after midnight and extend towards the morning terminator, while displaying a similar contrast with low latitude. The GCM cold collar shows its maximum at latitudes slightly higher than −70°, the observed one a few degrees equatorward, about −65°. The cold collar temperature contrast with the warm core temperature is larger in data than in the model (15 K against 10 K); infact, modelled high latitudes suffer from poor spatial resolution, as already noted.

Although the structure simulated within the inner core is smoother than obtained by other GCMs, like Yamamoto and Takahashi (2015) and Ando et al. (2016), that use spectral dynamical cores that do not have singularities at the pole, the IPSL Venus GCM is capable to reproduce the cold collar at an altitude (~64 km) and with temperature values (~220 K) consistent with observations.

Fig. 28 shows the model-data comparison at 2×10^3 Pa pressure level (corresponding to the upper cold elongation), where the observed nighttime temperature fields (**Fig. 28a**) and the simulated (**Fig. 28b**) display clear differences. We already know, from the altitude–latitude distribution that, at this altitude, VIRTIS-M shows a monotonic increasing regime (**Fig. 18a**): the temperatures rise from the equator to the pole, with retrieved values spanning in a range of 10–15 K. While the temperature range in the model is in general similar to that observed, the horizontal distribution is completely different. In the GCM output, temperatures become colder from the equator to mid-latitude, and then starts to become warmer and warmer poleward. Temperature values around -80° are similar in the GCM and VIRTIS-M fields, therefore, the transition between mid and high latitudes in the second half of the night is sharper in the simulation than in the observations. In the GCM map, a warm area is visible in the first part of the night, close to the evening terminator; in the VIRTIS-M map, this region also appears to be warmer.

The thermal structure of Venus atmosphere has been studied previously (Tellmann et al., 2009; Haus et al., 2014; Grassi et al., 2010) and all these works showed a cold collar region with its thermal inversion, but none of these temperature maps obtained from observations showed the upper inversion that appeared in Lebonnois et al. (2016) and Ando et al. (2016). Ando et al. (2016) identified this feature as the cold collar. However, comparing their results with **Fig. 18** and **Fig. 28** in this work, we conclude that their cold elongation is more similar to our upper inversion than to the inversion corresponding to the cold collar.

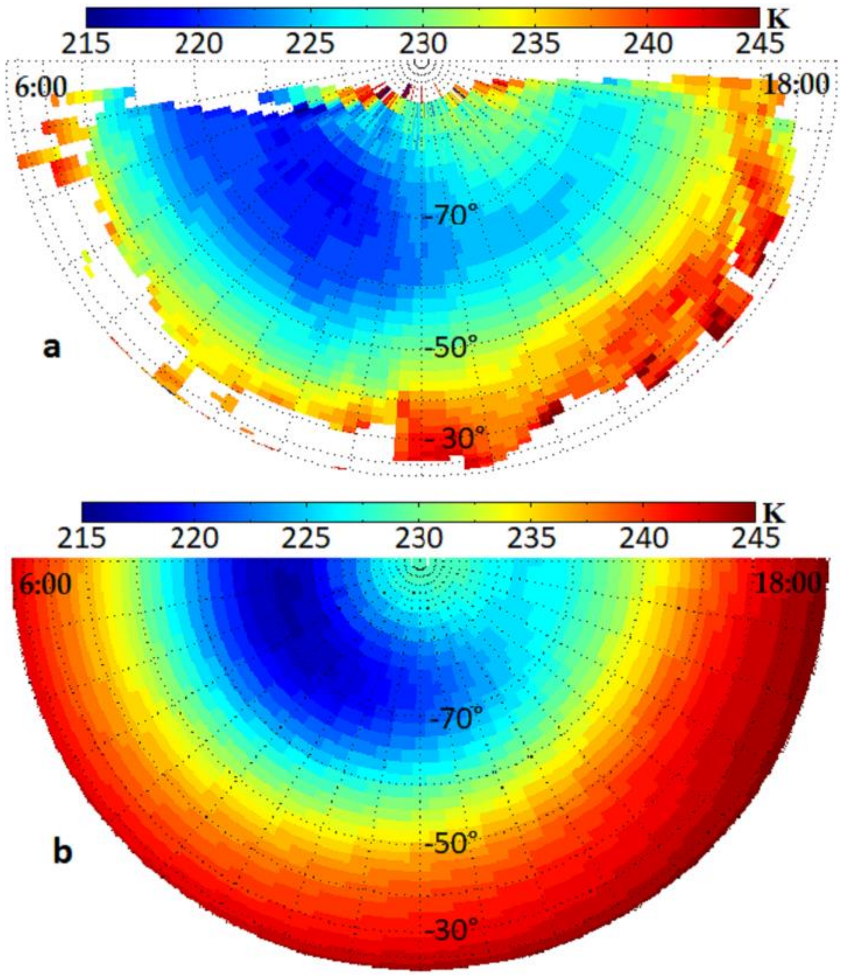

Figure 27*:* Nighttime polar temperature field (K) at 7×10^3 Pa (~64 km) for (a) VIRTIS-M and (b) the IPSL Venus GCM simulation. The radial coordinate of the grid corresponds to latitude (from 0° to -90°) and the angular coordinate to local time (from 18:00 to 6:00, clockwise). Scarica et al. (2019).

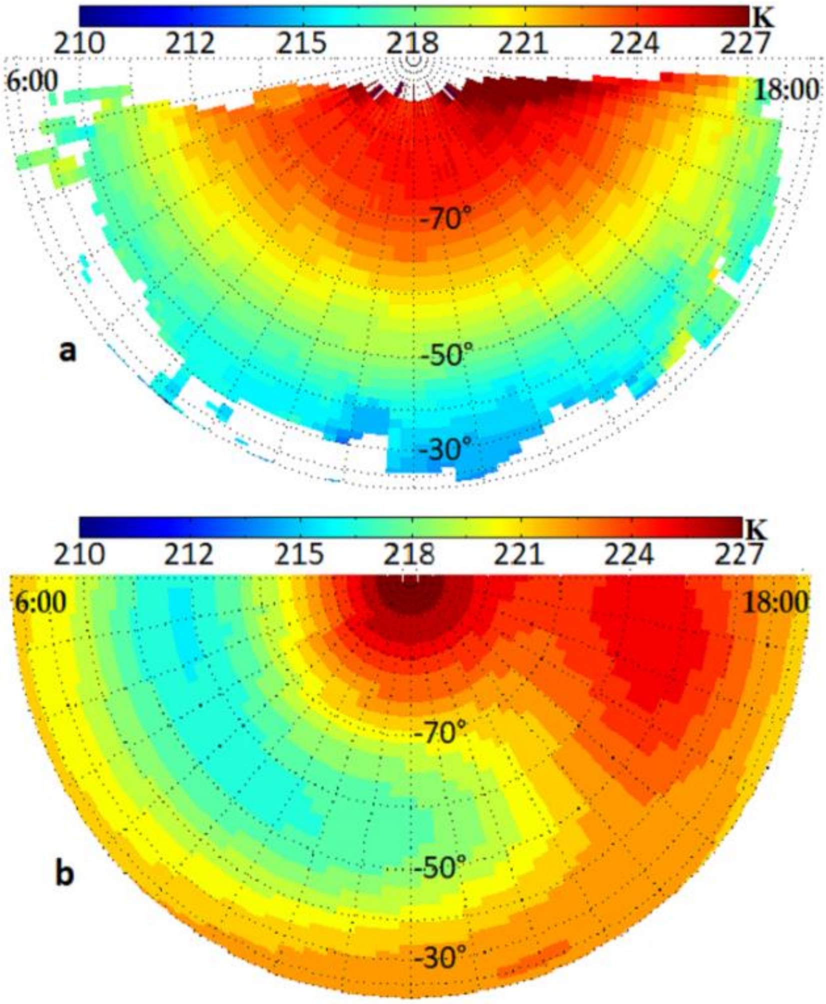

Figure 28: Nighttime polar temperature field (K) at 2×10^3 Pa (~72 km) for (a) VIRTIS-M and (b) the IPSL Venus GCM simulation. The radial coordinate of the grid corresponds to latitude (from 0° to -90°) and the angular coordinate to local time (from 18:00 to 6:00, clockwise). Scarica et al. (2019).

Indeed, even if this modelled upper inversion shares some characteristics with the cold collar, appearing just in the second half of the night and peaking around -60°, the altitude level where these features are obtained is different. These are completely different features, and the similarity of their horizontal structure is probably due to the longitudinal polar filter of the IPSL Venus GCM, that does not allow to reproduce fine-scale features. Indeed, the grid used currently in the model, is based on a longitude-latitude scheme with a longitudinal polar filter that reduces the latitudinal resolution and removes the high frequency variations in the polar regions. A new icosahedral dynamical core in development (Dubos et al., 2015) will be used in order to improve the robustness of the computation of the polar circulation.

Further discussions about the possible origins of this upper cold elongation, will be reported in **section 5.5**.

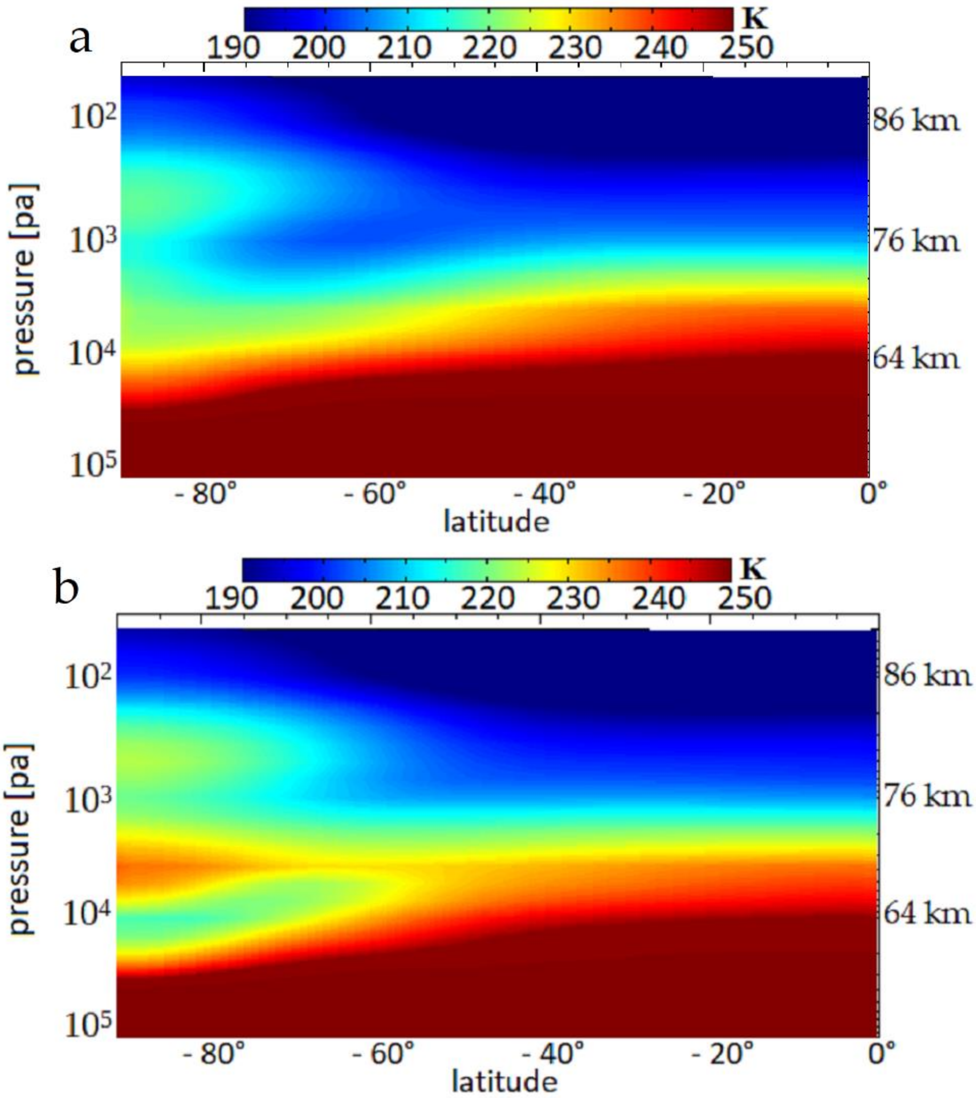

Figure 29: Zonally and temporally averaged temperature field (K) for the IPSL Venus GCM, when considering: (a) uniform clouds; (b) variable clouds. Data is averaged over 360° in longitude and for the entire nighttime, over 2 Vd. Adapted from Scarica et al. (2019).

4.1.4 Impact of the latitudinal variability of clouds on the thermal field

Garate-Lopez and Lebonnois (2018) show that introducing a latitudinal variability in the cloud parameterization is crucial in polar temperature structure and dynamics. Thanks to this improvement, the upper cold elongation appearing at mid-to-high latitude in Ando et al. (2016) and Lebonnois et al. (2016) weakens and the cold collar is reproduced for the first time in a Venus GCM, at the right altitude (2 x 10^4 Pa – 4 x 10^3

Pa) and latitude (poleward of 60°). Indeed, as reported in Garate-Lopez and Lebonnois (2018), the cold collar is formed in the simulation with variable clouds but not in the simulation with uniform clouds, which indicates that the generation of this characteristic feature is affected by latitudinal variations of the clouds in the IR cooling rates.

We show here the zonally and temporally averaged temperature field derived by both uniform and variable clouds simulation. In the uniform clouds' simulation (**Fig. 29a**), there is a wide, cold region – the upper cold elongation – around 10^3 Pa and -65° that extends downward and poleward, associated with a warmer region close to the pole. In the variable clouds' case (**Fig. 29b)**, this region becomes less extended and the cold collar appears.

This comparison demonstrates the importance of a fine cloud parametrization in the modelling of Venus.

4.1.5 Thermal field northern-southern hemisphere comparison

Along the entire study here presented, we assumed a symmetric planet and we presented our comparison just for the southern hemisphere, because of the better spatial coverage of the three datasets. In order to demonstrate the symmetry of the two modelled hemispheres, here we briefly show the comparison between the zonally and temporally averaged temperature field of the northern and southern hemisphere.

Fig. 30 shows that no macroscopic discrepancies are found. We can't appreciate any difference in either the overall hemispheric thermal structure or the polar temperature fields. Therefore, conclusions regarding the average modelled thermal field of the southern atmosphere of Venus, can be extended to the northern counterpart.

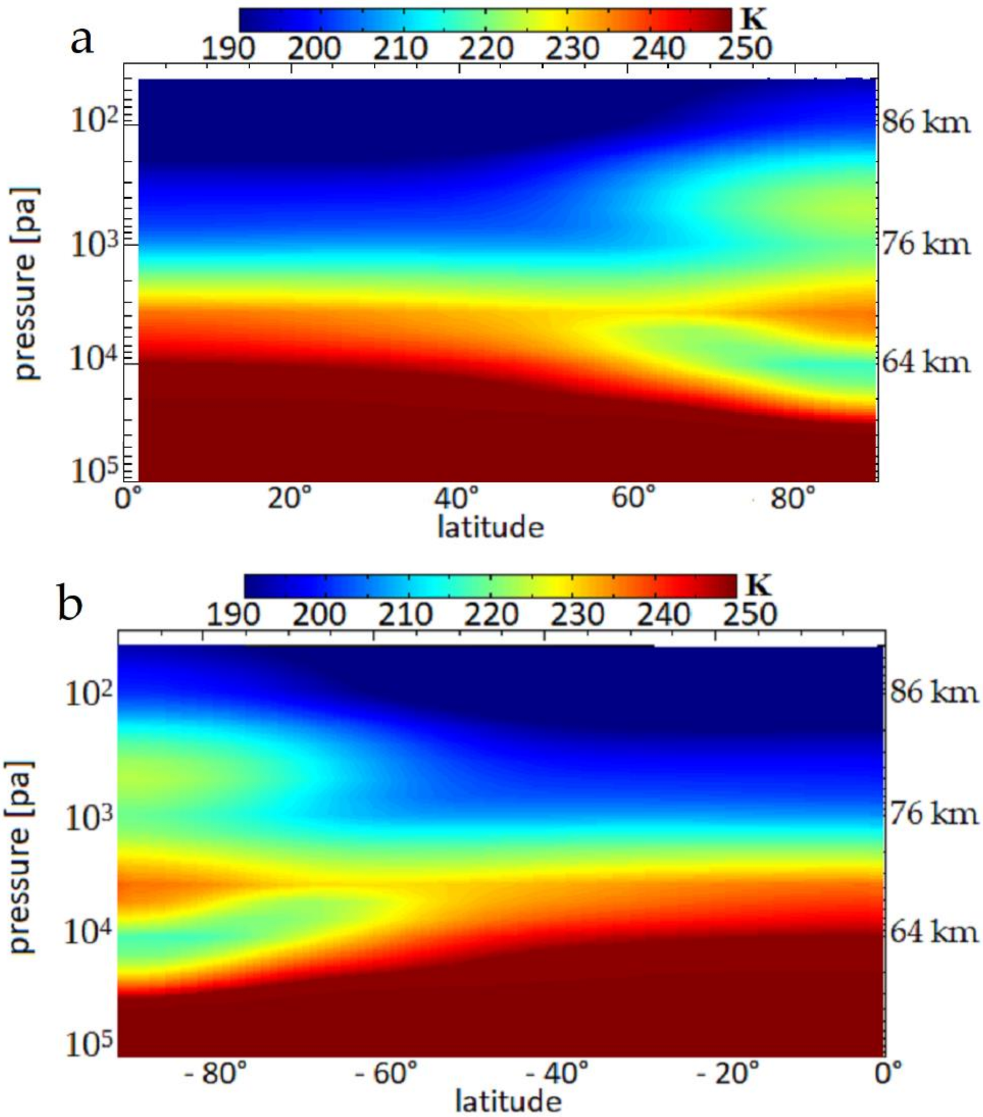

Figure 30: Altitude-latitude distribution of the zonal and temporal average temperature field (K) for the IPSL Venus GCM. The average has been obtained over 360° of longitude and the entire nighttime, over 2 Vd. (a) northern hemisphere (b) southern hemisphere. Adapted from Scarica et al. (2019).

4.2 Average wind fields

We now focus on the wind fields derived by the IPSL Venus GCM, which provides the second tool that we use to validate the model. Comparison with VIRTIS ad VeRa datasets will base upon published papers (Sanchez-Lavega et al., 2008).

First, we produced a map of the zonal and temporal average of the wind fields. The average was performed over 360° of longitude, using a simulation through 2 Venus days. The wind field have been decomposed in its three components: the zonal, the meridional and the vertical component. Maps have been produced for both daytime (averaging from 6:00 to 18:00 in local time) and nighttime (averaging from 18:00 to 6:00 in local time). Results are displayed in **Fig. 31.**

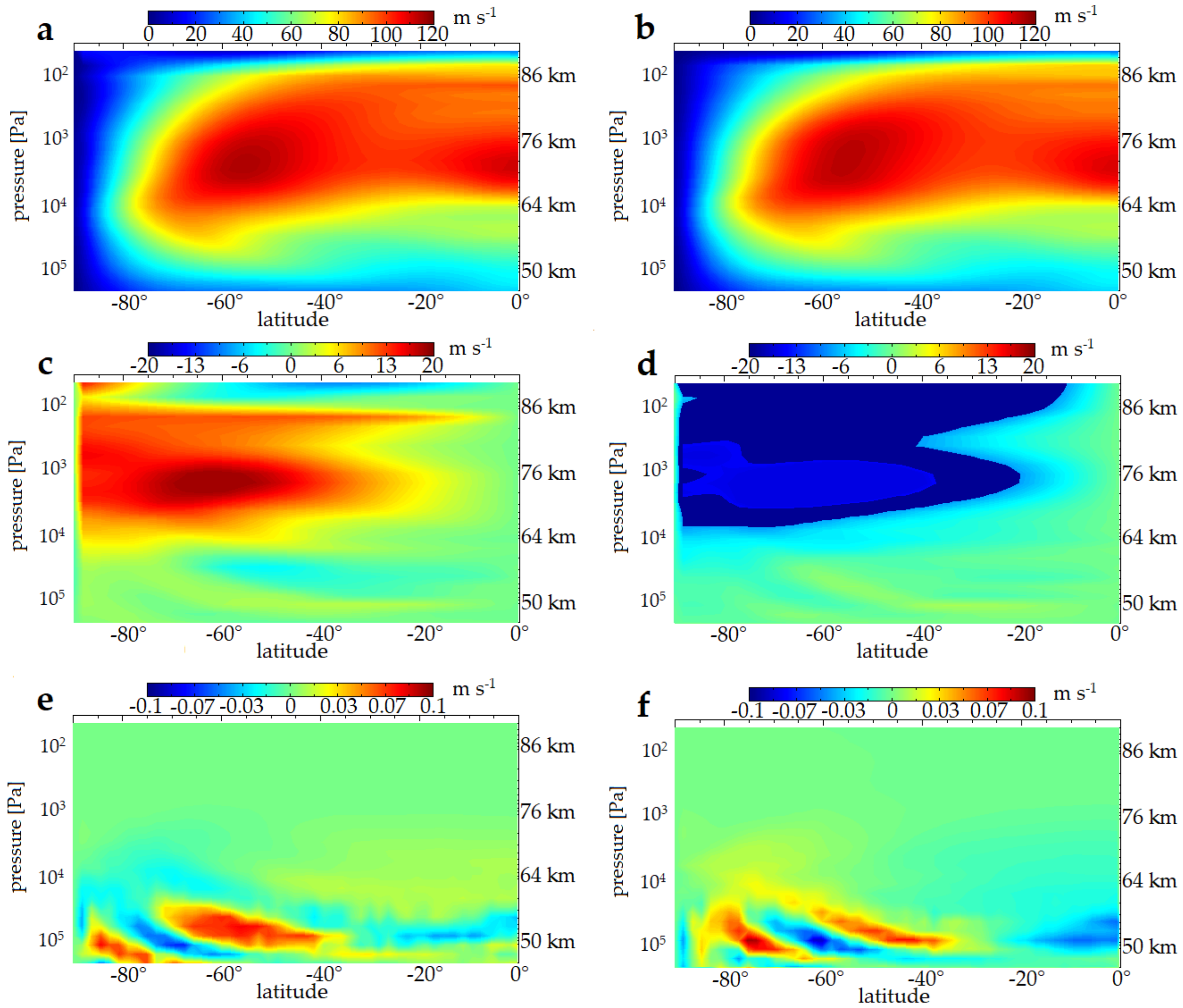

Figure 31: Zonally and temporally averaged wind fields (m/s) for the latest version of the IPSL Venus GCM, averaged over 360° in longitude and the southern hemisphere, for 2 Vd. (a) Zonal wind field, nighttime; (b) zonal wind field, daytime; (c) meridional wind field, nighttime; (d) meridional wind field, daytime; (e) vertical wind field, nighttime; (f) vertical wind field, daytime.

Fig. 31a and **Fig. 31b** refer to the zonal wind field in nighttime and daytime, respectively; **Fig. 31c** and **Fig. 31d** refer to the meridional wind field in nighttime and daytime, respectively; **Fig. 31e** and **Fig. 31f** refer to the vertical wind field in nighttime and daytime, respectively.

- The altitude-latitude distributions of the modelled wind field show that the zonal component is the dominant one in the range between ~50 km and ~86 km, with strong retrograde winds. Superrotation is already active at 50 km (winds at ~40 m/s) and fast winds are modelled in the entire range of pressures of our analysis, until very high latitudes (-80°): the fastest zonal winds speed is in general around ~100 m/s from ~65 km to ~85 km and two jets are centered at the equator and -60° latitude, with mid latitude wind velocities roughly 120 m/s. Both peaks are located at 3 x 10^3 Pa (~70 km). No macroscopic differences can be noted between daytime and nighttime.
- The meridional component, strongly dependent from the insolation, varies from day to night. During nighttime, a strong equatorward meridional circulation is found between 10^4 Pa and 10^2 Pa, at latitude higher than -30° (wind speeds roughly ~10 m/s). A -60° latitude jet is found, which peaks at ~20 m/s. Between 10^5 Pa and 10^4 Pa we observe an opposite trend: a meridional circulation with negative wind speeds around -5 m/s is observed, which is active in low-to-mid latitude and indicates a poleward meridional circulation. In general, we can recognize these features in the zonal wind field as Hadley-like cells in the lower and middle clouds (roughly 10^5 – 10^4 Pa), and above 10^4 Pa (up to the model top). A wide minimum region is modelled at 10^2 Pa: this high-altitude region is strongly dependent with thermal tides and will be analyzed more in detail in **chapter 5**. During daytime, the main component of the meridional circulation (between 10^4 and 10^2 Pa) is negative. Wind speeds reaches -15 m/s, indicating meridional winds pointing towards the south pole.
- The vertical component is almost negligible everywhere. Wind speeds are no more than 0.1 m/s in both directions, upward and downward. However, it is important to note the presence of regions where circulation cells recycle the air (below 2 x 10^4 Pa), linked to the mid latitude jet and the polar subsidence of cold air.

In Sanchez-Lavega, et al. (2008) they presented zonal and meridional winds at three altitude levels within the cloud layers of Venus: 47 km (nighttime), 61 km (daytime) and 66 km (daytime). Winds were derived from cloud tracking, using images taken with the VIRTIS instrument (**Fig. 32**).

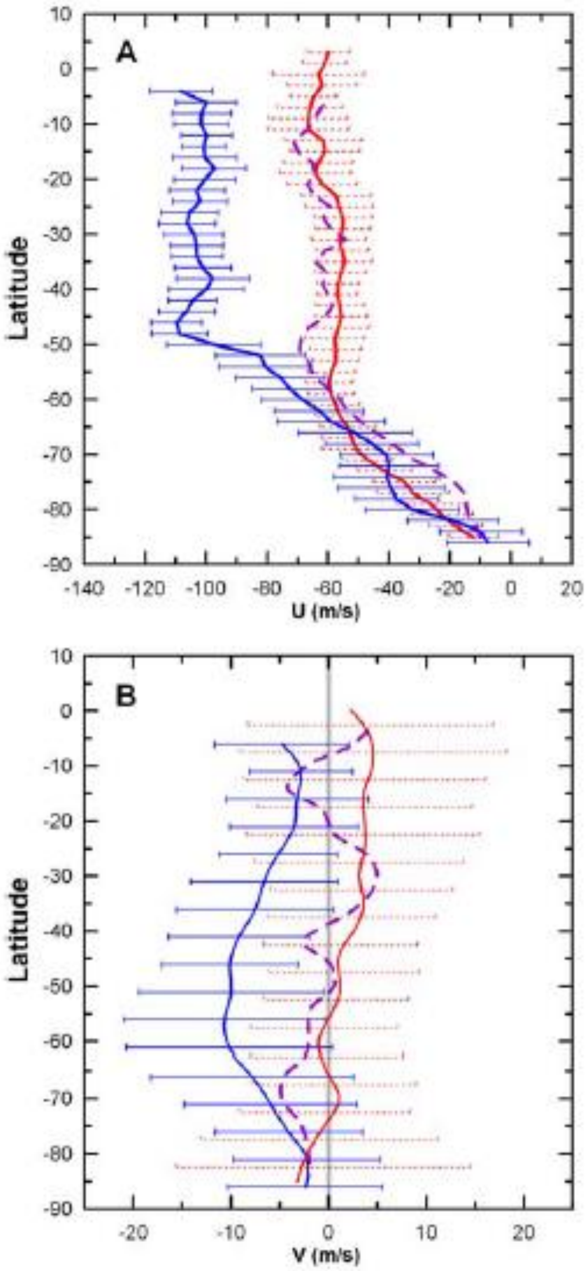

Figure 32: *Temporally and zonally averaged wind profiles from VIRTIS cloud tracking (m/s). Blue: daytime, 66 km. Violet: daytime, 61 km. Red: nighttime, 47 km. (a) Zonal wind velocity; (b) meridional wind velocity. Sanchez-Lavega et al. (2008).*

In the upper cloud level (61 and 66 km), the zonal wind speed is constant from the equator until -55° (60 m/s and 100 m/s, respectively) and then decreases towards zero at the pole. At 47 km the wind speed is constant until higher latitudes (~-65°) and then drops and reaches 0 m/s at the pole.

The meridional wind field presents a relatively large measurements uncertainty and no conclusive latitudinal trend can be inferred at 47 and 61 km. Meanwhile, at 66 km the meridional component reaches a peak of 10 m/s at -55° and then decreases until 0 m/s to the equator and the pole, marking the presence of a Hadley cell (Schubert et al., 1983; Gierarsch et al., 1997) and the structure of the polar vortex.

We extracted from the model the same altitude cuts and produced the comparison of the temporally and zonally averaged zonal and meridional wind field (**Fig. 33**) with these data. Before the comparison with Sanchez-Lavega (2008) it is worth mentioning that the error bars in data were obtained from the standard deviation of measurements, that includes both the measurement errors and the deviations from the mean due to dynamical processes.

At equatorial and mid-latitudes (0° to -60° latitude), a modelled vertical wind shear $\delta\langle u\rangle/ \delta z$ of 4 m/s per km is found between 61 and 66 km, where u is the zonal wind and z the vertical coordinate. At polar and subpolar latitudes (-60° to -90° latitude), a vertical wind shear $\delta\langle u\rangle/ \delta z$ slightly more than ~1 m/s per km is found between the same altitude levels.

Between 47 and 61 km, the simulated vertical wind shear $\delta\langle u\rangle/ \delta z$ is about 1.7 m/s per km at latitudes equatorward of – 40°, about 3 m/s per km at -70° and about 2 m/s per km poleward of -70°.

This means a modelled vertical wind shear at low latitude, between 47 and 61 km, larger than in VIRTIS data (< 1 m/s per km), and a smaller one between 61 and 66 km (8 m/s per km in data). At high latitude, the vertical wind shear is in general higher in the model than in data.

We must note that the altitudes of the winds obtained by cloud tracking in Sànchez-Lavega (2008) have been estimated by radiative transfer. Their errors will depend on several factors, such as the error of the method and the altitude of the clouds during day and night. Moreover, variations of $\delta\langle u\rangle/ \delta z$ along the vertical, produce uncertainties on the mean value.

- At 47 km the simulated zonal wind field has a behavior very consistent with data: it is constant until -65°, like in the observations, and then drops. The constant low and mid-latitude wind speeds are slower in the GCM than in data, about 15 m/s less (~40 m/s). This may be partially due to the uncertainty in the estimated altitudes of the winds. Between 0° and -20° a little bump in the profile can be noted – an equatorial jet – about 5 m/s higher than mid-latitudes; the error bars in the observations, does not allow us to draw any conclusions, even if a similar trend can be deduced in VIRTIS data. The meridional wind field – obtained for the nighttime, like in the observations – has generally positive values, with two peaks at -40° and -80°, that are not recognizable in data. Although showing peaks, the modelled meridional component displays very little values of the wind speed, that are consistent with the observed profile, within its error bars.

- At 61 km, the zonal wind field peak, drifts towards slightly lower latitudes, even if 10° poleward then the observed one. This jet, more evident than in data, reaches more than 80 m/s, that is 20 m/s higher than VIRTIS wind speeds and 15 m/s more than simulated low latitudes. Indeed, while in the observations this maximum is just a slightly variation in the almost-constant low to mid latitudes zonal wind field, in the GCM it is more evident. Poleward of -60° the zonal wind speed slows down in good agreement with data, even if the model presents a much higher latitudinal gradient. The modelled meridional component shows rising values from the equator to the pole, with a strong increase poleward of -75° (peak ~ -4 m/s). In Sanchez-Lavega, et al. (2008), meridional wind speeds display a peak at -70° (~ -5 m/s), but it does not confirm the faster simulated wind velocities close to the pole.
- At 66 km, the modelled zonal wind field is roughly 90 m/s in the low to mid latitude range and rises to 110 m/s at -60°. While having slower zonal wind speeds at low latitudes (10 m/s less than in cloud tracking), the -60° jet is consistent with observations. However, this simulated peak is much more marked than in data, having a higher contrast with respect to low latitudes – as happened at 61 km – and it is located poleward (-50° in the observations). Higher latitudes display the usual decreasing trend of the zonal wind speed, in both data and model, with the GCM presenting a higher latitudinal gradient. The rising wind speeds between -20° and 0° latitude are still present in the model, as in the lower altitude cases, but they don't appear in Sanchez-Lavega, et al. (2008). The modelled meridional component at this altitude level resembles the one at 61 km, with increasing values until -70°, where it reaches its maximum of -8 m/s. In data, while the maximum velocities are consistent with the simulation (~ -10 m/s), they are reached in a mid-latitude region

(between -40° and -60°). This behavior is shifted in the IPSL Venus GCM, which obtained a similar meridional wind profile around 70 km (not shown).

The 61 km level was also investigated using Galileo mission images (Peralta et al., 2007) and zonal wind speeds ~ 10 m/s higher than Sanchez-Lavega et al., (2008) were retrieved. These wind speeds are more consistent with the IPSL Venus GCM zonal component.

As already reported in Lebonnois et al. (2016), the comparison between the modelled zonal wind field and observations has improved with respect to previous versions of the IPSL Venus GCM, thanks to the new boundary layer adopted in this latest version, which yields more efficient pumping of angular momentum.

This improvement has a large impact, especially in the deep atmosphere, where superrotation is then activated, but also in the cloud deck level, with values more consistent with observations.

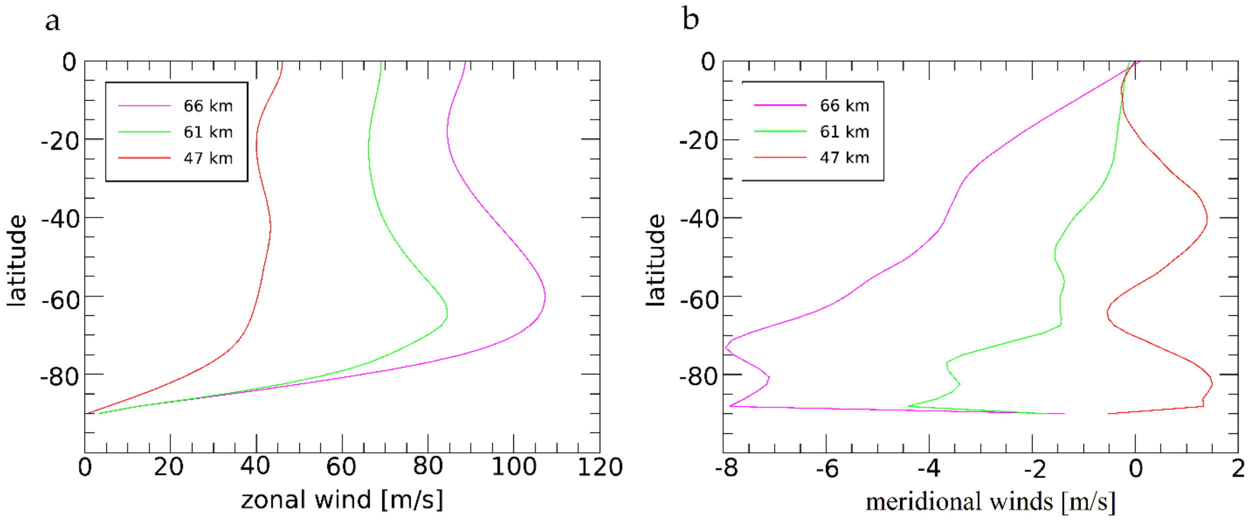

Figure 33: Temporally and zonally averaged wind profiles (m/s) from the IPSL Venus GCM. Violet: daytime, 66 km. Green: daytime, 61 km. Red: nighttime, 47 km. (a) Zonal wind velocity; (b) meridional wind velocity.

4.2.1 Impact of the latitudinal variability of clouds on the wind fields

The impact of the latitudinal variability of clouds is shown through a comparison of the modelled temporally and zonally averaged wind profiles uniform cloud case (**Fig. 34**) with the variable cloud case (F**ig. 33**).

In this latest version, considering the latitudinal structure of the clouds (Garate-Lopez and Lebonnois, 2018) has produced an even better agreement with data: in the uniform clouds' case, zonal winds were slower than the observed values, while the variable clouds' case adopted in this work, modelled wind velocities faster and in better agreement with observations. This is particularly clear in the 61 km and 66 km wind profiles in **Fig. 34a**.

This new version of the IPSL Venus GCM was also capable to decrease the intensity of the modelled equatorial jet, with respect to the mid-latitude jets and slightly reduced the height of the mid-latitude jets. However, the equatorial jet is still present (see the 66 km in **Fig. 34a**) and for sure stronger than cloud-tracking measurements. Moreover, the simulated mid-latitude jet is developed too close to the pole; for this reason, the latitudinal wind gradient at high latitude is still higher than observations.

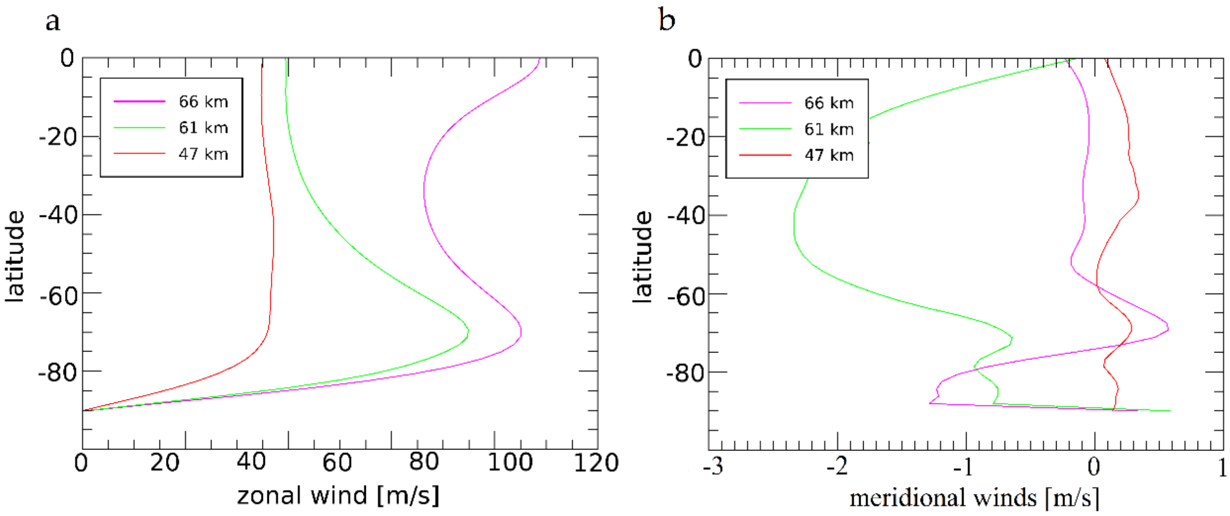

Figure 34: Temporally and zonally averaged wind profiles (m/s) from the IPSL Venus GCM uniform clouds' case. Violet: daytime, 66 km. Green: daytime, 61 km. Red: nighttime, 47 km. (a) Zonal wind velocity; (b) meridional wind velocity.

A worsening of the velocity of the zonal winds below 40 km altitude must be noted, even if not shown in these plots: this latest version of the IPSL Venus GCM has displayed winds slower than observed in the deep atmosphere (Schubert, 1983). This issue could be related to the horizontal resolution and the lack of large-scale gravity waves in the lower atmosphere. Indeed, as Lebonnois (2016) reported, improving the horizontal resolution with respect to Lebonnois et al. (2010), has also improved the winds below the clouds.

Meridional winds in this latest version (**Fig. 34b**) have been increased of a factor 3-4 with respect to the previous simulations, but the error bars in the observational meridional winds does not allow us to drive any conclusion.

4.2.2 Wind fields northern-southern hemisphere comparison

We already observed the symmetry of planet Venus hemispheres, through the evidence of the averaged thermal field comparison between northern and southern hemisphere. A similar study can be conducted, utilizing the zonally and temporally averaged zonal, meridional and vertical component of the wind field. The results presented in **Fig. 31** were obtained for the southern hemisphere; their counterparts are shown in **Fig. 35**.

No major differences can be assessed in the zonal and vertical component of the wind. The northern meridional wind field have the same absolute values of the southern wind field, but with a different sign. The broad minimum between 10^4 and 10^2 Pa, means meridional winds going from the north pole to the south, the opposite than in the southern hemisphere. Thus, the meridional circulation in this altitude range during nighttime is symmetric in the two hemispheres, pointing towards the equator in both cases. In the same altitude range, the circulation is reverted during daytime (directed towards the pole), though not shown.

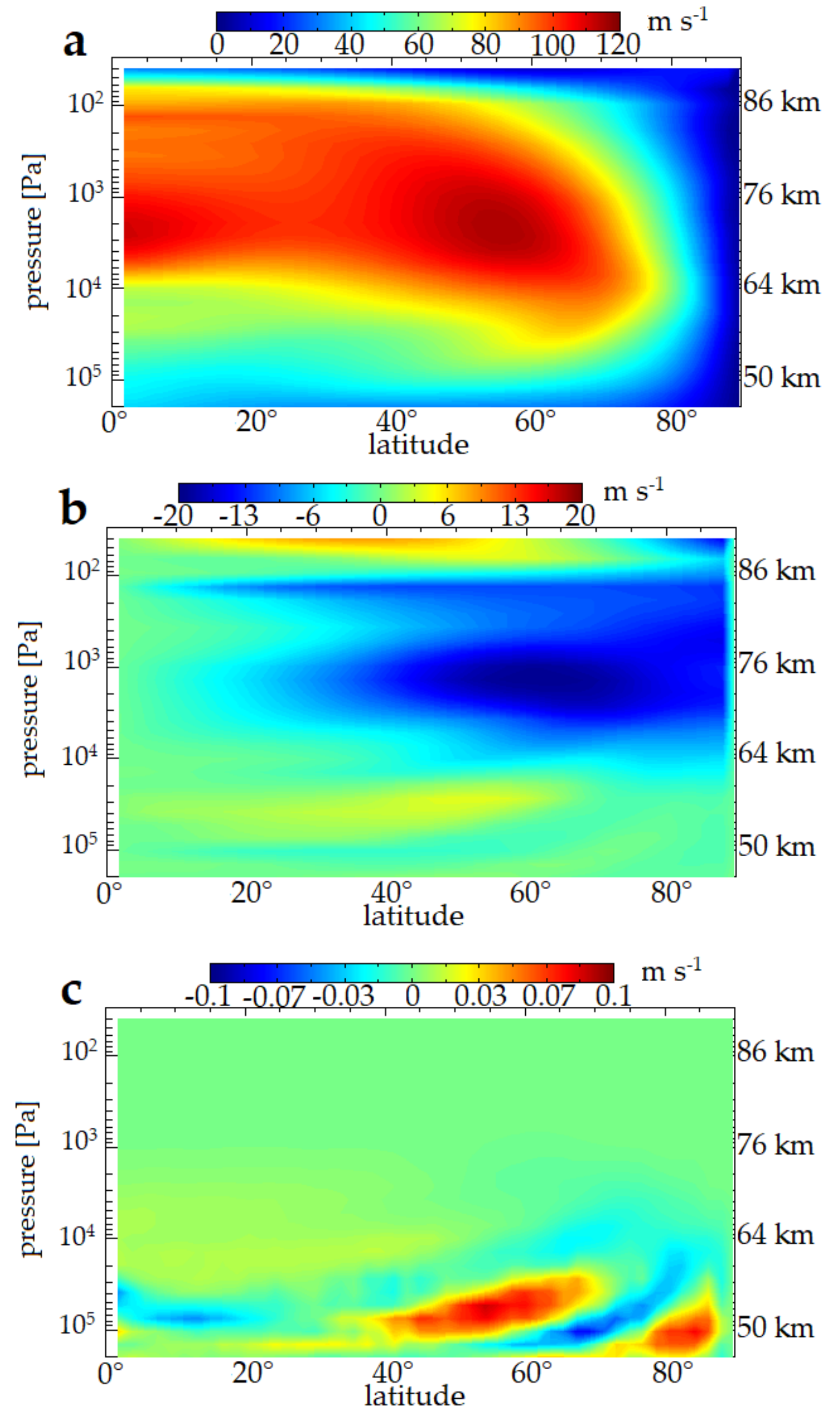

Figure 35: Zonally and temporally averaged wind fields (m/s) for the latest version of the IPSL Venus GCM, averaged over 360° in longitude and the northern hemisphere, over 2 Vd. (a) Zonal wind field, nighttime; (b) meridional wind field, nighttime; (c) vertical wind field, nighttime.

5. Data-model comparison: Thermal tides

5.1 Study of the wave activity

We used a Fast Fourier Transform (FFT), in order to study the waves developing in the modelled atmospheric circulation and to analyze the frequency spectrum of temperature, zonal and meridional winds.

The output of the modelled atmospheric winds has a frequency of 100 points per Venus day. For each given latitude, longitude and pressure in the GCM, the FFT is applied to this time series over the last 2 Vd of the simulation.

The amplitude of the FFT is displayed in **Fig. 36** (temperature field), **Fig. 37** (zonal wind field) and **Fig. 38** (meridional wind field), at several latitudinal cuts (-75°, -45° and -15° latitude) and pressure cuts (10^2, 10^3 and 10^4 Pa).

Our analysis reveals that the modelled temperature field, zonal wind field and meridional wind field, have in common a high contribution of low frequency waves (1/Vd, 2/Vd, 3/Vd). These waves are related to temperature oscillations resulting from the apparent motion of the Sun across the sky. They are radiatively controlled thermal phenomena in the atmosphere of Venus: since waves of different frequencies are involved, we speak of diurnal tides when referring to the 1/Vd frequency, semidiurnal tides for the 2/Vd frequency, terdiurnal tides for the 3/Vd frequency and so on.

In the temperature field (**Fig. 36**), these waves have a large impact from the equator to the poles, in the upper part of the mesosphere (10^2 Pa). In the deep part of the atmosphere (10^4 Pa), within the upper clouds, the diurnal tide is just important in the high latitude range, while the semidiurnal tide dominates at low latitudes. Typical amplitudes peak from 5 K at 10^2 Pa (low latitudes) and 10^4 Pa (high latitudes) to 2 K at 10^3 Pa.

In the zonal wind field (**Fig. 37**), the 1/Vd wave weakens at increasing pressures, although very narrow peaks are still observed at 10^4 Pa, poleward of -80°. Moving from 10^2 Pa to 10^4 Pa, also the peaks of the zonal wind 2/Vd and 3/Vd waves, reduced in their latitudinal extension: the 2/Vd is the most important between 10^2 and 10^3 Pa, from mid latitude until the equator. The 3/Vd component, that is marked in the upper atmosphere at mid latitude (between +/-20° and +/-70°), almost vanishes at higher pressures.

In the meridional wind field (**Fig. 38**), 1/Vd and 2/Vd are the dominant components among the low frequency waves. Going from 10^2 to 10^4 Pa, their amplitudes become progressively smaller. At all pressure levels, their peak is located around +/- 60°, while they generally fade close to the equator (equatorward of +/-10°).

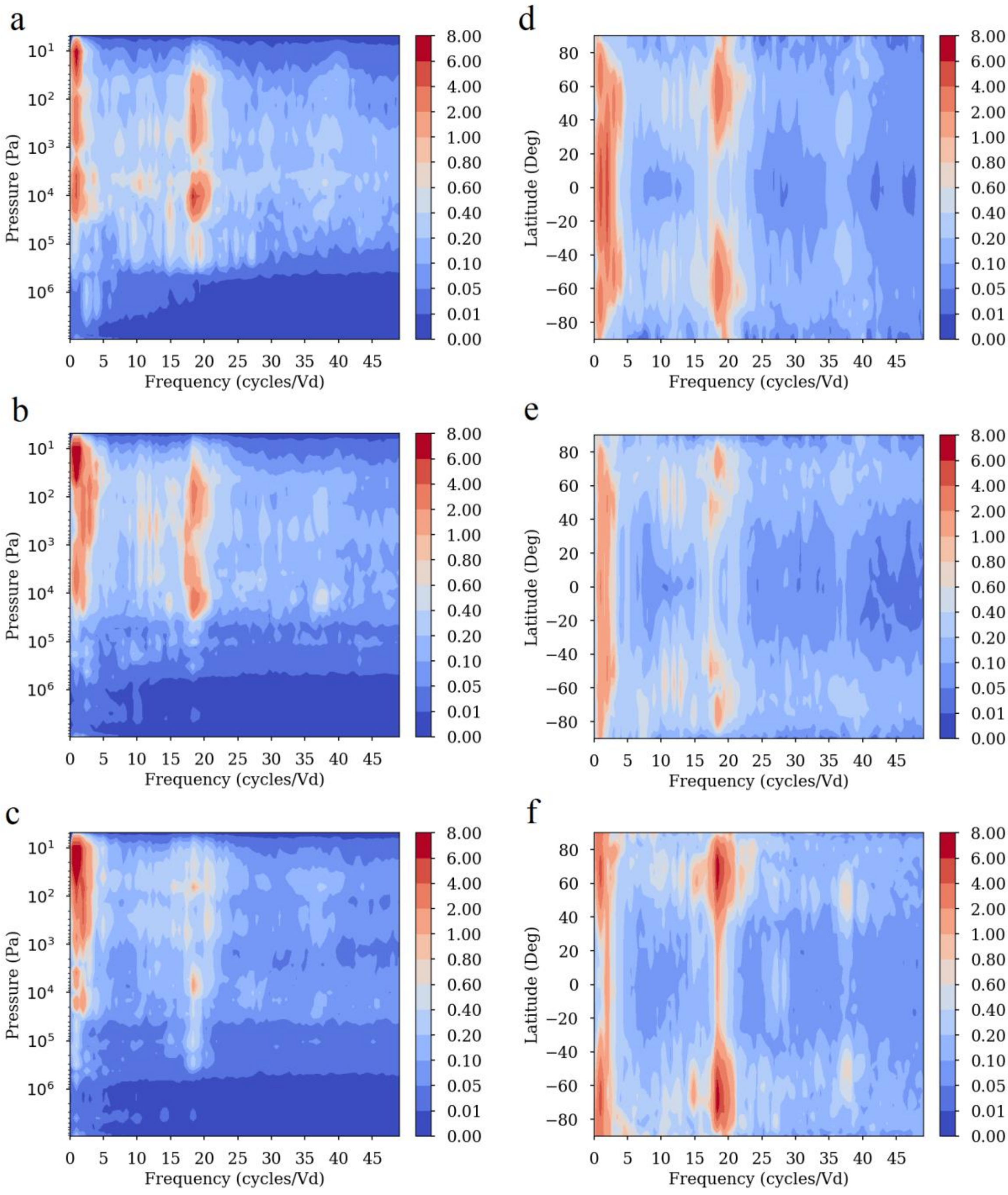

***Figure 36**: Frequency analysis of the temperature (K) as a function of pressure. (a) -75°; (b) -45°; (c) -15°; (d) 10^2 Pa; (e) 10^3 Pa; (f) 10^4 Pa.*

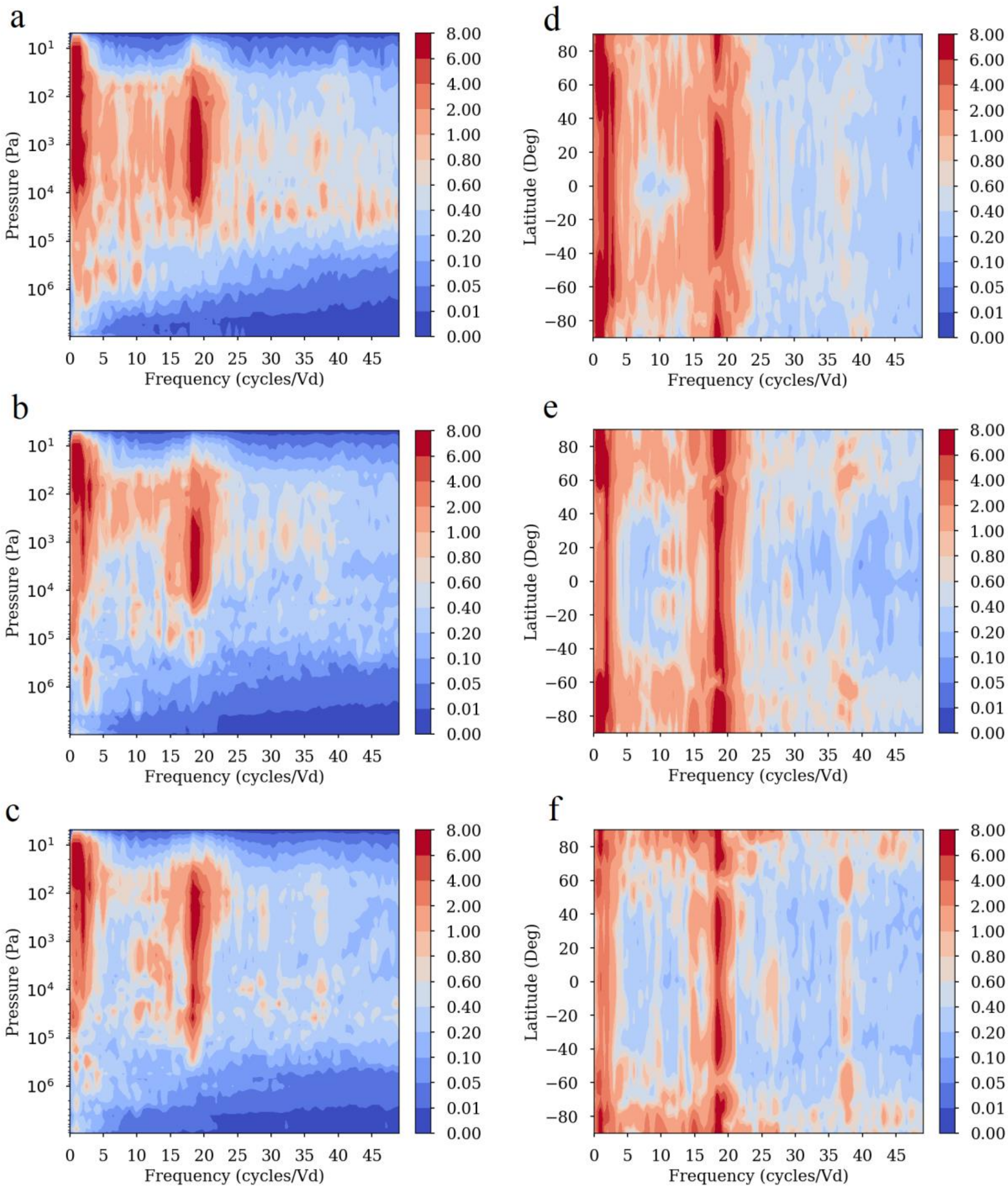

Figure 37*: Frequency analysis of the zonal wind field (m/s) as a function of pressure. (a) -75°; (b) -45°; (c) -15°; (d) 10^2 Pa; (e) 10^3 Pa; (f) 10^4 Pa.*

Waves propagating in the vertical component are negligible, according to our analysis, and are not shown here. We will briefly discuss the thermal tides in the vertical wind field at the end of this chapter.

The IPSL Venus GCM reveals a complex pattern of waves, beyond the main harmonics related to the thermal tides. At higher frequencies, other waves appear:

- The frequency analysis of the temperature field (**Fig. 36**) reveals small and weak waves with a frequency of 11/Vd, 12/Vd and 13/Vd, that are located between 40° and 70° in the mid pressure range (10^3 Pa) and around -75° latitude at pressures slightly lower than 10^4 Pa. Another 15/Vd wave appears at high latitude and high pressures (from -55° to -75°, around 10^4 Pa). But the most prominent wave pattern is the one at 18/Vd, 19/Vd and 20/Vd: the amplitude of these waves reaches 6 m/s at -75° and 10^4 Pa, where it peaks. These waves compose in general a mid to high latitude pattern, that covers from 2 x 10^4 to pressures lower than 10^2 Pa, except for the narrow region between 10^3 Pa and 2 x 10^3 Pa.

- The high-frequency waves that arise in the analysis of the zonal wind (**Fig. 37**), compose a more complex pattern. Between the 4/Vd and the 18/Vd frequency we see many waves, mostly located at high latitude (poleward of +/-75°), while in the low-to-mid-latitude range, they appear closer to the lower pressures (10^2 Pa). Other perturbations are also present at higher frequencies, especially between 10^3 and 10^4 Pa. The dominant wave in this frequency analysis is the one at 18/Vd, whose amplitudes are comparable with 1/Vd and 2/Vd. The 18/Vd wave extends from the equator to mid latitude (+/-50°) and from mid latitude (+/- 60°) to the poles, with just a little gap between +/-50° and +/-60°, at both hemispheres. While the waves between 4/Vd and 18/Vd may be higher orders harmonics of the thermal tides, this 18/Vd wave may be responsible for the high frequency perturbations.

- The analysis of the meridional wind field (**Fig. 38**) presents some resemblance with the temperature field and the zonal wind field. As for the temperature field, equatorial to mid-latitude waves (from 0° to +/-60°) develop at frequencies of 11/Vd, 12/Vd and 13/Vd, in the high atmosphere (between 10^2 Pa and 3 x 10^3 Pa). As for the zonal wind, between the 4/Vd and the 18/Vd frequency, we report many waves, peaking at high latitude (poleward of +/-75°) and lower pressures (10^2 Pa); other perturbations are present at frequencies higher than 20/Vd, especially around cloud top (pressures slightly higher than 10^4 Pa). As already discussed for the zonal wind field, these two groups of waves may be subharmonics of the low-frequency components of the thermal tides and of the major 18/Vd wave, respectively. Indeed, at 18/Vd, a high-amplitude wave is found also in the meridional wind field, from +/-20° to the poles, with a little gap around the equator, which resembles the 1/Vd and 2/Vd components of the meridional wind.

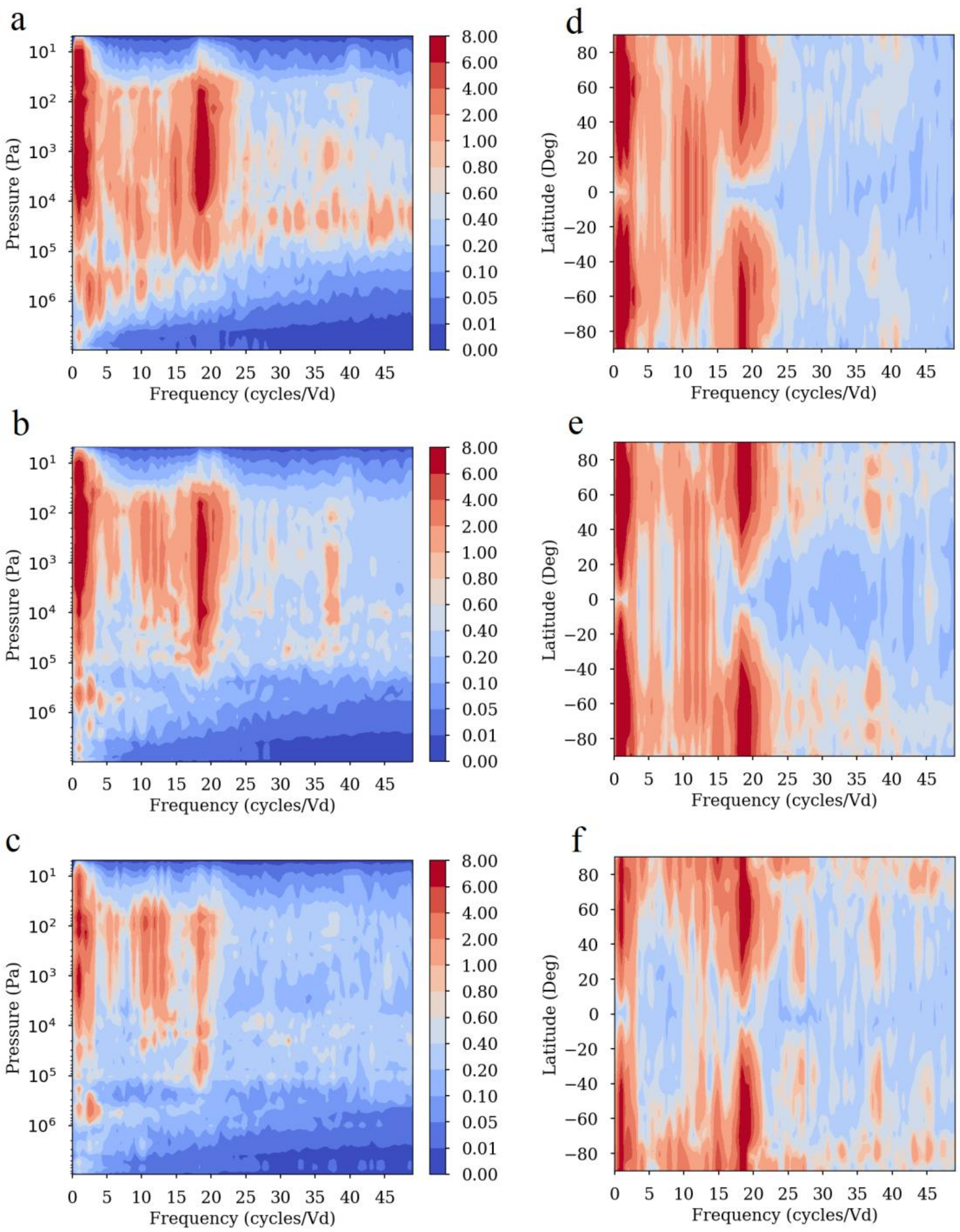

***Figure 38**: Frequency analysis of the meridional wind field (m/s) as a function of pressure. (a) -75°; (b) -45°; (c) -15°; (d) 10^2 Pa; (e) 10^3 Pa; (f) 10^4 Pa.*

The 18/Vd perturbation is visible in the zonal wind and in the meridional wind. While in the zonal wind it extends from the equator up to +/- 50° and then from mid latitude (+/- 60°) to the poles, in the meridional wind this wave is seen at low latitudes, but not on the Equator. These are characteristics of a Kelvin type wave, which is a hydrodynamic instability that develops in presence of strong vertical shear of the horizontal wind: as the shear between the layers increases, it can become unstable and waves will form across the interface.

The 11/Vd, 12/Vd and 13/Vd, on the opposite, are equatorial to mid-latitude waves in the meridional wind field and then appears at low latitude – but not at the equator – in the zonal wind and temperature fields. These are characteristics of Rossby-gravity waves propagating slower than the Kelvin wave.

In the following sections, we will focus more on the thermal tides, the low-frequency waves of these analysis, and we put them in the context of a comparison with observational data and other Venus GCMs.

5.2 Temperature anomalies

The IPSL Venus GCM and Venus Express data, are now compared by using the thermal tides induced in the atmosphere by the diurnal cycle of the solar heating rates.

Altitude-local time distributions of temperature anomalies (defined as the temperature differences minus the average over the entire nighttime) are shown in **Fig. 39** and **Fig. 40** for the GCM simulation and for VIRTIS observations.

For the high-latitude and mid-latitude samples a robust comparison can be made, which is not the case for the low latitude one, where VIRTIS data coverage is not enough to produce meaningful maps. The same is true for VIRTIS-H at high latitude. Therefore, we show the comparison of the IPSL Venus GCM with VIRTIS-M at -75° latitude and with both VIRTIS-M and VIRTIS-H at -45°. The right edges of these maps correspond to the dawn terminator, while the left ones to the evening terminator. Local time goes from 18:00 (left) to 6:00 (right). Data close to the dawn terminator have been removed in our analysis, because of the presence of spurious effects due to the scattered sunlight coming from daytime.

Fig. 39a shows the modelled temperature anomalies' map at -75° latitude. At altitudes below 10^3 Pa (~ 76 km), a warmer first half of the night is displayed until 22:00 (~5 K), and a colder second half after 0:00 (~ -5 K). An inverted tendency is seen above 10^3 Pa, with colder temperature towards evening (~ -4 K) and warmer towards dawn (~4 K). This warm–cold dichotomy that emerges in this high latitude temperature anomalies' map, points out the presence of a periodic temperature wave, linked with the diurnal cycle. These periodic fluctuations seem to be related to diurnal tide. The presence in the model of a diurnal differential heating of the atmosphere, induced by the sun, is an evidence of the GCM capability to reproduce thermal tides.

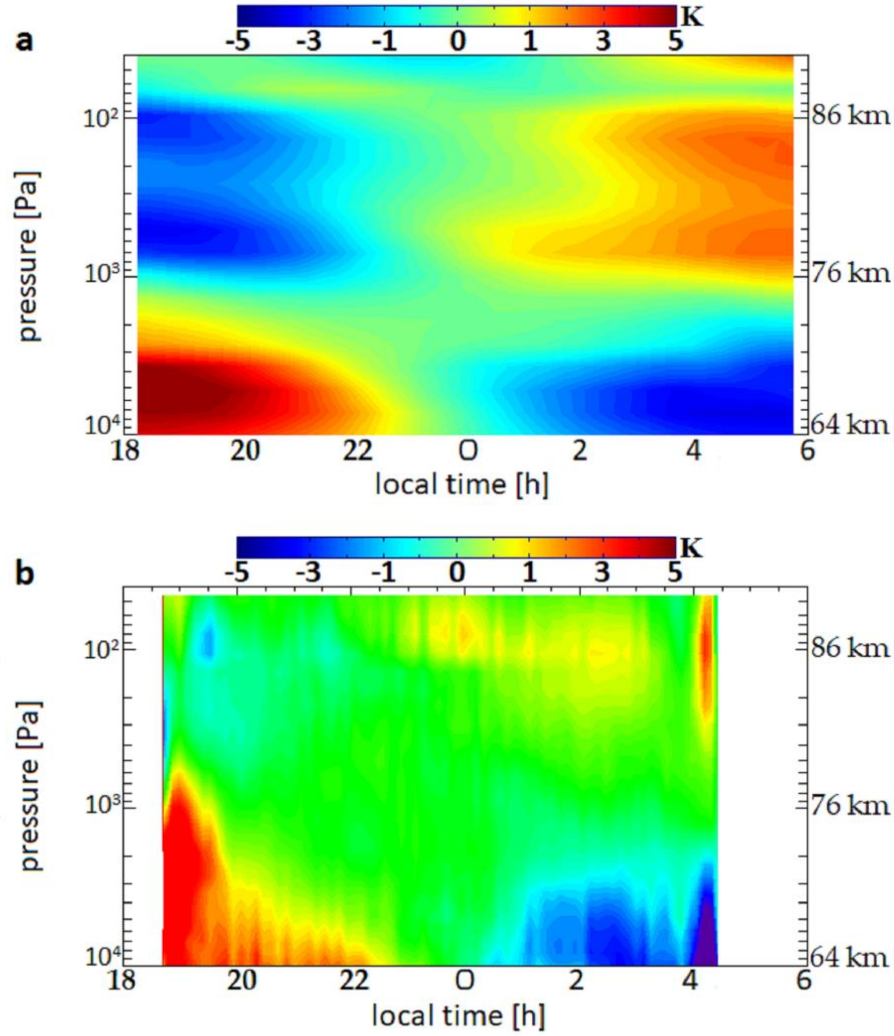

***Figure 39**: Altitude-local time distribution of the temperature residuals anomalies (K) at -75°. (a) GCM simulation; (b) VIRTIS-M observations. Scarica et al. (2019).*

Moreover, comparing with **Fig. 39b**, we note that the observations share with the model the two clearly recognizable regimes. The agreement is very good in the atmosphere below 10^3 Pa, where the observed minimum and maximum have a comparable amplitude with the same modelled features. At pressures lower than 10^3 Pa, cold and warm regions are less pronounced in VIRTIS-M with respect to the model (roughly -1 K and 1 K, respectively). These maxima and minima extend in a broad altitude region from 10^2 Pa (~ 86 km) to 10^3 Pa (~ 76 km) in the model; in VIRTIS-M data they just appear in a narrow region around 10^2 Pa.

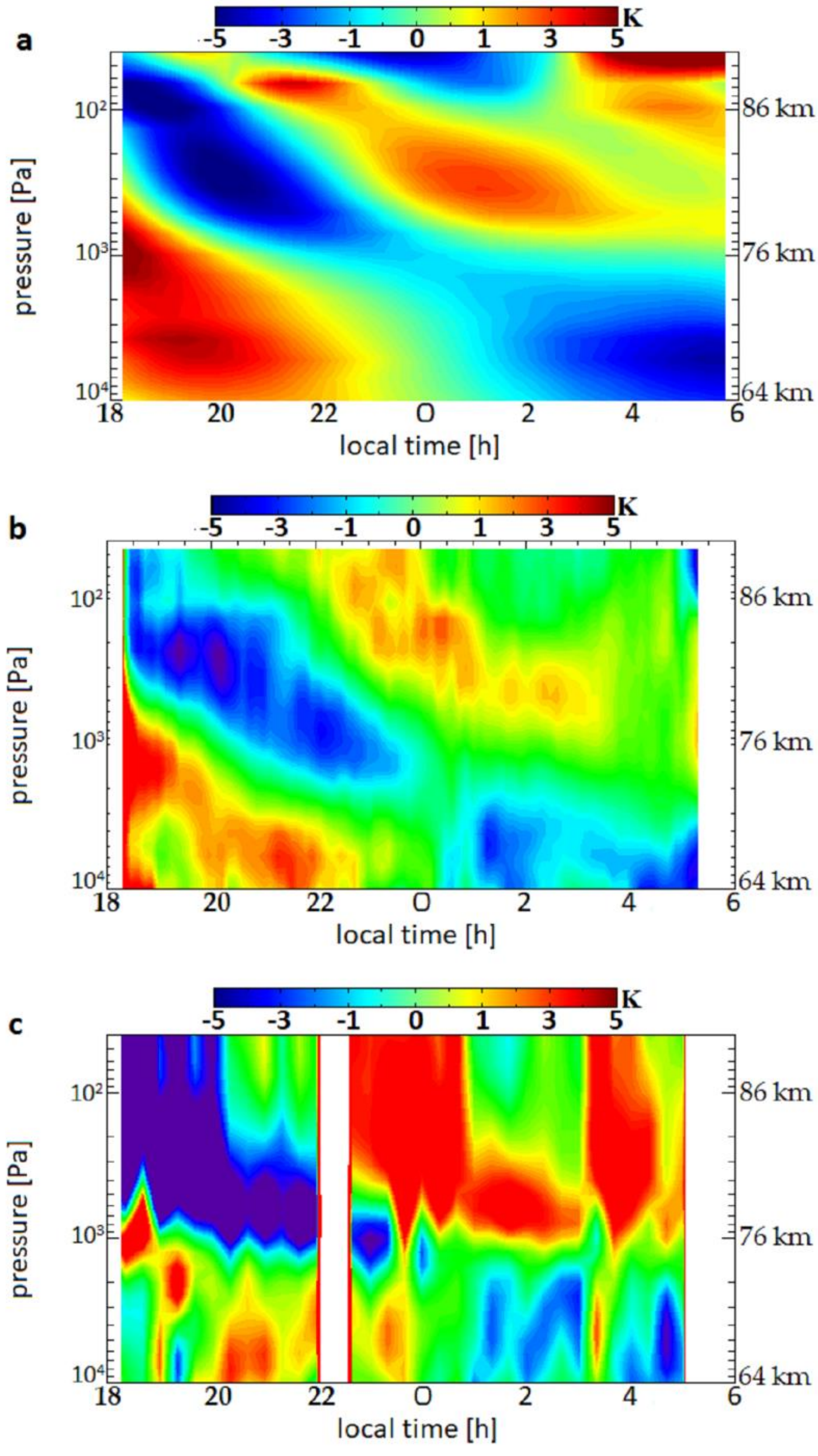

Figure 40*: Altitude-local time distribution of the temperature residuals anomalies (K) at -45°. (a) GCM simulations; (b) VIRTIS-M observations; (c): VIRTIS-H observations. Scarica et al. (2019).*

At -45° (**Fig. 40a**) the modelled maximum-minimum couple above 10^3 Pa splits up into a component with half of the period, which phase propagates into the higher layers as we move towards the evening terminator. At low pressure levels, the semidiurnal tide is clearly dominating in the model, while the diurnal tide is still recognizable in the atmosphere below 10^3 Pa. The bottom simulated minimum and maximum have temperature anomalies around -5 K and 5 K. The upper minima and maxima have a slightly weaker amplitude (minima around -5 K and maxima around 3 K). On the very top, at pressures lower than 60 Pa, we find another region dominated by diurnal tides. It must be noted that this altitude range is the upper limit of VIRTIS-M retrieval and the SPICAV bottom limit. At the same time, VeRa does not provide enough coverage. Therefore, we don't have information to draw any conclusion.

The modelled temperature anomalies are qualitatively in good agreement with the observed ones. The appearance of a dominating semidiurnal component at mid latitudes is confirmed by both VIRTIS-M (**Fig. 40b**) and VIRTIS-H (**Fig. 40c**) data, with a striking resemblance with the GCM: model and data show a good consistency of their phase in local time. The contrast between warm and cold regions in the observations is reduced with respect to the model, apart from VIRTIS-H anomalies at pressures below 10^3 Pa, which present an amplitude larger than 10 K.

In **Fig. 41**, the -15° latitude case is shown for the IPSL Venus GCM, although no reliable comparison can be made with VIRTIS and VeRa data. The diurnal component at pressures higher than 10^3 Pa (below 76 km), fades, while the semidiurnal component in the upper part of the simulated atmosphere (above 76 km), shows an amplitude weaker than mid-latitude. Towards the equator, the maxima and minima related to thermal tides, strengthen, although still having an amplitude smaller than the one at -45°. The phase of these minima and maxima is shifted towards dawn, with respect to the mid-latitude sample (about 2 h of phase shift between -15° and -45°).

Fig. 39, **Fig. 40** and **Fig. 41** show the total temperature deviations but do not directly show the thermal tides' first and second components. However, it seems that many of the temperature anomalies that we find in model and data come from diurnal and semidiurnal tides, and that higher harmonics of thermal tides are much less significant when contributing to the total temperature deviations. In the next section we will discuss thermal tides and their impact in the modelled temperature and wind fields.

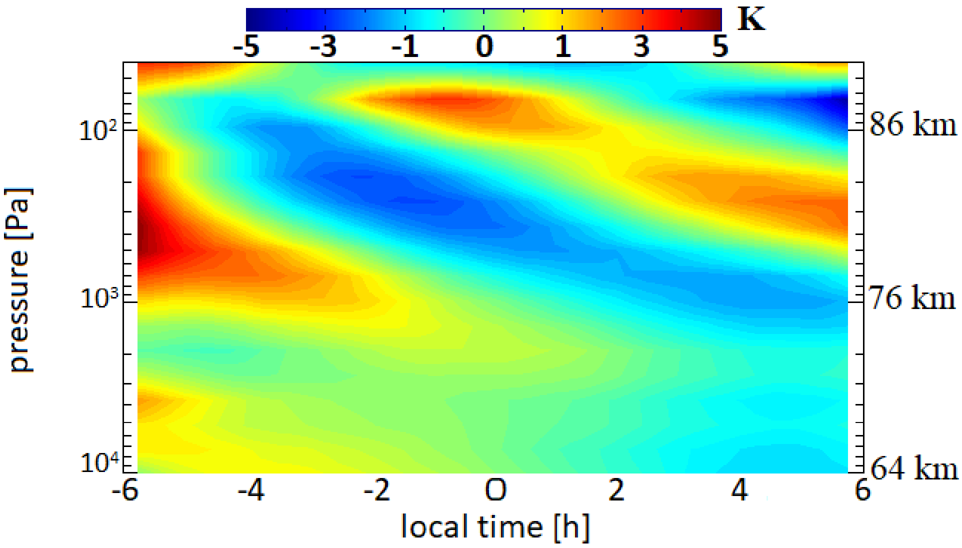

Figure 41: *Altitude-local time distribution of the temperature residuals anomalies (K) at -15°, for the IPSL Venus GCM.*

5.3 Thermal tides in the temperature and wind fields

Through the Fourier analysis we expressed the temperature and the wind fields in a sum of periodic components. We used a Fast Fourier Transform (FFT) algorithm in order to separate each field into components that contribute at discrete frequencies. This FFT applies in the time domain and its output (spectrum or transform) exists in the frequency domain.

Defining our field as a Fourier series:

$$A_k = \sum_{m=0}^{n-1} a_m e^{\left(-2\pi i \frac{mk}{n}\right)}$$

k = 0, …, n-1,

or, in a sine-cosine form:

$$A_n = \frac{a_0}{2} + \sum_{m=1}^{N} a_m \cos\left(2\pi \frac{mk}{n}\right) + b_m \sin\left(2\pi \frac{mk}{n}\right)$$

where a_m and b_m are the coefficients of the Fourier series, m is the order of the series and k/n gives the time interval, we can then extract each different order of the series. Knowing the Fourier coefficients means to know the expression of each sub-harmonic. The order 0 will be the average for that field, the 1st order will correspond to the 1st harmonic (1/Vd frequency), the 2nd order to the 2nd harmonic (2/Vd frequency) and so on.

Latitude-pressure maps of the FFT spectrum of the temperature, for the frequencies 1/Vd, 2/Vd, 3/Vd and 4/Vd are plotted in **Fig. 42** for the southern hemisphere and the range of pressure 30 – 10^4 Pa. They give information about the amplitude of the main subharmonics of the thermal tides and they illustrate the regions where they are impacting more.

The diurnal tide clearly dominates at pressures lower than 7 x 10^2 Pa, where its amplitude is far bigger than the other three sub-harmonics. Between 10^3 and 10^2 Pa, at latitudes ranging from -55° to -80°, another peak of this component is shown, with values roughly 3.5 K. At latitudes slightly equatorward (-45° to -80°), a lower altitude peak is shown in the diurnal tide amplitude map, with peak values around 5.5 K.

In the entire low-to-mid-latitudes (until -50°), between 70 Pa and 10^3 Pa, the semidiurnal tide is comparable or – in some regions – dominates over the diurnal component. Its peak is about 5.5 K closer to the equator. Outside of this region semidiurnal tide is negligible.

The terdiurnal and quarterdiurnal tides reach their maximum at latitudes between -40° and -60°, and pressures below 5 x 10^2 Pa. The 4/Vd component is overall negligible with respect to the first two sub-harmonics and its peak is about 1 K. Meanwhile, the terdiurnal component can still have a decent impact in the mid latitude thermal field, between 50 and 5 x 10^2 Pa, but especially in the 2.5 K peak, at pressures between 2 x 10^2 and 5 x 10^2 Pa, where the 1/Vd component almost fades.

According to Lebonnois et al. (2016), these behaviors are consistent with VIRTIS/Venus-Express dataset analysis. However, we can directly evaluate the agreement of model and data through **Fig. 39** and **Fig. 40**: we already know that these figures are not meant to directly show the thermal tides' main sub-harmonics but, as already guessed at the end of **section 5.2**, many of the temperature anomalies – observed and modelled – come from the main components of the thermal tides and in particular the diurnal and the semidiurnal tides: thermal tides amplitudes and temperature anomalies varies latitudinally and altitudinally with a good consistency.

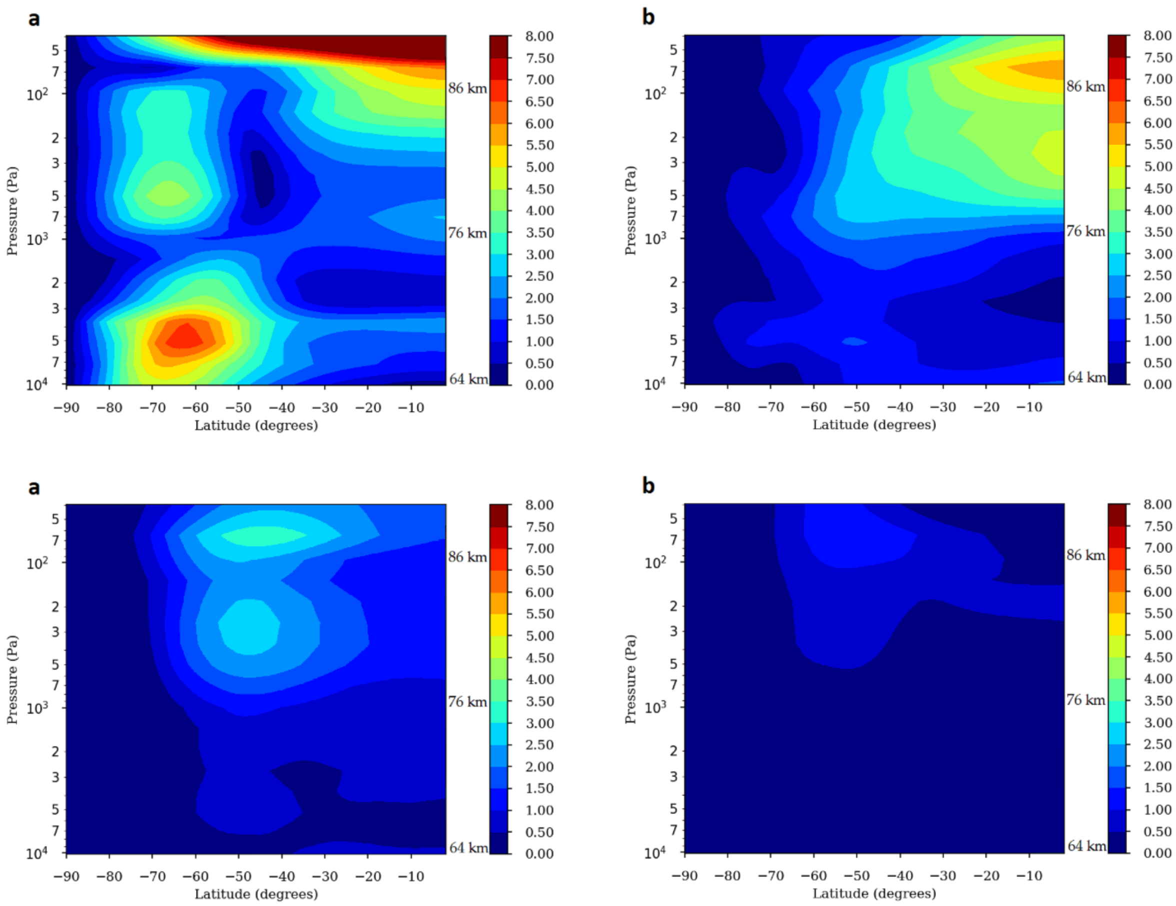

***Figure 42**: Fast Fourier transform (FFT) components of the temperature in the GCM simulation: (a) diurnal component; (b) semidiurnal component; (c) terdiurnal component; (d) quarterdiurnal component. Adapted from Scarica et al. (2019).*

The clear warm-cold dichotomy observed along the nighttime in VIRTIS-M data high-latitudes (**Fig. 39**), agrees with **Fig. 42**, where a -75° latitude section, would cut along the two peaks of the diurnal tide, while all the other main harmonics would be negligible.

The two different regimes observed at -45°, above and below the 10^3 Pa pressure level (semidiurnal and diurnal tides dominating, respectively), are found in **Fig. 42**, too. Cutting along -45°, the 2/Vd is found as the dominating component above 10^3 Pa, partially overlapped in a small region to the 3/Vd sub-harmonic. Vice versa, below 10^3 Pa, 1/Vd is larger than the other components. The presence of the 3/Vd sub-harmonic is not easy to distinguish in either the IPSL Venus GCM or the VIRTIS temperature anomalies. On the other hand, right on the top of the analyzed pressure range (from ~30

Pa to ~60 Pa), we confirm the presence of a diurnal-tide-dominated region, which is not appearing in data. The dominance of diurnal tide on the top of Venus atmosphere is known, but this comparison suggests a little altitude displacement between model and data.

Latitude-pressure maps of the FFT spectrum of the zonal wind, for the frequencies 1/Vd and 2/Vd are plotted in **Fig. 43** for the southern hemisphere and the range of pressure 30 – 10^4 Pa. The 3/Vd and 4/Vd sub-harmonics are negligible and thus have been omitted.

Low-to-mid-latitudes, below ~ 86 km altitude, are characterized by a weak diurnal tide component. However, on the top of the modelled atmosphere and at high latitude, the amplitude of the diurnal tide affecting the zonal wind increases above 20 m/s.

The semidiurnal tide is not negligible, but for sure is weaker than the diurnal tide in the entire range of pressures and latitudes. The low latitude peak around 10^2 Pa, is the same affecting the temperature field, but it just reaches 10 m/s and doesn't dominate on the diurnal component. Another peak, with a similar amplitude, but less extended, is found between -60° and -70°, around 10^3 Pa.

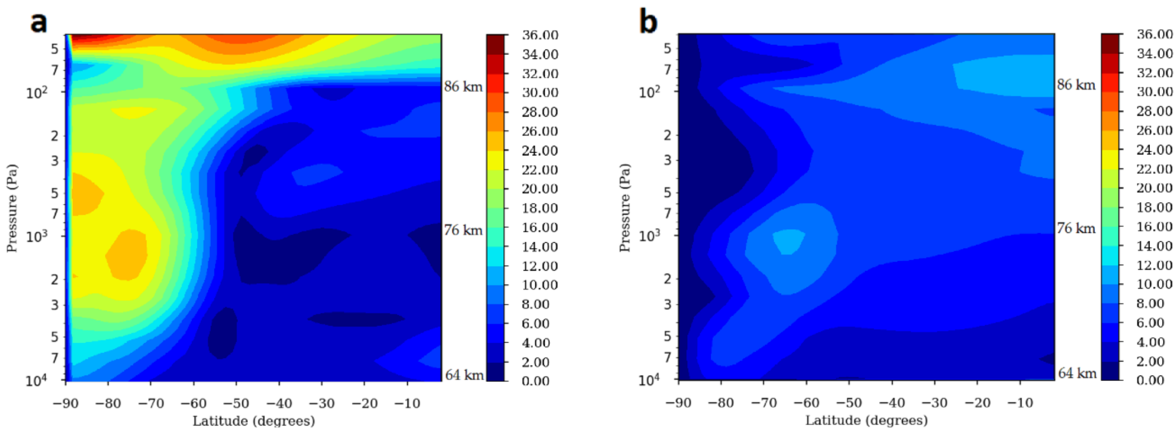

Figure 43: *Fast Fourier transform (FFT) components of the zonal wind in the GCM simulation: (a) diurnal component; (b) semidiurnal component.*

Terdiurnal and quarterdiurnal sub-harmonics are not impacting the simulated thermal tides in the zonal wind. They are negligible and thus, they are not presented here. A full analysis of the zonal tidal disturbances has been carried out in Peralta et al. (2012), but conclusive results are just presented in a very narrow region of latitudes (from -72° to -73°) at cloud top (~ 68 km), where it is shown the presence of a quarterdiurnal harmonic in the zonal wind structure, with a tidal amplitude of 5.0 m/s, that is ~20% of the zonally averaged zonal flow.

The FFT spectrum of the meridional wind (**Fig. 44**) shows that the diurnal component resembles the zonal and temporal average of the meridional wind fields. Indeed, both the phase and the amplitude are consistent with **Fig. 31c** and **Fig. 31d**, which means that the meridional circulation is fully activated by the temperature oscillations due to the variation of solar heating.

The 2/Vd component is consistent with the 1/Vd, but its amplitude reaches at most 10 m/s, 30% less than diurnal tide's amplitude, which is > 30 m/s at peaks and > 20 m/s in a broad region equatorward of -40°.

The tidal effects on the meridional component of the winds observed in VIRTIS-M, are much stronger than the tidal effects on the zonal component (Peralta et al., 2012). The 1/Vd wave is clearly detected in data and dominates this component of the wind. The peaks are located around -79°, with an amplitude slightly lower than model. In the southern hemisphere, the observational diurnal tides accelerate the atmosphere poleward in the dayside and equatorward in the nightside: this agrees with the IPSL Venus GCM.

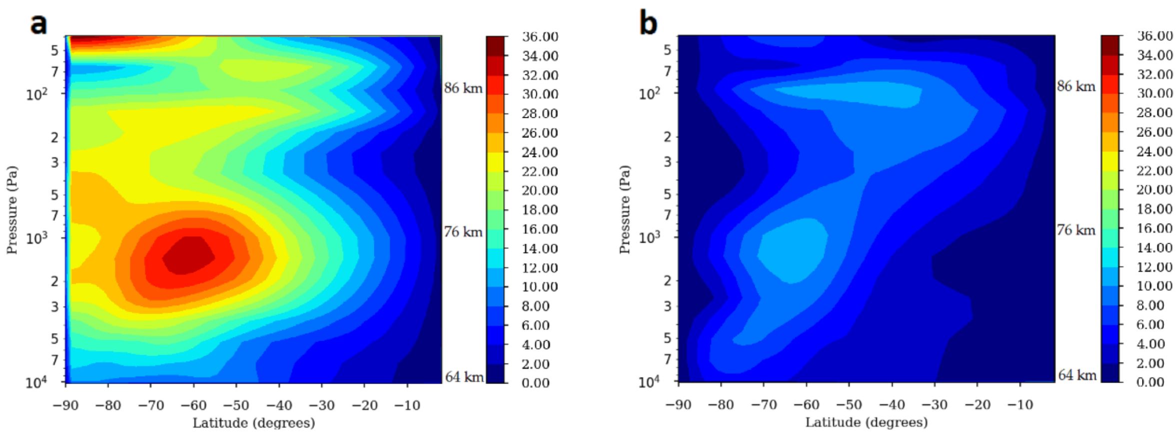

***Figure 44**: Fast Fourier transform (FFT) components of the meridional wind in the GCM simulation: (a) diurnal component; (b) semidiurnal component.*

The analysis conducted by Peralta et al. (2012) on VIRTIS-M data, revealed diurnal tides at southern polar latitudes (-70° to -85°) in the meridional wind field, while a quarterdiurnal tide seems to have an impact at high latitude in the zonal wind field. Although our study agrees with the considerations done for the VIRTIS-M meridional wind thermal tides, we found a big impact of the diurnal tide in the zonal wind field, while the 4/Vd component is negligible. It has to be noted that this 4/Vd sub-harmonics could be the result of nonlinear interactions between diurnal and semidiurnal tides, as occurs in the Earth (Peralta et al., 2012; Smith and Ortland, 2001; Egbert et al., 2010).

5.4 Thermal tides in the horizontal structure of temperature and wind fields

In order to investigate the nature of the main observed and modelled features of the atmosphere of Venus, we analyzed the horizontal structure of the simulated temperature anomaly field (**Fig. 45a, Fig. 45b**) for two different pressure levels: 5×10^2 Pa and 7×10^3 Pa, corresponding to the upper inversion level and the cold collar, respectively.

The horizontal structure of the overall temperature anomaly field shows that thermal tides obtained in the IPSL Venus GCM have a large impact from the equator until -80° latitude, at both pressure levels.

- At 5×10^2 Pa, the thermal tides have a large impact, with amplitudes roughly 8 K. This pressure level shows a complex pattern of the thermal tides: multiple maxima and minima equatorward of -55° and just one minimum and one maximum poleward.
- At 7×10^3 Pa the amplitude is about 5 K at high latitude and 2 K at low latitude. The minimum-maximum couple at high latitudes is still present, along with the multiple minima and maxima at low latitudes. However, for every minima and maxima, the phase is shifted with respect to 5×10^2 Pa.

Due to the spatial coverage, this kind of study is only meaningful with VIRTIS-M dataset (**Fig. 45c, Fig. 45d**). Moreover, we must note that our comparison is reliable only at high latitudes (poleward of -30°/-40°), where the diurnal component is the dominant one and no sign of semidiurnal tides is found. The latitude-local time distributions show that amplitudes are in general weaker in observations (this confirms **Fig. 39** and **Fig. 40**), while the phase in local time and latitude is in good agreement with the IPSL Venus GCM at both pressure levels.

The upper cold elongation and the modelling of this simulated feature may be related to the forcing induced by thermal tides in the temperature field (**Fig. 45**). Being the upper cold elongation, a modelled thermal feature, we would expect some discrepancies between model and data at 5 x 10^2 Pa, at mid-to-high latitudes, where this second inversion appears. But we didn't find macroscopic disagreements. On the other hand, the fact that the 7 x 10^3 Pa pressure level shows consistency between GCM and data, it is not surprising, being the cold collar well reproduced in the simulation: the minimum towards the morning terminator and the maximum towards the evening terminator are consistent with observations (**Fig. 27**). In general, the cold collar seems to be enhanced by thermal tides in the temperature field (**Fig. 45**).

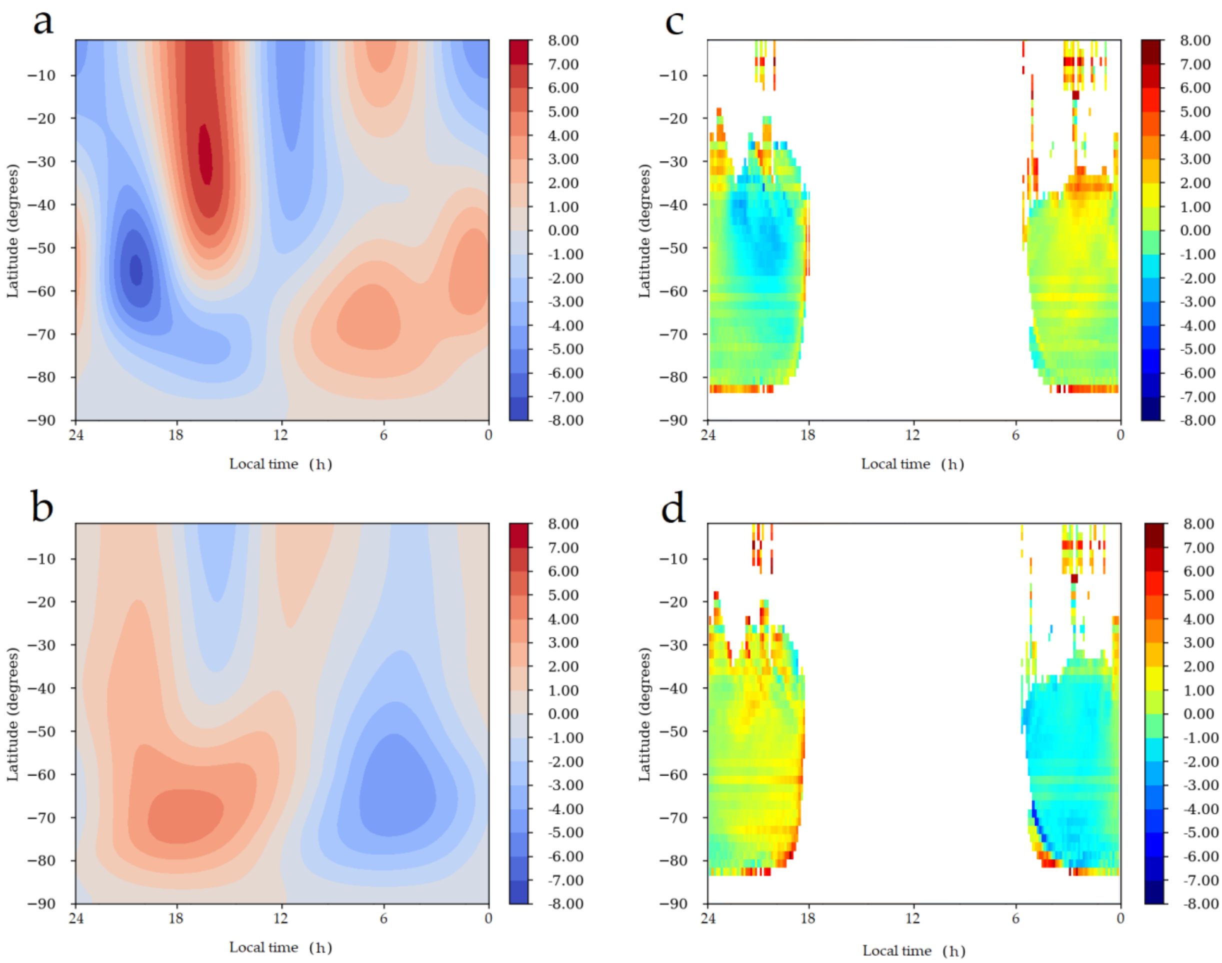

Figure 45*: Horizontal structure of the temperature anomaly field: (a) IPSL Venus GCM, 5 × 10^2 Pa (80 km), Scarica et al. (2019); (b) IPSL Venus GCM, 7 x 10^3 Pa (67 km); (c) VIRTIS-M, 5 x 10^2 Pa (80 km); VIRTIS-M, 7 x 10^3 Pa (67 km).*

The horizontal structure of the zonal wind and meridional wind anomaly fields (**Fig. 46**) has been derived for these pressure levels. The altitude level of the upper cold elongation presents strong thermal tides in the zonal wind high latitude (**Fig. 46a**, poleward of -70°) and in the meridional wind mid-to-high-latitude (**Fig. 46c**, poleward of -40°). The thermal tides appearing in the wind fields, at the cold collar altitude, is weaker (**Fig. 46b** and **Fig. 46d**), being its amplitude ~ 50% than the upper cold elongation.

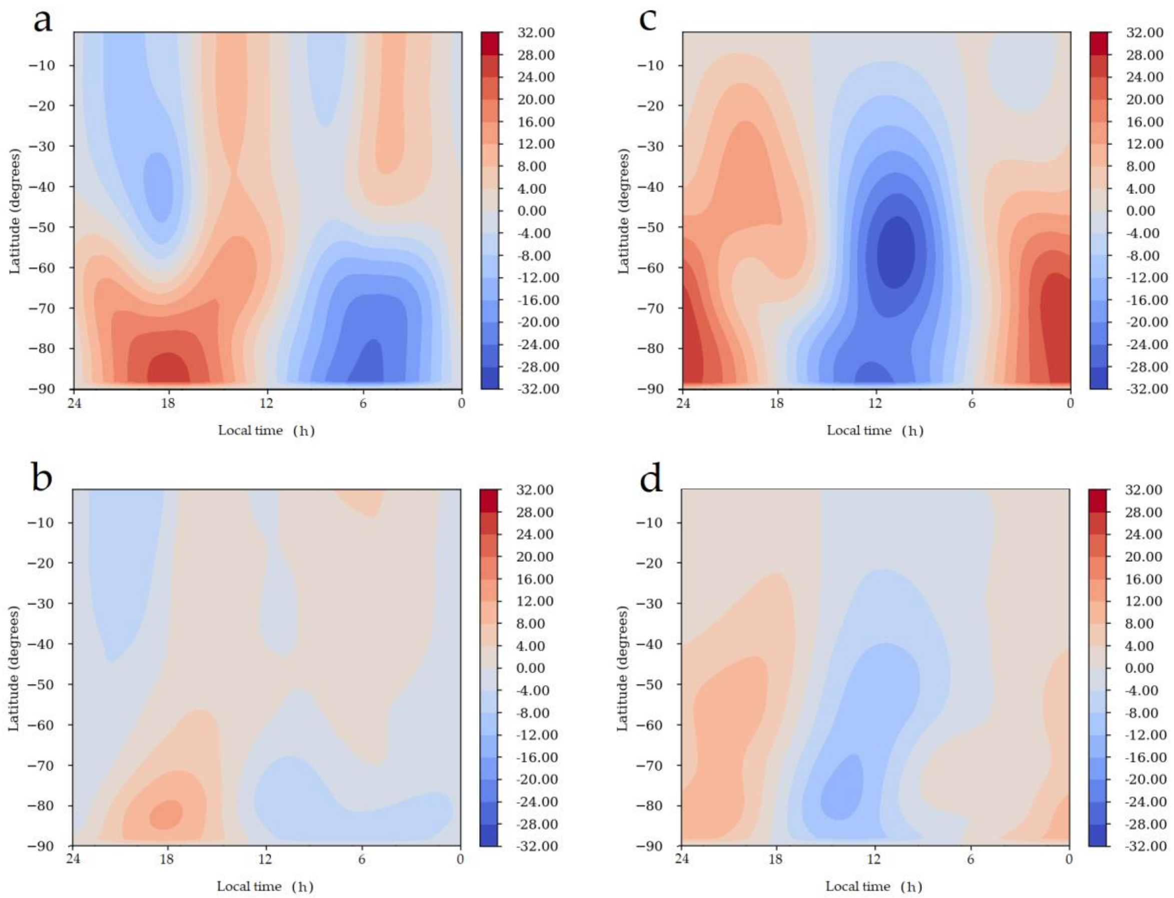

***Figure 46**: Horizontal structure of the IPSL Venus GCM wind anomaly field: (a) zonal wind, 5 × 10^2 Pa (80 km); (b) zonal wind, 7 x 10^3 Pa (67 km); (c) meridional wind, 5 x 10^2 Pa (80 km); (d) meridional wind, 7 x 10^3 Pa (67 km).*

- At 5 x 10^2 Pa, the thermal tides forcing in the high latitudes zonal wind displays the opposite phase than the forcing in the temperature field at the same latitudes. Close to the equator, just a slightly shift of phase appears between the thermal tides induced in the zonal wind and in the temperature. The opposite is found at 7 x 10^3 Pa: a shift in phase is found at low latitudes, while at high latitudes minima and maxima of the temperature and zonal wind fields are located approximately at the same local time.
- A ~6 h shift in local time is displayed between the simulated thermal tides of the zonal and meridional winds, at both pressure levels. The 5 x 10^2 Pa meridional wind jet located around -50°/-60° latitude, gains a strong poleward contribution

by thermal tides in the subsolar point (12 h), while a strong equatorward input is given by thermal tides at the antisolar point (0 h), but at higher latitudes.

No thermal tides signatures are visible in the wind field at the right altitude and latitude of the cold collar (**Fig. 46b** and **Fig. 46d**); on the other hand, the simulated peaks coincide with the location of the warm pole. Thermal tides signatures have also been found in the wind fields within the polar warm region associated to the modelled second inversion (**Fig. 46a** and **Fig. 46c**).

5.4.1 Horizontal structure of the Thermal tides subharmonics

In the discussion of the simulation based on their AFES model, Ando et al. (2016) suggested that the thermal tides are crucial for the structure of Venus upper polar atmosphere and above cloud levels. This includes the upper cold elongation that they modelled and that we also found in our analysis of the IPSL Venus GCM.

In order to study this possibility, we analyzed the horizontal structure of the temperature anomaly field for the three main harmonics. The quarterdiurnal component have not been reported in this study; its amplitude is much smaller than all the other main harmonics, along the entire hemisphere. This study has been conducted on the temperature, zonal wind and meridional wind field (**Fig. 47**, **Fig. 48** and **Fig. 49**), for the 5×10^2 Pa and 7×10^3 Pa pressure levels.

We already discussed that the horizontal structure of the overall temperature anomaly field (**Fig. 45**) shows that thermal tides obtained in the IPSL Venus GCM have a large impact from the equator until -80° latitude. This result was even more clear in the zonal and meridional wind field, where peaks of thermal tides were detected until the south pole.

After the decomposition, we observed that the diurnal component (**Fig. 47a**, **Fig. 47d**) is the one responsible for the thermal tides signatures at high latitudes in the temperature fields; its amplitude peaks between -55° and -80° and has a value of 5 K. The phase of the peaks is the opposite at the two pressure levels: temperature increases towards the evening terminator within the cold collar, and increases towards the morning terminator at 5×10^2 Pa. More in detail, the upper cold elongation shows a different phase with altitude, being more consistent with the cold collar at pressures higher than 7×10^2 Pa (not shown), with an opposite phase below 7×10^2 Pa.

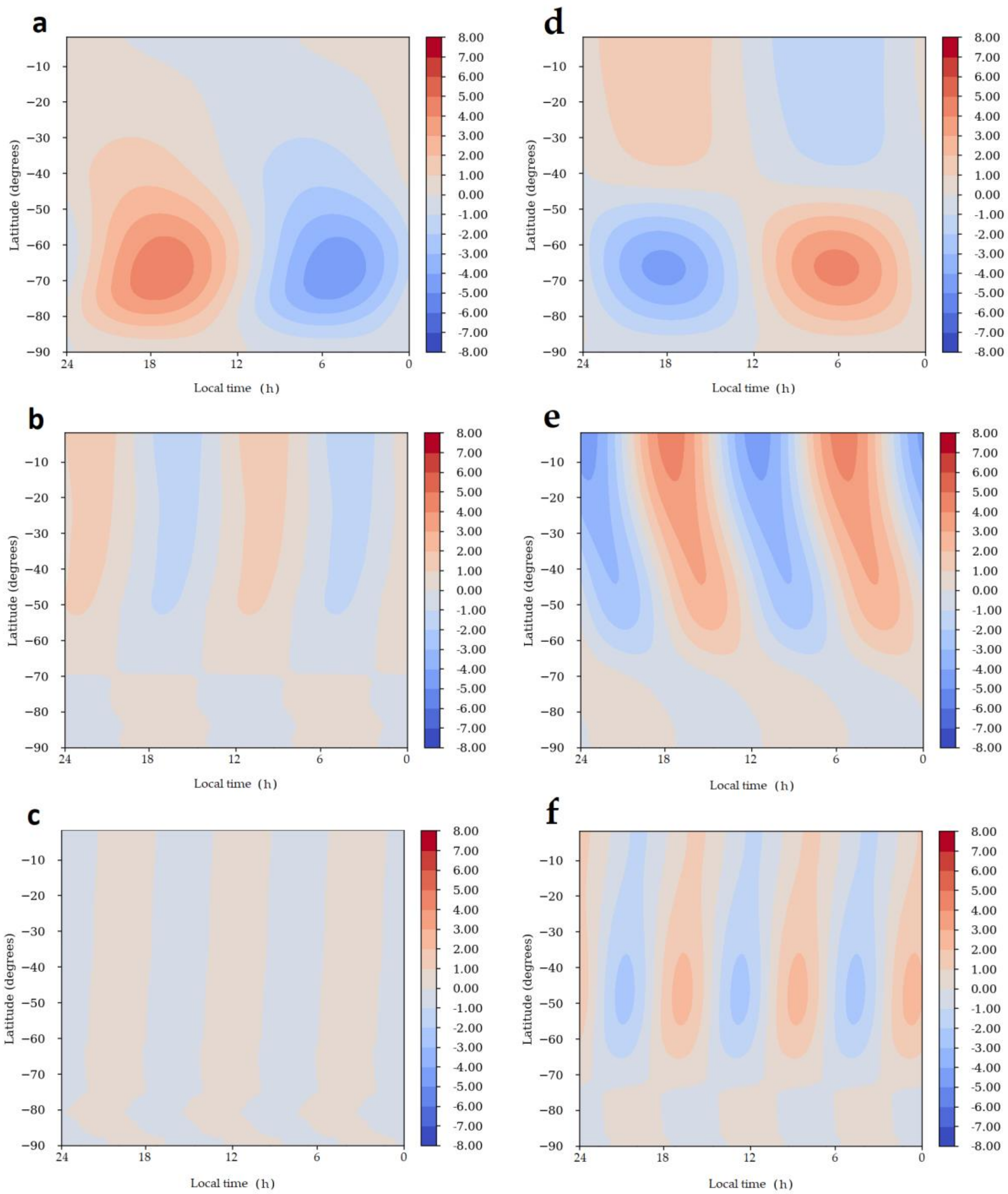

***Figure 47**: Horizontal structure of the IPSL Venus GCM temperature anomaly field: (a) 1/Vd, 7 × 10^3 Pa (67 km); (b) 2/Vd, 7 × 10^3 Pa (67 km); (c) 3/Vd, 7 × 10^3 Pa (67 km); (d) 1/Vd, 5 × 10^2 Pa (80 km); (e) 2/Vd, 5 × 10^2 Pa (80 km); (f) 3/Vd, 5 × 10^2 Pa (80 km).*

As already guessed, the low-to-mid-latitude minima and maxima of **Fig. 45a** are not related to the diurnal tide, but to the 2-nd and 3-rd subharmonics (**Fig. 47b**, **Fig. 47c**, **Fig. 47e**, **Fig 47f**). In the upper cold elongation pressure level, the semidiurnal component dominates at latitudes equatorward of -55° and peaks at the equator with an amplitude of 5 K. At the same level, the terdiurnal component reaches its maximum amplitude of 3 K at mid-latitudes (between -30° and -60°). At the cold collar pressure level, terdiurnal component becomes negligible and also the 2/Vd subharmonics has a low impact (about 2 K at low latitudes): therefore, the diurnal tides are dominating in the entire hemisphere.

The horizontal structure of the zonal wind anomaly field for the two main harmonics is shown in **Fig. 48** for 5 x 10^2 Pa and 7 x 10^3 Pa. The diurnal component of 3 m/s amplitude at 7 x 10^3 Pa high latitudes (poleward of -80°) becomes 6 m/s at 5 x 10^2 Pa (similar latitudes). The semidiurnal component peaks close to the pole at cold collar pressure level and then it peaks on lower latitudes at lower pressure levels. The fact that subharmonics with higher order than 3 are negligible and the strong dominance of diurnal tides, does not agree with VIRTIS observations, although latitudinally limited.

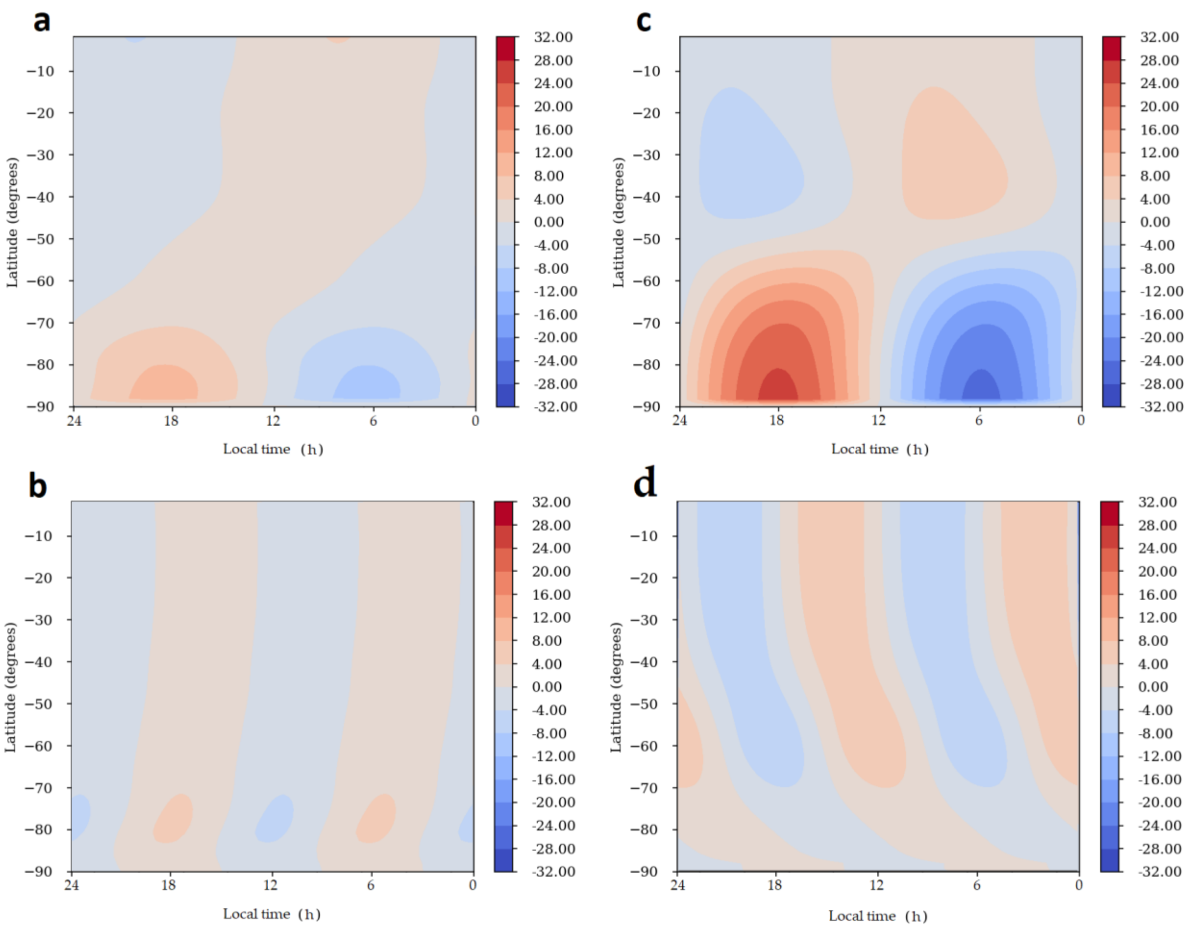

Figure 48*: Horizontal structure of the IPSL Venus GCM zonal wind anomaly field: (a) 1/Vd, 7 × 10^3 Pa (67 km); (b) 2/Vd, 7 × 10^3 Pa (67 km); (c) 1/Vd, 5 × 10^2 Pa (80 km); (d) 2/Vd, 5 × 10^2 Pa (80 km).*

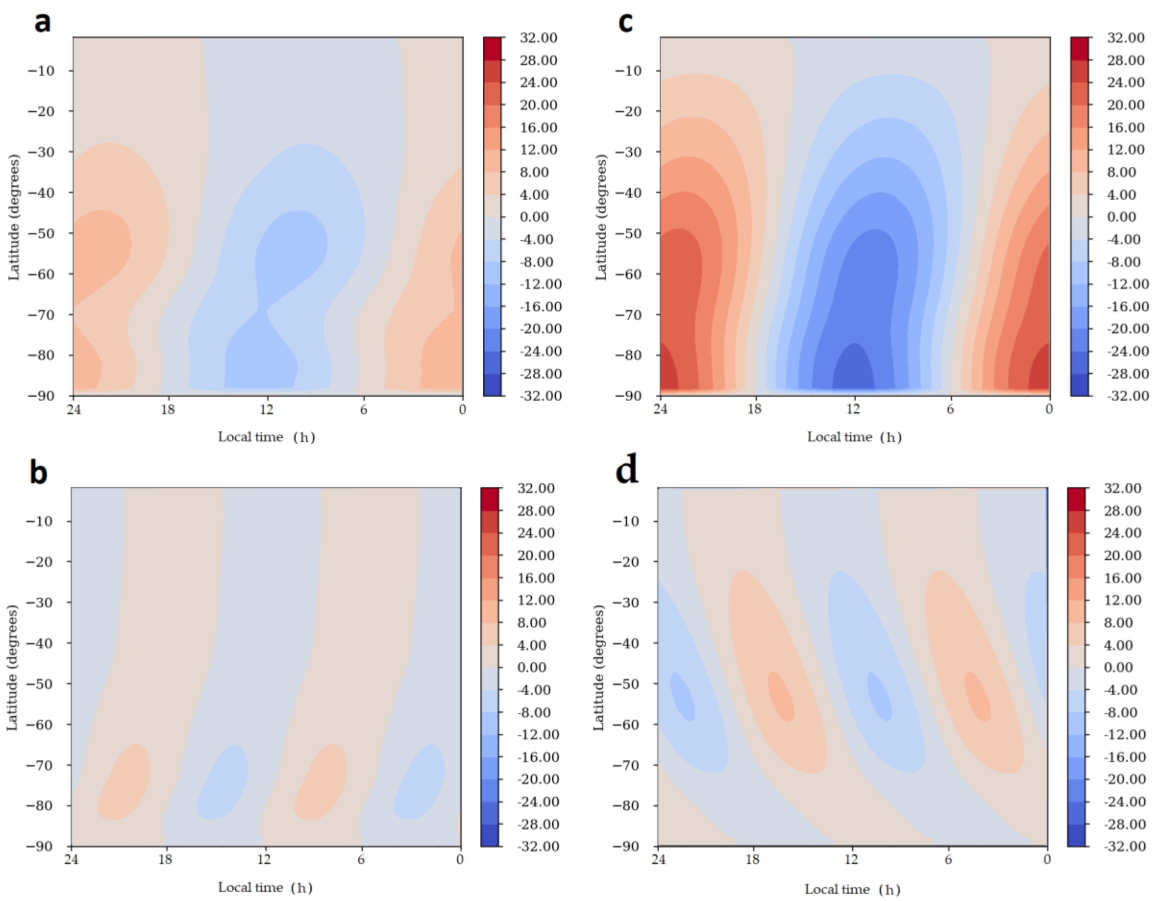

Figure 49: *Horizontal structure of the IPSL Venus GCM meridional wind anomaly field: (a) 1/Vd, 7 × 10^3 Pa (67 km); (b) 2/Vd, 7 × 10^3 Pa (67 km); (c) 1/Vd, 5 × 10^2 Pa (80 km); (d) 2/Vd, 5 × 10^2 Pa (80 km).*

Diurnal component dominates also in the horizontal structure of the meridional circulation (**Fig. 49**). However, the impact of semidiurnal tides is not negligible, especially in the cold collar pressure level, where its amplitude is more than 50% of diurnal tides' amplitude. The high latitude peak at 7 x 10^3 Pa is due to the superposition of the 1/Vd subharmonic with the 2/Vd, as well as the mid latitude jet (between -50° and -60°) at 5 x 10^2 Pa.

The fact that the phase of the dominant diurnal tide does not vary with latitude, at both pressure levels, implies a direct poleward motion during daytime and equatorward during nighttime, that is consistent with observations (Peralta et al., 2012).

5.5 Thermal tides discussion and comparison with the AFES GCM

The general behavior shown in the analysis from **Fig. 41** to **Fig. 48**, is consistent with previous IPSL Venus GCM simulations, but shows some differences with the AFES model (Ando et al., 2018). Indeed, while they didn't produce a similar study for the 67 km altitude – because of the lack of a cold collar feature in their model – we know that at 80 km, their maximum values for the total temperature deviation are somewhat higher than IPSL Venus GCM, while the amplitudes of the diurnal and semidiurnal tides for both studies are comparable, which suggests that higher wave number components could be significant in their model (being the total temperature deviation the sum of all the components).

In fact, Takagi et al. (2018) studied the amplitudes of the terdiurnal and quarterdiurnal tides in the AFES-Venus GCM simulations, and showed that in the vertical winds, peak amplitudes of these higher harmonics are roughly 50% and 25%, respectively, compared to semidiurnal tide, while the 2/Vd subharmonics is about 50% of the 1/Vd. In our FFT analysis of the simulated vertical wind field (**Fig. 50**), while the 2/Vd subharmonic is more than the 50% of 1/Vd, the terdiurnal and quarterdiurnal components seem negligible (for this reason, they are not shown).

Moreover, comparing **Fig. 47** of the present work, with **Fig. 8** of Ando et al. (2018), it is clear that the most significant component in the upper inversion area (5×10^2 Pa, 60°–90°) is the diurnal tide. The maxima and the minima of the diurnal component locate around −65° latitude in our model and 45° in Ando et al. (2018). Besides of being out of the upper cold elongation, their peaks are not consistent with the IPSL Venus GCM.

Consequently, due to the different thermal tide contributions, we find it unlikely that the upper thermal inversion seen in both the IPSL Venus GCM and the AFES-Venus GCM is due to the thermal tides in this area.

Because it is a structure observed in the temperature field, the origin of the upper inversion is probably related to the heating or cooling rates used in each GCM. According to Ando et al. (2018), moving upwards the top altitude of the solar heating from 80 km to 90 km did not affect the thermal structure much. At the same time, in the IPSL model, changing only the solar heating rates (between Lebonnois et al. 2016 and Garate-Lopez and Lebonnois, 2018) did not affect the polar thermal structure near the cloud-top. Therefore, it seems that this upper inversion is barely sensitive to the solar heating computation scheme. This is consistent with the fact that, at latitude poleward of +/-60°, the thermal balance is mostly obtained between dynamical heating and infrared cooling.

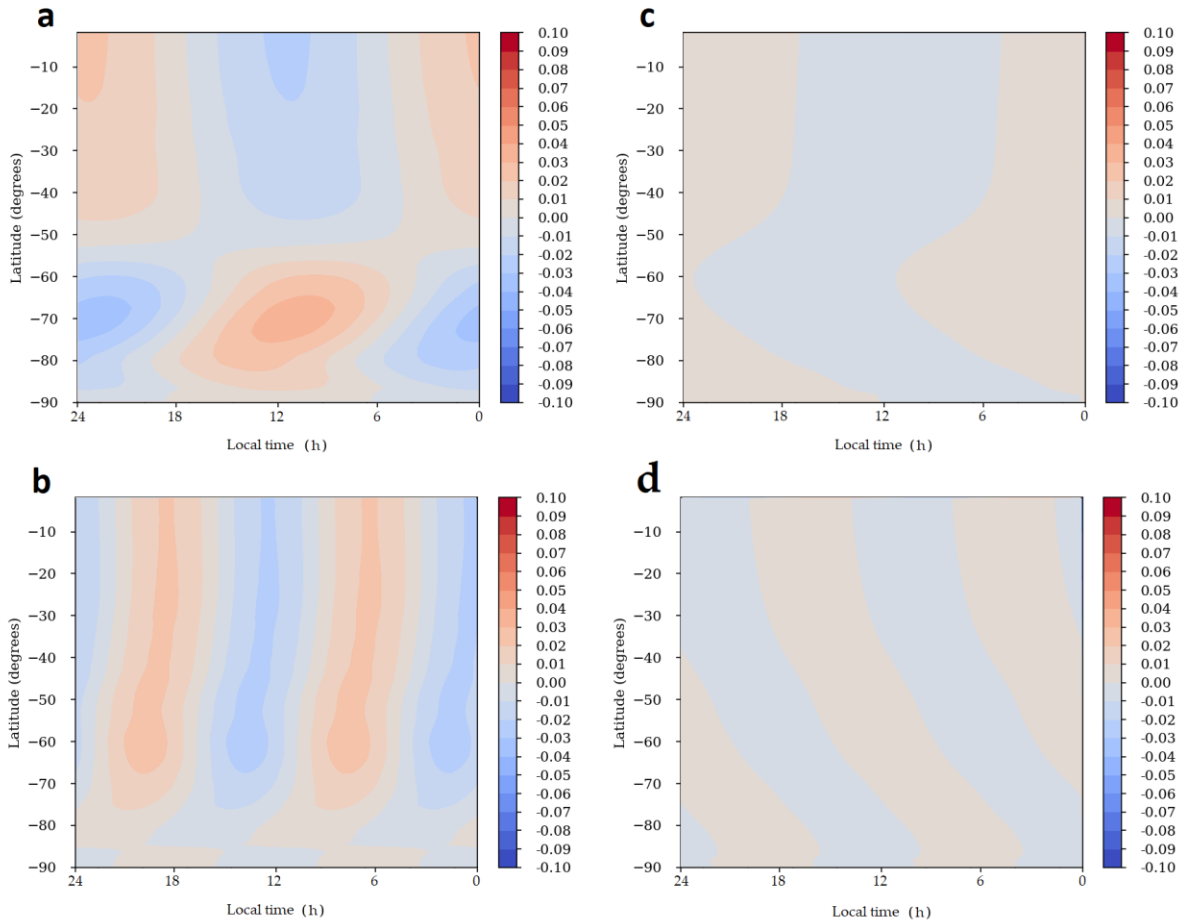

Figure 50*: Horizontal structure of the IPSL Venus GCM vertical wind anomaly field: (a) 1/Vd, 7 × 10^3 Pa (67 km); (b) 2/Vd, 7 × 10^3 Pa (67 km); (c) 1/Vd, 5 × 10^2 Pa (80 km); (d) 2/Vd, 5 × 10^2 Pa (80 km).*

For the infrared cooling rates, using the latitudinal variation in the cloud structure did affect significantly the polar thermal structure in the work of Garate-Lopez and Lebonnois (2018), inducing the presence of the simulated cold collar, at the right altitude and latitude. However, it did not remove the upper inversion, though it reduced it.

Both GCMs have slightly different vertical resolution for the calculation grid: 1 km for the AFES-Venus and 1.5 km for the IPSL Venus GCM around the upper inversion level. For this reason, we do not believe that vertical resolution is responsible for the modelling of this structure; however, improving the vertical resolution – and thus the capability of the model to resolve low scale gravity waves – could help to reveal the nature of this feature. An attempt has been made. We produced a finer vertical grid, made of 150 vertical levels very dense within the cloud deck, but instabilities in the temperature field arose in the process. A new simulation with better vertical resolution, at least in the cloud region and above, would be of interest for future works.

It is most likely that the origin of this thermal structure is related to the particle distribution used in the model within the region of this upper inversion, rather than to thermal tides. The latitudinal variations suggested by the work of Haus et al. (2015) may not be enough to model the balance between radiative cooling and dynamical heating correctly. Unfortunately, observations of the opacity, composition and particle size in the clouds are incomplete, especially in the polar atmosphere.

Conclusions

We validated the latest version of the IPSL Venus GCM (Garate-Lopez and Lebonnois, 2018): simulated temperature and wind fields have been compared to the data obtained in the mesosphere of Venus by the VIRTIS and VeRa experiments onboard the ESA space mission Venus Express. Through this validation of the IPSL Venus GCM, we have an insight into the main issues and the present simulation capabilities for the atmosphere of Venus, as well as a test of the state of the art of General Circulation Models for environments other than Earth.

The zonal and temporal average of the simulated temperature and wind fields display a general agreement with observations, both in terms of the qualitative overall behavior and in the characteristics of some peculiar features.

Indeed, the IPSL Venus GCM shows two different dynamical regions, with temperatures increasing from the equator to the south pole at pressures lower than 10^3 Pa, and decreasing towards the pole at pressures higher than 10^3 Pa. This is consistent with the analysis conducted in this work, by using the VeRa and VIRTIS dataset. The presence of a modelled, well-formed cold feature, at pressures higher than 3-4 × 10^3 Pa and poleward of -60°, is a striking resemblance with the observed cold collar, that appears in the global averaged maps and profile, as well as in the polar temperature maps presented in this work. The cold collar shows temperatures about 15–20 K colder than the surroundings. The unique capability of the IPSL Venus GCM to produce a well-formed cold collar, marks a milestone in the modelling of Venus atmosphere.

This comparison also demonstrates that General Circulation Models are now able to reproduce Venus' super-rotation. A fully developed retrograde superrotation is modelled, consistently with data. High zonal wind velocities are built up beneath the clouds, but reach maximum values at cloud top (~ 120 m/s), as observations revealed. The IPSL Venus GCM presents cloud top winds consistent with the cloud tracking presented in Sànchez-Lavega et al. (2008). Lower velocities have been simulated in the bottom clouds and the modelled wind peak is shifted poleward with respect to observations, being located at ~ -60°, which is -10° poleward than data. These two discrepancies lead to a higher vertical shear in the model, at low-to-mid latitudes (from 0° to -60°), and to steeper zonal wind profiles at high latitudes (poleward of -60°).

Perturbations induced by diurnal cycle arise in the model and they agree in both amplitude and phase with thermal tides observed in the data temperature field. The larger contributions in the IPSL Venus GCM temperature anomalies are due to the first and the second harmonic of thermal tides, with the diurnal tide that is the most important component at high latitudes (maxima at 5 × 10^2 Pa and 5 × 10^3 Pa), and the semidiurnal tide that dominates at low and mid latitudes (between 10^2 and 10^3 Pa). This is consistent with data, although our comparison could only be performed in the mid-to-high latitude range (from -40° to the pole), due to the low observational spatial coverage at low latitude.

We relied on Peralta et al. (2012) for the comparison of thermal tides that develop in the modelled and observational wind fields. The analysis of Peralta et al. (2012) agrees with the simulated thermal tides induced within the meridional wind field, but not with the ones in the zonal wind field. We can confirm the meridional circulation deduced by data: a daytime poleward motion and a nighttime equatorward motion are induced by thermal tides. On the other hand, the discrepancies of the modelled and observational thermal tides in the zonal wind field, may be related to nonlinear interactions between diurnal and semidiurnal tides; moreover, a more extensive analysis of data – limited to -72°/-73° in Peralta et al. (2012) – could help us to unveil the behavior of thermal tides in the zonal wind field.

We can conclude that the IPSL Venus GCM is capable to reproduce the observational temperature of Venus atmosphere and – in a more limited way – the winds, both in terms of the average fields and in the thermal tides associated with them.

However, we recognize a major unsolved question: an upper cold elongation appears in the simulated temperature field, is located at altitudes above 2×10^3 Pa and is coupled with a warmer region at high latitudes. This cold feature was already present in the former version of the IPSL Venus GCM (Lebonnois et al., 2016), as well as in the AFES model, which was the first to reproduce it (Ando et al., 2016). In both IPSL and AFES models, despite of modifications that have been made in the rates calculation schemes between previous and current versions of the two models, this feature did not change with respect to the old simulations (Ando et al., 2016, Lebonnois et al., 2016).

According to our analysis, the horizontal structure of the temperature anomaly field in the IPSL Venus GCM shows some discrepancies with the AFES model (Ando et al., 2018). Diurnal tide maxima and minima are located around -65° in our model and 20° equatorward in the AFES model. Moreover, despite of the discrepancies in the amplitudes of the total temperature deviation, the amplitudes of the diurnal and semidiurnal tides of the two studies are comparable, which implies a larger contribution of higher wave number components in the AFES model. This different behavior seems confirmed by comparing the thermal tides subharmonics in the vertical wind of the IPSL and the AFES models. Due to these reasons, we find no hint of a thermal tides involvement in the formation of the upper cold elongation: it is produced in both the IPSL Venus GCM and the AFES-Venus GCM, despite the discrepancies in the simulated thermal tides.

Our knowledge of the particle distribution in the Venus polar atmosphere, on which the aerosol density profiles that we used in our model relies (Haus et al., 2014; Haus et al., 2015), is still incomplete. The aerosol density profile used in our model probably may not accurately represent the actual atmosphere of Venus in the polar regions above the clouds. We suggest that this upper cold elongation may be related to this lack of accuracy, significantly affecting the cooling rates, rather than thermal tides' contribution or heating rates calculation.

We recognize several possible steps in the next future, that could help to solve this major issue:

i) Perform a more detailed comparison of the modelled and observational winds, especially the thermal tides affecting them. This could help to validate the model and to put better constrains on the capability of the IPSL Venus GCM to simulate Venus atmosphere.

ii) Test the impact of small-scale gravity waves, by improving the vertical resolution of the model.

iii) Test the sensitivity of the thermal structure to different distributions of the particle modes.

iv) Run a simulation with the new icosahedral dynamical core, Dynamico, that could allow a better modelling of the polar and subpolar features.

This study demonstrates that the state of the art of the GCMs for Venus is such to give an important contribution to the study of the planet, because of the capability to reproduce the general structure and the dynamics of Venus. However, General Circulation Models are in general very sensitive to model parameters and to the dynamical core; for such reason, observations are needed to put better constrains on numerical simulations. In the next decade, Venus exploration will continue, thanks to the next generation of space missions by several parties (CNSA, ISRO, NASA, ESA), in particular NASA and ESA proposals. Only a joined effort between the modelling scientific community and the space exploration community, can provide a satisfactory insight in all the scientific aspects regarding the atmosphere of Venus.

Bibliography

Arrhenius, S. The destinies of the stars. **1918**.

Boyer, C.; Guérin, P. Étude de la Rotation Rétrograde, en 4 Jours, de la Couche Extérieure Nuageuse de Vénus. *Icarus.* **1969**, 11, 338-355. DOI: 10.1016/0019-1035(69)90067-0

Allen, D.A.; Crawford J.W. Cloud structure on the dark side of Venus. *Nature* **1984**, 307, 222-224. DOI: 10.1038/307222a0

Sonett, C.P. A Summary Review of the Scientific Findings of the Mariner Venus Mission. *Space Science Reviews* **1963**, 2, 751-777, DOI: 10.1007/BF00208814

Avduevskii, V.S.; Marov, M.Ya.; Kulikov, Iu.N.; et al. Structure and Parameters of the Venus Atmosphere according to Venera Probe Data. In *Venus*; Hunten, D.M., Colin, L., Donahue, T.M., Moroz, V.I., Tucson, AZ, Eds.; University of Arizona Press: Tucson, AZ, USA **1983**; 280–298

Blamont, J.E. The VEGA Venus balloon experiment. *Adv. Space Res.* **1987**, *7*, 295–298

Saunders, R.S.; Spear, A.J.; Allin, P.C.; et al. Magellan mission summary. *J. Geophys. Res.* **1992**, *97*, 13067–13090, DOI:10.1029/92JE01397

Colin, L.; Hunten, D.M. Pioneer venus experiment descriptions. *Space Science Reviews* **1977,** 20, 451-525, DOI: 10.1007/BF02186463

Carlson, R.W.; Baines, K.H.; Encrenaz Th; et al. Galileo Infrared Imaging Spectroscopy Measurements at Venus. *Science* **1991**, 253, 1541-1548, DOI: 10.1126/science.253.5027.1541

Russell, C.T. The Cassini-Huygens Mission. Overview, Objectives and Huygens Instrumentarium. Russell, C.T.; University of California, U.S.A **2003**.

Konopliv, A.S.; Banerdt, W.B.; Sjogren, W.L. Venus Gravity: 180th Degree and Order Model. *Icarus* **1999**, 139, 3-18, DOI: 10.1006/icar.1999.6086

Schubert, G. General circulation and the dynamical state of the Venus atmosphere. In *Venus*; University of Arizona Press: Tucson, AZ, USA **1983**; 681-765

Pepin, R.O. Atmospheres on the terrestrial planets: Clues to origin and evolution. *Earth and Planetary Science Letters* **2006**, 252, 1-14, DOI: 10.1016/j.epsl.2006.09.014

Luhmann, J.G.; Russell, D.S. Magnetic fields in Venus nightside ionospheric holes - Collected Pioneer Venus Orbiter magnetometer observations. *Journal of Geophysical Research* **1992**, 97, 10267-10282, DOI: 10.1029/92JE00790

Titov D.V.; Taylor, F.W.; Svedhem, H. Introduction to the special section on Venus Express: Results of the Nominal Mission. *Journal of Geophysical Research* **2008**, 113, E00B19, DOI: 10.1029/2008JE003202

Fukuhara, T.; Futaguchi, M.; Hashimoto, G.; et al. Large stationary gravity wave in the atmosphere of Venus. *Nature Geoscience* **2017**, 10, 85-88, DOI: 10.1038/ngeo2873

Glaze, L.; Wilson, C.F.; Zasova, L.; et al. Future of Venus Research and Exploration. *Space Science Reviews* **2018**, 214, 37, DOI: 10.1007/s11214-018-0528-z

Taylor, F.; Grinspoon, D. Climate evolution of Venus. *Journal of Geophysical Research* **2009**, 114, E00B40, DOI: 10.1029/2008JE003316

Adams, W.S.; Dunham, T. Jr. Absorption Bands in the Infra-Red Spectrum of Venus. *Publications of the Astronomical Society of the Pacific* **1932**, 44, 243-245, DOI: 10.1086/124235

Vandaele, A.C.; De Mazière, M.; Drummond, R.; et al. Composition of the Venus mesosphere measured by Solar Occultation at Infrared on board Venus Express. *Journal of Geophysical Research* **2008**, 113, E00B23, DOI: 10.1029/2008JE003140

De Bergh, C.; Moroz, V.I.; Taylor, F.W.; et al. The composition of the atmosphere of Venus below 100 km altitude: An overview. *Planetary and Space Science* **2006**, 54, 1389-1397, DOI: 10.1016/j.pss.2006.04.020

Marcq, E.; Bézard, B.; Drossart, P.; et al. A latitudinal survey of CO, OCS, H_2O, and SO_2 in the lower atmosphere of Venus: Spectroscopic studies using VIRTIS-H. *Journal of Geophysical Research* **2008**, 113, E00B07, DOI: 10.1029/2008JE003074

Knollenberg, R.G.; Hunten, D.M. The microphysics of the clouds of Venus - Results of the Pioneer Venus particle size spectrometer experiment. *Journal of Geophysical Research* **1980**, 85, 8039-8058. DOI: 10.1029/JA085iA13p08039

Wilson, C.F.; Guerlet, S.; Irwin, P.G.J.; et al. Evidence for anomalous cloud particles at the poles of Venus. *Journal of Geophysical Research* **2008**, 113, E00B13, DOI: 10.1029/2008JE003108

Titov, D.V.; Ignatiev, N.I. McGouldrick, K.; et al. Clouds and Hazes of Venus. *Space Science Reviews* **2018**, 214, 61, DOI: 10.1007/s11214-018-0552-z

Belyaev, D.; Korablev, O.; Fedorova, A.; et al. First observations of SO_2 above Venus' clouds by means of Solar Occultation in the Infrared. *Journal of Geophysical Research* **2008**, 113, E00B25. DOI: 10.1029/2008JE003143

Krasnopolsky, V.A. Photochemistry of the Atmospheres of Mars and Venus. In *Physics and Chemistry in Space*; Krasnopolsky, V.A.; Springer Berlin Heidelberg (Berlin, Heidelberg) **1986,** 13, DOI: 10.1007/978-3-642-70401-7

Clancy, R.T.; Muhleman, D.O. Long-term (1979-1990) changes in the thermal, dynamical, and compositional structure of the Venus Mesosphere as inferred from microwave spectral line observations of ^{12}CO, ^{13}CO, and C ^{18}O. *Icarus* **1991**, 89, 129-146. DOI: 10.1016/0019-1035(91)90093-9

Shalygin, E.V.; Markiewicz, W.J.; Basilevsky, A.T.; et al. Active volcanism on Venus in the Ganiki Chasma rift zone. *Geophysical Research Letters* **2015**, 42, 4762-4769, DOI: 10.1002/2015GL064088

Bézard, B.; Fedorova, A.; Bertaux, J.-L.; et al. The 1.10- and 1.18-μm nightside windows of Venus observed by SPICAV-IR aboard Venus Express. *Icarus* **2011**, 216, 173-183, DOI: 10.1016/j.icarus.2011.08.025

Bézard, B.; Tsang, C.C.C.; Carlson, R.W.; et al. Water vapor abundance near the surface of Venus from Venus Express/VIRTIS observations. *Journal of Geophysical Research* **2009**, 114, E00B39, DOI: 10.1029/2008JE003251

Donahue, T.M.; Russell, C.T. The Venus Atmosphere and Ionosphere and Their Interaction with the Solar Wind: an Overview. In *Venus II : Geology, Geophysics, Atmosphere, and Solar Wind Environment*. Edited by Bougher, S.W.; Hunten, D.M.; Philips R.J.. Tucson, AZ : University of Arizona Press, **1997**.

Grinspoon, D.H. Implications of the high D/H ratio for the sources of water in Venus' atmosphere. *Nature* **1993**, 363, 428-431, DOI: 10.1038/363428a0

Kasting, J.F. Runaway and moist greenhouse atmospheres and the evolution of Earth and Venus. *Icarus* **1988**, 74, 472-494, DOI: 10.1016/0019-1035(88)90116-9

Grinspoon, D.H.; Bullock, M.A. Astrobiology and Venus exploration. In *Exploring Venus as a Terrestrial Planet*; Geophys. Monogr. Ser.; Esposito L. W., Stofan E. R., and Cravens T. E., AGU, Washington, D. C. **2007**, 176, 191-206, DOI: 10.1029/176GM12

Svedhem, H.; Titov, D.V.; McCoy, D.; et al. Venus Express—The first European mission to Venus. *Planet. Space Sci.* **2007**, *55*, 1636–1652, DOI: 10.1016/j.pss.2007.01.013

Sànchez-Lavega, A. An introduction to planetary atmospheres. Taylor & Francis **2011**.

Tellmann, S.; Pätzold, M.; Häusler, B.; et al. Structure of the Venus neutral atmosphere as observed by the Radio Science experiment VeRa on Venus Express. *J. Geophys. Res.* **2009**, 114, E00B36, DOI: 10.1029/2008JE003204

Lebonnois, S.; Schubert, G. The deep atmosphere of Venus and the possible role of density-driven separation of CO_2 and N_2. *Nature Geoscience* **2017**, 10, 473-477. DOI: 10.1038/ngeo2971

Kliore, A.J. Recent results on the Venus atmosphere from pioneer Venus radio occultations. *Advances in Space Research* **1985**, 5, 41-49, DOI: 10.1016/0273-1177(85)90269-8

Pätzold, M.; Häusler, B.; Bird, M.K.; et al. The structure of Venus' middle atmosphere and ionosphere. *Nature* **2007**, 450, 657–660, DOI: 10.1038/nature06239

Piccioni, G.; Drossart, P.; Sànchez-Lavega, A.; et al. South-polar features on Venus similar to those near the north pole. *Nature* **2007**, *450*, 637–640, DOI: 10.1038/nature06209

Garate-Lopez, I.; García Muñoz, A.; Hueso, R.; et al. Instantaneous three-dimensional thermal structure of the South Polar Vortex of Venus. *Icarus* **2015**, 245, 16-31, DOI: 10.1016/j.icarus.2014.09.030

Limaye, S.S.; Grassi, D.; Mahieux, A.; et al. Venus Atmospheric Thermal Structure and Radiative Balance. *Space Science Reviews* **2018**, 214, 71, DOI: 10.1007/s11214-018-0525-2

Haus, R.; Kappel, D.; Arnold, G. Atmospheric thermal structure and cloud features in the southern hemisphere of Venus as retrieved from VIRTIS/VEX radiation measurements. *Icarus* **2014**, 232, 232–248, DOI: 10.1016/j.icarus.2014.01.020

Montmessin, F.; Bertaux, J.-L.; Lefèvre, F.; et al. A layer of ozone detected in the nightside upper atmosphere of Venus. *Icarus* **2011**, 216, 82-85, DOI: 10.1016/j.icarus.2011.08.010

Sànchez-Lavega, A.; Hueso, R.; Piccioni, G.; et al. Variable winds on Venus mapped in three dimensions. *Geophysical Research Letters* **2008**, 35, L13204, DOI: 10.1029/2008GL033817

Müller-Wodarg, I. C. F.; Forbes, J. M.; Keating, G. M. The thermosphere of Venus and its exploration by a Venus Express Accelerometer Experiment. *Planetary and Space Science* **2006**, 54, 1415-1424, DOI: 10.1016/j.pss.2006.04.029

Luhmann, J. G.; Fedorov, A.; Barabash, S.; et al. Venus Express observations of atmospheric oxygen escape during the passage of several coronal mass ejections. *Journal of Geophysical Research* **2008**, 113, E00B04, DOI: 10.1029/2008JE003092

Galli, A.; Fok, M.-C.; Wurz, P.; et al. Tailward flow of energetic neutral atoms observed at Venus. *Journal of Geophysical Research: Planets* **2008**, 113, E00B15, DOI: 10.1029/2008JE003096

Piccialli, A. Cyclostrophic wind in the mesosphere of Venus from Venus Express observations. *Ph.D thesis, Technische Universität Braunschweig* **2010**.

Machado, P.; Widemann, T.; Peralta, J.; et al. Venus cloud-tracked and doppler velocimetry winds from CFHT/ESPaDOnS and Venus Express/VIRTIS in April 2014. *Icarus* **2017**, 285, 8-26, DOI: 10.1016/j.icarus.2016.12.017

Moroz, V. I.; Zasova, L. V. VIRA-2: a review of inputs for updating the Venus International Reference Atmosphere. *Advances in Space Research* **1997**, 19, 1191-1201. DOI: 10.1016/S0273-1177(97)00270-6

Linkin, V. M.; Kerzhanovich, V. V.; Lipatov, A. N.; et al. VEGA balloon dynamics and vertical winds in the Venus middle cloud region. *Science* **1986**, 231, 1417-1419, DOI: 10.1126/science.231.4744.1417

Drossart, P.; Montmessin, F. The legacy of Venus Express: highlights from the first European planetary mission to Venus. *The Astronomy and Astrophysics Review* **2015**, 23, 23, DOI: 10.1007/s00159-015-0088-0

Garate-Lopez, I.; Hueso, R.; Sánchez-Lavega, A.; et al. A chaotic long-lived vortex at the southern pole of Venus. N*ature Geoscience* **2013**, 6, 254-257, DOI: 10.1038/ngeo1764

Sornig, M.; Livengood, T.; Sonnabend, G.; et al. Venus upper atmosphere winds from ground-based heterodyne spectroscopy of CO_2 at 10 μm wavelength. *Planetary and Space Science* **2008**, 56, 1399-1406, DOI: 10.1016/j.pss.2008.05.006

Newman, M.; Leovy, C.; Maintenance of strong rotational winds in Venus middle atmosphere by thermal tides. *Science* **1992**, 257, 647-650, DOI: 10.1126/science.257.5070.647

Collard, A. D.; Taylor, F. W.; Calcutt, S. B.; et al. Latitudinal distribution of carbon monoxide in the deep atmosphere of Venus. *Planetary and Space Science* **1993**, 41, 487-494. DOI: 10.1016/0032-0633(93)90031-V

Tsang, C. C. C.; Irwin, P.G. J.; Wilson, C. F.; et al. Tropospheric carbon monoxide concentrations and variability on Venus from Venus Express/VIRTIS-M observations. *Journal of Geophysical Research* **2008**, 113, E00B08, DOI: 10.1029/2008JE003089

Bertaux, J.-L.; Nevejans, D.; Korablev, O.; et al. SPICAV on Venus Express: Three spectrometers to study the global structure and composition of the Venus atmosphere. *Planetary and Space Science* **2007**, 55, 1673-1700, DOI: 10.1016/j.pss.2007.01.016

Rossow, W. B.; del Genio, A. D.; Eichler, T. Cloud-tracked winds from Pioneer Venus OCPP images. *Journal of the Atmospheric Sciences* **1990**, 47, 2053-2084, DOI: 10.1175/1520-0469(1990)047<2053:CTWFVO>2.0.CO;2

Peralta, J.; Luz, D.; Berry, D. L.; et al. Solar migrating atmospheric tides in the winds of the polar region of Venus. *Icarus* **2012**, 220, 958-970, DOI: 10.1016/j.icarus.2012.06.015

Schofield, J. T.; Diner, D. J. Rotation of Venus’ s polar dipole. *Nature* **1983**, 305, 116-119, DOI: 10.1038/305116a0

Titov, D. V.; Svedhem, H.; Koschny, D.; et al. Venus Express science planning. *Planetary and Space Science* **2006**, 54, 1279-1297. DOI: 10.1016/j.pss.2006.04.017

Svedhem, H.; Titov, D.; Taylor, F.; et al. Venus Express mission. J*ournal of Geophysical Research* **2009**, 114, E00B33, DOI: 10.1029/2008JE003290

Markiewicz, W.J.; Titov, D.V.; Ignatiev, N.; et al. Venus Monitoring Camera for Venus Express. *Planetary and Space Science* **2007**, 55, 1701-1711. DOI: 10.1016/j.pss.2007.01.004

Formisano, V.; Angrilli, F.; Arnold, G.; et al. The planetary fourier spectrometer (PFS) onboard the European Venus Express mission. *Planetary and Space Science* **2006**, 54, 1298-1314, DOI: 10.1016/j.pss.2006.04.033

Barabash, S.; Sauvaud, J.-A.; Gunell, H.; et al. The Analyser of Space Plasmas and Energetic Atoms (ASPERA-4) for the Venus Express mission. *Planetary and Space Science* **2007**, 55, 1772-1792, DOI: 10.1016/j.pss.2007.01.014

Zhang, T. L.; Baumjohann, W.; Delva, M.; et al. Magnetic field investigation of the Venus plasma environment: Expected new results from Venus Express. *Planetary and Space Science* **2006**, 54, 1336-1343, DOI: 10.1016/j.pss.2006.04.018

Coradini, A.; Capaccioni, F.; Drossart, P.; et al. Virtis: an imaging spectrometer for the rosetta mission. *Planetary and Space Science* **1998**, 46, 1291-1304, DOI: 10.1016/S0032-0633(98)00025-7

Piccioni, G.; Drossart, P.; Suetta, E.; et al. VIRTIS: The Visible and Infrared Thermal Imaging Spectrometer. *ESA Special Publication* **2007**, SP 1295.

Drossart, P.; Piccioni, G.; Adriani, A.; et al. Scientific goals for the observation of Venus by VIRTIS on ESA/Venus express mission. *Planetary and Space Science* **2007**, 55, 1653-1672, DOI: 10.1016/j.pss.2007.01.003

Mueller, N.; Helbert, J.; Hashimoto, G. L.; et al. Venus surface thermal emission at 1 μm in VIRTIS imaging observations: Evidence for variation of crust and mantle differentiation conditions. *Journal of Geophysical Research* **2008**, 113, E00B17, DOI: 10.1029/2008JE003118

Grassi, D.; Politi, R.; Ignatiev, N.I.; et al. The Venus nighttime atmosphere as observed by the VIRTIS-M instrument. Average fields from the complete infrared data set. *J. Geophys. Res. Planets* **2014**, 119, 837–849, DOI: 10.1002/2013JE004586

Migliorini, A.; Grassi, D.; Montabone, L.; et al. Investigation of air temperature on the nightside of Venus derived from VIRTIS-H on board Venus-Express. *Icarus* **2012**, 217, 640–647, DOI: 10.1016/j.icarus.2011.07.013

Rodgers, C.D. Inverse Methods for Atmospheric Sounding: Theory and Practice. Rodgers, C.D.; *Published by World Scientific Publishing Co. Pte. Ltd*. **2000**, DOI: 10.1142/3171

Grassi, D.; Migliorini, A.; Montabone, L.; et al. Thermal structure of Venusian nighttime mesosphere as observed by VIRTIS-Venus Express. *J. Geophys. Res.* **2010**, 115, E09007, DOI: 10.1029/2009JE003553

Forget, F.; Hourdin, F.; Talagrand, O. CO_2 Snowfall on Mars: Simulation with a General Circulation Model. *Icarus* **1998**, 131, 302-316, DOI: 10.1006/icar.1997.5874

Spiga, A.; Guerlet, S.; Sylvestre, M. ÉmerGéantes: a new Global Climate Model to study the dynamics of Saturn's stratosphere - and beyond. *EGU General Assembly* **2013**, held 7-12 April, 2013 in Vienna, Austria

Forget, F.; Bertrand, T.; Vangvichith, M. A post-new horizons global climate model of Pluto including the N_2, CH_4 and CO cycles. *Icarus* **2017**, 287, 54-71, DOI: 10.1016/j.icarus.2016.11.038

Lebonnois, S.; Burgalat, J.; Rannou, P. Titan global climate model: A new 3-dimensional version of the IPSL Titan GCM. *Icarus* **2012**, 218, 707-722, DOI: 10.1016/j.icarus.2011.11.032

Vangvichith, M.; Forget, F.; Wordsworth, R. A 3-D General Circulation Model of Triton's Atmosphere. *American Astronomical Society, DPS meeting* **2010**; Bulletin of the American Astronomical Society, 42, 952

Turbet, M.; Leconte, J.; Selsis, F. The habitability of Proxima Centauri b. II. Possible climates and observability. *Astronomy & Astrophysics* **2016**, 596, 29, DOI: 10.1051/0004-6361/201629577

Bengtsson, L.; Bonnet, R.-M.; Grinspoon, D.; et al. Towards understanding the climate of Venus – Applications of terrestrial models to our sister planet. Edited by Bengtsson, L.; Bonnet, R.-M.; Grinspoon, D.; et al. *Springer*. **2013**.

Yamamoto, M.; Takahashi, M. The Fully Developed Superrotation Simulated by a General Circulation Model of a Venus-like Atmosphere. *J. Atmos. Sci.* **2003**, 60, 561–574. DOI: 10.1175/1520-0469(2003)060<0561:TFDSSB>2.0.CO;2

Yamamoto, M.; Takahashi, M. Dynamics of Venus' superrotation: The eddy momentum transport processes newly found in a GCM. *Geophysical Research Letters* **2004**, 31, L09701, DOI: 10.1029/2004GL019518

Yamamoto, M.; Takahashi, M. Superrotation Maintained by Meridional Circulation and Waves in a Venus-Like AGCM. *Journal of Atmospheric Sciences* **2006**, 63, 3296-3314, DOI: 10.1175/JAS3859.1

Ikeda, K.; Yamamoto, M.; Takahashi, M. Superrotation of the Venus atmosphere simulated by an atmospheric general circulation model, in *IUGG/IAMAS Meeting*, Perugia, **2007**

Yamamoto, M.; Takahashi, M. Venusian middle-atmospheric dynamics in the presence of a strong planetary-scale 5.5-day wave. *Icarus* **2012**, 217, 702-713, DOI: 10.1016/j.icarus.2011.06.017

Yamamoto, M.; Takahashi, M. Dynamics of polar vortices at cloud top and base on Venus inferred from a general circulation model: Case of a strong diurnal thermal tide. *Planetary and Space Science* **2015**, 113, 109-119, DOI: 10.1016/j.pss.2015.01.017

Lee, C.; Lewis, S. R.; Read, P. L. A numerical model of the atmosphere of Venus. *Advances in Space Research* **2005**, 36, 2142-2145, DOI: 10.1016/j.asr.2005.03.120

Lee C.; Richardson, M.I.; A general circulation model ensemble study of the atmospheric circulation of Venus. *J. Geophys. Res. Planets* **2010**, 115, E04002. DOI:10.1029/2009JE003490

Seiff, A.; Kirk, D. B.; Young, R. E.; et al. Measurements of thermal structure and thermal contrasts in the atmosphere of Venus and related dynamical observations - Results from the four

Pioneer Venus probes. *Journal of Geophysical Research* **1980**, 85, 7903-7933, DOI: 10.1029/JA085iA13p07903

Lee, C.; Lewis, S. R.; Read, P. L. A bulk cloud parameterization in a Venus General Circulation Model. *Icarus* **2010**, 206, 662-668, DOI: 10.1016/j.icarus.2009.09.017

Mendonca, J.M.; Read, P.L.; Lewis, S.R. New radiative transfer code in the Oxford Venus GCM, in *3rd International Conference on Venus*, Aussois, **2010**

Mendonca, J.M.; Read, P.L.; Lewis, S.R. Zonal winds on high latitudes on Venus: An improved application of cyclostrophic balance to Venus Express observations, *Icarus* **2012**, 217, 629–639 DOI: 10.1016/j.icarus.2011.07.010

Ando, H.; Sugimoto, N.; Takagi, M.; et al. The puzzling Venusian polar atmospheric structure reproduced by a general circulation model. *Nat. Commun.* **2016**, 7, 10398, DOI: 10.1038/ncomms10398

Tomasko, M.G.; Doose, L.R.; Smith, P.H.; et al. Measurements of the flux of sunlight in the atmosphere of Venus. *J. Geophys. Res.* **1980**, 85, 8167–8186, DOI: 10.1029/JA085iA13p08167

Takagi, M.; Sugimoto, N.; Ando, H.; et al. Three-Dimensional Structures of Thermal Tides Simulated by a Venus GCM. *J. Geophys. Res. Planets* **2018**, 123, 335–352, DOI: 10.1002/2017JE005449

Crespin, A.; Lebonnois, S.; Hourdin, F.; et al. Simulations of the Dynamics of Venus' Atmosphere with the LMD Venus General Circulation Model. American Astronomical Society, DPS meeting, *Bulletin of the American Astronomical Society* **2006**, 38, 515

Lebonnois, S.; Hourdin, F.; Eymet, V.; et al. Superrotation of Venus' atmosphere analyzed with a full general circulation model. *J. Geophys. Res.* **2010**, 115, DOI: 10.1029/2009JE003458

Mellor, G.L.; Yamada, T. Development of a turbulence closure model for geophysical fluid problems. *Rev. Geophys. Space Phys.* **1982**, 20, 851–875, DOI: 10.1029/RG020i004p00851

Lebonnois, S.; Sugimoto, N.; Gilli, G. Wave analysis in the atmosphere of Venus below 100-km altitude, simulated by the LMD Venus GCM. *Icarus* **2016**, 278, 38–51, DOI: 10.1016/j.icarus.2016.06.004

Garate-Lopez, I.; Lebonnois, S. Latitudinal variation of clouds' structure responsible for Venus' cold collar. Icarus **2018**, 314, 1–11, DOI: 10.1016/j.icarus.2018.05.011

Haus, R.; Kappel, D.; Arnold, G. Lower atmosphere minor gas abundances as retrieved from Venus Express VIRTIS-M-IR data at 2.3 µm. *Planet. Space Sci.* **2015**, 105, 159–174, DOI: 10.1016/j.pss.2014.11.020

Seiff, A.; Schofield, J.T.; Kliore, A.J.; et al. Model of the structure of the atmosphere of Venus from surface to 100 km altitude. *Adv. Space Res.* **1985**, 5, 3-58, DOI: 10.1016/0273-1177(85)90197-8

Scarica, P.; Garate-Lopez, I.; Lebonnois, S.; et al. Validation of the IPSL Venus GCM Thermal Structure with Venus Express Data. *Atmosphere* **2019**, 10, 584, DOI: 10.3390/atmos10100584

Dubos, T.; Dubey, S.; Tort, M.; et al. DYNAMICO-1.0, an icosahedral hydrostatic dynamical core designed for consistency and versatility. *Geoscientific Model Development* **2015**, 8, 3131-3150, DOI: 10.5194/gmd-8-3131-2015

Gierasch, P.; Goody, R. M.; Young, R. E.; et al. The General Circulation of the Venus Atmosphere: an Assessment. In *Venus II : Geology, Geophysics, Atmosphere, and Solar Wind Environment*. Edited by Stephen W. Bougher, D.M. Hunten, and R.J. Philips. Tucson, AZ : University of Arizona Press, **1997**, 459

Peralta, J.; Hueso, R.; Sánchez-Lavega, A. A reanalysis of Venus winds at two cloud levels from Galileo SSI images. *Icarus* **2007**, 190, 469-477., DOI: 10.1016/j.icarus.2007.03.028

Smith, A.K.; Ortland, D.A. Modeling and analysis of the structure and generation of the Terdiurnal Tide. *J. Atmos. Sci.* 2001, 58, 3116–3134, DOI: 10.1175/1520-0469(2001)058<3116:MAAOTS>2.0.CO;2

Egbert, G.D.; Erofeeva, S.Y.; Ray, R.D. Assimilation of altimetry data for nonlinear shallow-water tides: Quarter-diurnal tides of the Northwest European Shelf. *Cont. Shelf Res*. 2010, 30, 668–679, DOI: 10.1016/j.csr.2009.10.011

Ando, H.; Takagi, M.; Fukuhara, T.; et al. Local Time Dependence of the Thermal Structure in the Venusian Equatorial Upper Atmosphere: Comparison of Akatsuki Radio Occultation Measurements and GCM Results. *J. Geophys. Res. Planets* **2018**, 123, 2270–2280, DOI: 10.1029/2018JE005640

Ringraziamenti

La ricerca e il lungo lavoro che hanno condotto a questa tesi sono stati supportati da ASI (Agenzia Spaziale Italiana) e INAF (Istituto Nazionale di Astrofisica). Sento però di dover ricordare anche il contributo offerto da altre persone, le quali si sono rese partecipi, in modo più o meno diretto, della buona realizzazione di questo lavoro, offrendo professionalità o supporto morale, a seconda dei casi.

La stesura della propria tesi di dottorato è un momento cruciale del percorso di formazione, che sancisce un passaggio importante. Il sostegno di molti è stato fondamentale affinché raggiungessi questo mio traguardo, durante questi anni di dottorato e ancor prima: menzionare tutti coloro che hanno partecipato al mio progetto, sarebbe impossibile. La mia gratitudine per il vostro supporto si palesa in queste righe e spero che, nel contemplare questo lavoro di tesi, siate fieri del risultato che avete contribuito a produrre.

Sento però doveroso rimarcare alcuni nomi che associo fortemente all’idea di sostegno, perché questo lavoro ne uscirebbe impoverito senza una menzione particolare nei loro confronti. Difatti, uno dei bagagli che porterò con me al termine di questa esperienza è la mia idea di Ricerca, che si sposa con quella di collaborazione e raramente trova il massimo della sua espressione nella produzione isolata di un singolo individuo. È oltremodo chiaro, quindi, il motivo per cui indugio in queste menzioni, perché ora l’idea di lavoro collettivo fa parte della mia identità in maniera più profonda.

I miei genitori hanno sempre creduto in me e mi hanno seguito nei miei primi passi, guidandomi la mano sin dall’inizio, senza mai lasciarmi. Si sono fatti sostenitori delle mie scelte, anche quando sono uscito dal seminato per intraprendere la mia strada. A voi va la mia riconoscenza.

Mia sorella, sempre presente, è la voce della coscienza, che mi fa riflettere sulle mie scelte e mi fa ridiscutere le mie certezze, arricchendomi. A te va la mia riconoscenza.

Il mio Supervisor Giuseppe è solo l’ultima delle figure accademiche che mi abbiano seguito. Sono però felice di aver trovato proprio alla fine un perfetto esempio di correttezza ed etica professionale, in grado di guidare senza mai vincolare. Con la sua competenza e assidua presenza è stato la migliore delle guide. A te va la mia riconoscenza.

Itziar e Sebastien sono stati collaboratori insostituibili, la cui esperienza e disponibilità ha reso possibile questo progetto di tesi e la pubblicazione ad esso correlata. Il nostro lavoro è stato un perfetto esempio di collaborazione scientifica, di cui vado molto fiero. A voi va la mia riconoscenza.

Al Planeto Team del “Le Laboratoire de Météorologie Dynamique (LMD)”, per avermi ospitato durante la mia lunga permanenza parigina. A tutti voi va la mia riconoscenza.

Davide, Alessandra e Silvia hanno partecipato offrendo sapienti consigli e dati imprescindibili per questo studio, adducendo inoltre un apporto fondamentale alla mia prima pubblicazione scientifica. A voi va la mia riconoscenza.

Molti amici mi hanno accompagnato in questi anni. Vincenzo, Gigi e Alessandra, vi ringrazio per le risate condivise. Giocatori di “Storia de il Mito della Ruota”, vi ringrazio per la vostra fantasia, che è cosa preziosa. Famiglia di Ludosport Roma, sempre affiatata, vi ringrazio perché siete un focolare acceso di sentimenti positivi. A tutti voi va la mia riconoscenza.

Ad Angela, mia compagna di vita, che non a caso lascio per ultima, in un ricercato effetto scenico: dulcis in fundo.